Umsetzung und Optimierung robotischer Hüpfbewegungen mit bio-inspirierter Virtual Model Control

Realization and optimization of robotic hopping motions using bio-inspired virtual model control

Ausarbeitung zur Master-Thesis von Jonathan Oehlke
13.10.2015

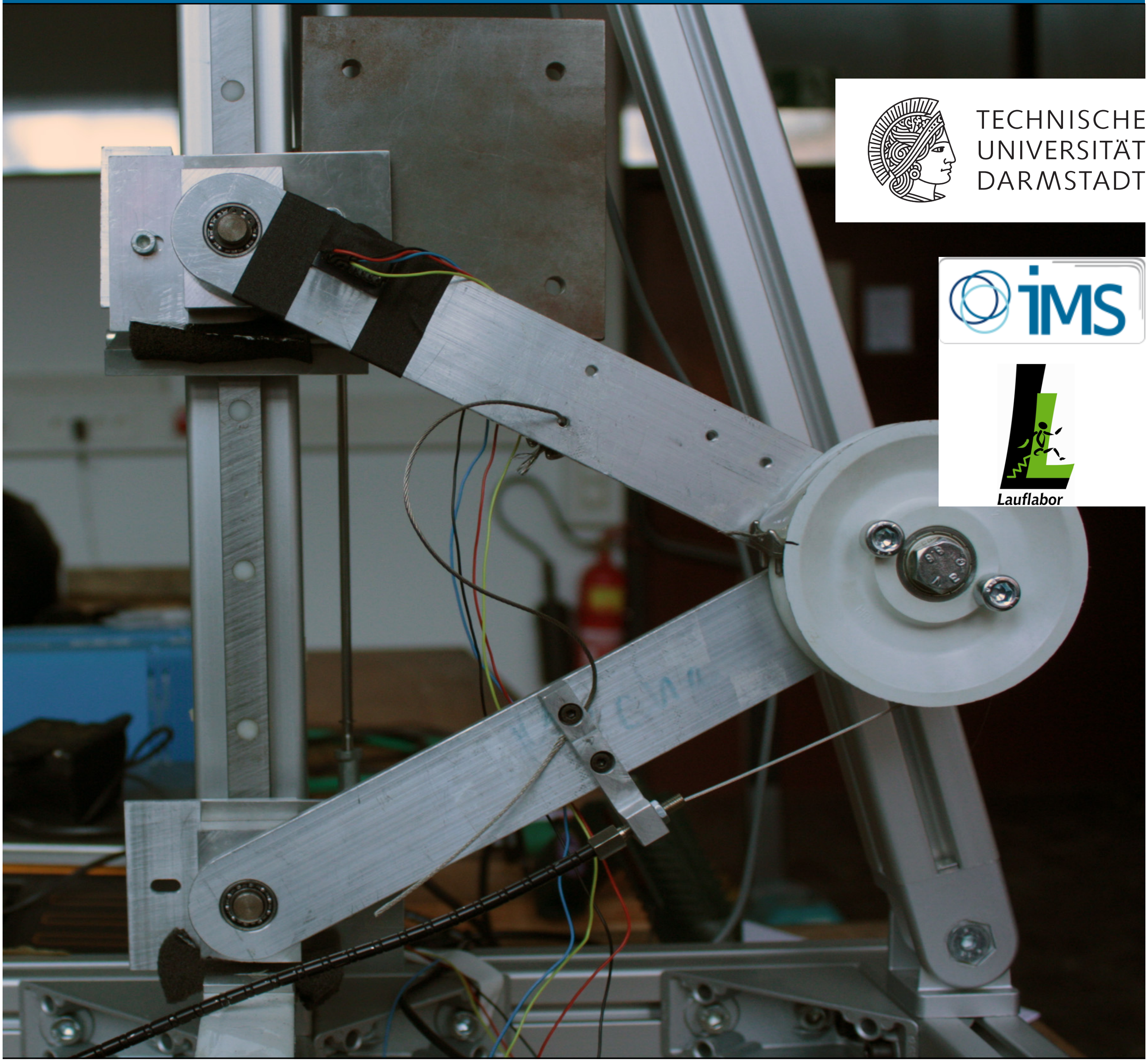

TECHNISCHE
UNIVERSITÄT
DARMSTADT

iMS

Lauflabor

Jonathan Oehlke
Matrikelnummer: 1570872

Masterthesis
Umsetzung und Optimierung robotischer Hüpfbewegungen mit bio-inspirierter Virtual Model Control
Realization and optimization of robotic hopping motions using bio-inspired virtual model control

Submitted: 13.10.2015
Published under CC BY-NC-ND 4.0 International

Supervision:
Dr. Philipp Beckerle
Dr. Maziar Ahmad Sharbafi

Prof. Dr.-Ing. S. Rinderknecht
Institut für Mechatronische Systeme im Maschinenbau IMS
Fachbereich Maschinenbau
Technische Universität Darmstadt
Otto-Berndt-Straße 2
64287 Darmstadt

TECHNISCHE
UNIVERSITÄT
DARMSTADT

Umsetzung und Optimierung robotischer Hüpfbewegungen mit bio-inspirierter Virtual Model Control

Master Thesis

Für Herrn Jonathan Oehlke

Realization and optimization of robotic hopping motions using bio-inspired virtual model control

---

Recently, the number of robotic systems interacting with humans is increasing, e. g., assistive devices like prostheses. To design suitable actuators and control techniques for such scenarios, inspiration from biology may be considered as a helpful approach.

Therefore, a modular test bed "MarcoHopper 2.0" for testing and demonstrating elastic drive concepts in hopping motions was designed and set up in previous projects. The mechanics of the test bed resemble the mechanics of a leg with two segments (thigh and shank) and one joint (knee). Actuation is modular regarding the configuration of actuator and passive mechanical elements to enable the realization of different mechanical models of human muscles.

This thesis aims at the realization and optimization of a virtual model control approach for template-based hopping motions inspired from biology. Therefore, suitable models and controllers are to be researched, compared and selected. Accordingly, simulations of the robot motions serve for control design and optimization. Based on simulation results, hardware will be adapted to optimize hopping motions and the controller will be implemented on the test bed. The ability of the controlled system to achieve hopping with different properties (e.g., hopping height or frequency) will be identified and the controller will be refined considering practical issues. An experimental evaluation of motion performance and perturbation attenuation will be performed and compared to existing human motion data.

Aufgaben:

- Simulation-based design of template-based virtual model control for hopping and optimization of mechanical parameters
- Hardware adaptation and control implementation/optimization based on simulation results
- Experimental evaluation in comparison to existing human motion data (e. g., perturbation recovery)

Beginn der Arbeit: 30.04.2015

Betreuer: Maziar Sharbafi (IFS), Jing Liu (IFS), Philipp Beckerle (IMS)

Darmstadt, 27.04.2015 Prof. Dr.–Ing. S. Rinderknecht

Thesis Statement

Hiermit versichere ich, Jonathan Oehlke, die vorliegende Master Thesis ohne Hilfe Dritter nur mit den angegebenen Quellen und Hilfsmitteln angefertigt zu haben. Alle Stellen, die Quellen entnommen wurden, sind als solche kenntlich gemacht worden. Diese Arbeit hat in gleicher oder ähnlicher Form noch keiner Prüfungsbehörde vorgelegen. In der abgegebenen Thesis stimmen die schriftliche und elektronische Fassung überein.

I herewith formally declare that I have written the submitted thesis independently. I did not use any outside support except for the quoted literature and other sources mentioned in the paper. I clearly marked and separately listed all of the literature and all of the other sources which I employed when producing this academic work, either literally or in content. This thesis had not been handed in or published before in the same or similar form. In the submitted thesis the written copies and the electronic version are identical in content.

Darmstadt, August 9, 2018

(Jonathan Oehlke)

Abstract

Biological inspired templates can help to control complex robotic movements. In this thesis a control strategy, enabling hopping motions of a segmented robotic leg, is developed. The control bases on the spring loaded inverse pendulum (SLIP) model, which can describe the courses of displacement of the center of mass and the ground reaction force during human or animal hopping motions. To use this template as a calculation model for desired control values a method called virtual model control (VMC) is used. VMC implements virtual components in real structures to design a desired behavior. Existing actuators of the real system are controlled in a manner to mimic the effects, the virtual components would have on the system. The virtual component used in this work is a spring with certain properties. Like in the role model, the SLIP template, the spring is virtually attached between hip and foot of the robotic leg. The knee is the only actuated part of the structure. Through the control of the knee torque the effects of the virtual spring are mimicked. The used test-bed necessitates it to adjust the developed control laws for the compensation of losses. Different methods for the calculation of a variable virtual spring stiffness have been developed, resulting in stable hopping motions of the robotic leg in the used test-bed. The resulting control strategy does not need a feedback loop of the controlled parameter and is therefore a kind of a feed-forward approach. The possibility of an overlaid force-feedback control has been examined and the limits of this method have been estimated.

Kurzfassung

Von der Natur inspirierte Modellvorstellungen können helfen die Regelung komplizierter robotischer Bewegungnen zu realisieren. In dieser Arbeit wurde eine Regelungsstrategie entwickelt, die es ermöglicht Hüpfbewegungen eines segmentierten robotischen Beines zu ermöglichen. Die Regelung basiert auf dem "spring loaded inverse pendulum" (SLIP) Modell. Dieses ist in der Lage Kenngrößen menschlicher und tierischer Hüpf- und Laufbewegungen vorherzusagen. Um dieses Modell für die Entwicklung von Berechnungsvorschriften von Regelungsparametern zu nutzen, wurde eine Technik namens "virtual model control" (VMC) verwendet. Mittels VMC werden virtuelle Komponenten in reale Strukturen integriert, um erwünschtes Verhalten zu erzielen. Die real vorhandenen Aktoren werden in einer Weise gesteuert, dass sie die Effekte erzielen, die die virtuelle Komponente erzielen würde. Die verwendete virtuelle Komponente ist in diesem Fall eine Feder mit bestimmten Eigenschaften. Wie im Vorbild, dem SLIP Modell, wird die Feder virtuell zwischen Hüfte und Fuß des robotischen Beins angebracht. Das Knie ist die einzige angetriebene Stelle des Beins. Durch die Regelung des Drehmoments am Knie werden die Effekte der virtuellen Feder imitiert. Die Verwendung auf einem Prüfstand macht die Anpassung des Regel-Gesetzes notwendig, um auftretende Verluste zu kompensieren. Verschiedene Methoden der Berechnung einer virtuellen Feder-Steifigkeit wurden entwickelt. Die Anwendung auf dem Versuchsstand resultiert in einer stabilen Hüpfbewegung. Die Möglichkeit einer superponierten Kraftregelung wurde untersucht und auf ihre Anwendbarkeit und Grenzen hin beurteilt.

Contents

Abstract **IV**

List of Figures **VII**

List of Tables **XV**

Nomenclature **XVII**

1. Introduction **1**
- 1.1. Preface . . . 1
- 1.2. Models of human hopping/locomotion . . . 1
  - 1.2.1. Spring loaded inverted pendulum . . . 2
  - 1.2.2. Inverted pendulum . . . 3
- 1.3. Test-beds legged locomotion . . . 3
  - 1.3.1. Marco Hopper . . . 3
  - 1.3.2. Development of the test-bed Marco Hopper II . . . 4
  - 1.3.3. Single legged robot with variable knee stiffness - L-MESTRAN . . . 6
- 1.4. Virtual model control . . . 7

2. Development of models for the control of hopping motions **9**
- 2.1. Dynamic equations of models with ascending complexity - squats . . . 10
  - 2.1.1. Harmonic oscillator with single mass . . . 10
  - 2.1.2. Single mass oscillator with flight phase . . . 13
  - 2.1.3. Multi-body system with one mass . . . 13
  - 2.1.4. Multi-body system with distributed masses . . . 19
- 2.2. Dynamic equations of models with ascending complexity - hopping . . . 28
  - 2.2.1. Harmonic oscillator . . . 28
  - 2.2.2. Multi-body system with distributed masses . . . 30

3. Test-bed Marco Hopper II **33**
- 3.1. Configuration of MARCO Hopper II and changes . . . 33
  - 3.1.1. Segmented leg of MARCO II . . . 33
  - 3.1.2. Drive-train of Marco Hopper II . . . 34
  - 3.1.3. Sensor concept and implementation . . . 36
- 3.2. Simulation models Marco Hopper II . . . 44
  - 3.2.1. Single Mass Oscillator . . . 45
  - 3.2.2. Simulation of the segmented leg . . . 46
  - 3.2.3. Drive-train model . . . 51
  - 3.2.4. Ground model . . . 58

3.2.5. Friction model 59

4. Control **63**
4.1. Force control - feed forward control 63
4.1.1. Feed forward control - bang-bang control 66
4.1.2. Feed forward control - continuous change of spring stiffness 70
4.1.3. Feed forward control - bang-bang control and continuous change of the spring stiffness 72
4.1.4. Feed forward control + PID - bang-bang control and continuous change of spring stiffness 76
4.2. Force control - PID 84
4.3. Position control - SEA 86

5. Experiments and suggestion for changes **89**
5.1. Experiments 89
5.1.1. Theoretical power consumption and motor current requirements 89
5.1.2. Ground reaction force - leg length relationship 90
5.1.3. Comparison to human hopping motions 91
5.2. Problems and suggestion for changes 93
5.2.1. Motor controller 93
5.2.2. Change of the knee pulley 94
5.2.3. Power sources 94
5.2.4. Reduction of friction 95

6. Conclusion and future works **97**

A. Appendix **XXI**
A.1. Run of the test-bed XXI
A.2. Data DVD XXI
A.2.1. Simulation models and m-files XXII
A.2.2. Experimental results + analysis XXX
A.2.3. Graphics, photos and figures XXX
A.3. Tables measurement data XXX
A.4. Mechanical drawings XXX

Bibliography **XXXVI**

List of Figures

1.1. The test-bed MARCO Hopper consists of a foot, a shank and a body. The weight of the motor and the attached transmission serves as the body mass. A tooth-belt connected to the ends of the shank and the output shaft of the motor makes it possible to move the motor up and down the shank. A second rail guides the whole structure in the vertical direction. The foot is equipped with a ball of highly damping material, to absorb the impact energy of the landing and prevent damages on the structure [17]. 4

1.2. Picture of the test-bed Marco Hopper 2.0 5

2.1. Sketch of a single mass oscillator. The mass m has got one degree of freedom x. A spring with the rate k and the rest length l_0 attached to the mass drives the oscillation of the system. The lower end point of the spring never leaves the ground. 10

2.2. Sketch of the multi-body system driven by an ideal torque τ. The structure got one degree of freedom x. The torque τ should act like a force by the virtual spring with the stiffness k_v. 14

2.3. Sketch of the multi-body system of two segments with the length l_l driven by an ideal torque τ. The system is divided in two parts through a cut at the knee and underneath the foot. Forces acting at the section planes are shown. 15

2.4. [SIM] Comparison of the oscillation of the single mass oscillator (a) and the multi-body system (b). The stiffness of the spring k_v is adjusted for a stable oscillation of $\omega = 7$ rad/s. The initial position of the mass is $x = 0.2$m and the rest length $l_0 = 0.5$m. The solver used for the single mass oscillator is ODE45 and for the multi-body system ODE23. The resulting oscillations are equivalent. 16

2.5. Sketch of the multi-body system of two segments with the length l_l driven by a force F attacking on a lever arm with the length r_p. The lever arm is parallel to the rail/direction of x in the initial position. The system is divided in two parts through a cut at the knee and underneath the foot. Forces acting at the section planes are shown. 17

2.6. [SIM] Comparison of the oscillation of the single mass oscillator and the multi-body system driven by a force F on a lever arm at the knee. The stiffness of the spring k_v is adjusted for a stable oscillation with the frequency $\omega = 7$ rad/s. The initial position of the mass is $x = 0.2$m and the rest length $l_0 = 0.5$m. The solver used for the single mass oscillator is ODE45 and for the multi-body system ODE23. 18

2.7. [SIM] Oscillation of the top mass of an multi-body system with deviation of the initial angle of the lever arm $\Delta\beta$. The force generation law is not adapted, so a "‘wrong"’ force is effective for each position. The used solver is ODE23. 19

2.8. Sketch of the multi-body system driven by an ideal torque τ. There are three masses in the system, the mass on top of the leg m_1 and the masses of each link m_2, which are considered as concentrated in the center of mass of each segment. Moments of mass inertia are calculated relative to the foot or the hip/ the end point of the segments. The structure got one degree of freedom x. The torque τ should act like a force by the virtual spring with the stiffness k_v. The system is divided in two parts through a cut at the knee and underneath the foot. Forces acting at the section planes are shown. 20

2.9. [SIM] Comparison of the oscillation of the single mass oscillator (b) and a multi-body system (a). The stiffness of the spring k_v is adjusted for reaching the rest length of the spring of both systems. Both systems have the exact same sum of mass, but a different distribution of masses. The initial position of the top point is $x = 0.2$m and the rest length $l_0 = 0.5$m. The solver used for the single mass oscillator is ODE45 and for the multi-body system ODE23. 22

2.10. [SIM] Comparison of the oscillation of the single mass oscillator (a) and two different multi-body system settings (b+c). The stiffness of the spring k_v is adjusted for reaching the rest length of the spring. In the system (c) the same k_v as in (a) is used. All systems have exact the same sum of mass, but a different distribution of masses. The initial position of the top point is $x = 0.2$m and the rest length $l_0 = 0.5$m. The solver used for the single mass oscillator is ODE45 and for the multibodysystem ODE23. 23

2.11. [SIM] Motion- and force-patterns derived from a single mass oscillator model (SLIP) and a multibody-system model (MBS) with distributed masses. The oscillation of the top point is the same for both models. Force patterns of the ground reaction force are different, for the sum of masses in the systems are different. $m = 1$ kg while $m_1 = 0.498$ kg and $m_2 = 0.135$ kg. The solver used for the single mass oscillator model is ODE45 and for the multi-body system ODE23. 24

2.12. [SIM] Relation between the position of the top point x and the ground reaction forces F_{GRF} for the multi-body system and $F_{\mathrm{GRF,SM}}$ for the single mass oscillator. Both systems are tuned to have the same oscillation pattern (shown in Fig. 2.11. Both courses of the force are linear but have different slopes and offsets. The solver used for the single mass oscillator is ODE45 and for the multi-body system ODE23. 25

2.13. [SIM] The oscillation of the hip position x_h of the segmented leg with different initial positions. The cable of the knee is attached to a rigid point. 26

2.14. Sketch of the model for the harmonic oscillator. The structure got two degrees of freedom x and x_f. A spring with the rate k attached between the hip mass m and the foot mass m_4 drives the oscillation. The ground consists of parallel spring with the rate k_g and a spring with the rate d_g. The ground forces effect the oscillator only during the stance phase. 29

2.15. Free body diagram of the multi-body system with all involved forces and torques. (1) represents the upper link (thigh) and (2) the lower link (shank) of the leg. m_1 represents the mass on the top point, m_2 is the mass of a link, m_3 is the additional mass at the knee point and m_4 represents the mass of the foot. All masses produce gravitational and inertial forces. Additionally the mass moments of inertia (related to hip/foot point) of the links presented by θ_l take effect. All forces ($F_{1\mathrm{y}}$,F_{ky},F_{kx},$F_{2\mathrm{y}}$,F_{GRF}) result from contact forces of the bearings. The torque τ actuates the system. Positions of the masses are given by x_{h}, x_A, x_K, x_B and x_{f}. The knee angle is represented by ϕ. 30

3.1. The segmented leg of MARCO Hopper II. (a) shows the leg in the current state. (b) shows it in the beginning of the thesis. The two segments thigh and shank got a length of l_{l} with a knee angle ϕ enclosed between them. Thigh and shank are connected by a roller bearing at the knee. The pulley is fixed on the shank with the cable glued on it. Positions of hip and foot are given by x_{h} and x_{f}. The foot and the hip are connected to the vertical sledge via linear bearings and to the segments via roller bearings. Also an additional mass m_1 could be added at the hip. The knee stop is realized via a cable, limiting the knee angle. Underneath the foot a force sensor is mounted measuring the ground reaction force F_{GRF}. The potentiometer position sensor is fixed to the foot. On the hip, near the joint, the IMU is mounted. 34

3.2. The drive-train of MARCO Hopper II. It consists of an electric motor with mounted transmission and encoder to measure the position of the motor. A ball screw converges the rotation of the motor in a translational movement of the carriages attached to the ball screw. The two carriages move on the rail and are connected to each other with a force sensor. The second carriage is attached to the Bowden cable which is connected to the pulley of the leg. 36

3.3. The different concepts of the connection in the drive-train are shown. In (a) a spring is fixed between the two carriages. SEA concepts can be investigated. In (b) the force sensor takes the place of the spring. A force-control approach is possible. Over the sensor the device for pre-loading the sensor is shown. 37

3.4. The force sensor used to measure the ground reaction force F_{GRF} [3]. 39

3.5. Drawing of the the adapter for the alternative sensor measuring the force in the drive-train. The long gray part connected with two drilled parts to the ITEM profile represents the sensor (beam load cell). The connection to the carriages is possible via the free threaded hole and the ITEM profile. 40

3.6. The signal of the force sensor without load. Measured is the force in the drivetrain F_{dt}. Different colors of the plot show the signal with a certain quantity of signal values used to calculate the average signal. 42

3.7. (a) Principle of a differential amplifier. It amplifies the differential signal $U_{e2}-U_{e1}$ by the factor K. [1](b) Implementation of the amplifier. The signals of both force sensors have to be amplified. Both are amplified with the same factor. The amplifier needs an own voltage source (down left). Sensors are provided with $U = 10$ V and the amplifier with $U = 25$ V. 43

3.8. [SIM] Motion- and force-patterns derived from a single mass oscillator model and a multi-body system model. The parameters are set to $m = m_1 = 1$ kg, $k = k_v = 36$ $^N/_m$,$x_0 = x_h = 0.2$ m. The solver ODE15s for the multibody-system brings some kind of damping in the simulated system. The oscillation ceases. For the solver ODE23 used for the multi-body model and ODE45 for the single mass oscillator the simulation results are equal. 44

3.9. Sketch of the model for the single mass oscillator. The structure got two degrees of freedom x and x_f. A spring with the rate k attached between the hip mass m and the foot mass m_4 drives the oscillation. The ground consists of a parallel spring with the rate k_g and a damper with the rate d_g. The ground forces effect the oscillator only during the stance phase. 46

3.10. Forces and torques introduced through the bearings in the simulation. Friction forces $F_{fr,h}$ and $F_{fr,f}$ and reaction forces of the stops F_{GRF}, $F_{GRF,h}$ and F_{HF} act on the foot and the hip. On the knee two torques take influence, the actuation torque τ_K and the torque by the knee stop τ_{ks}. 48

3.11. The course of the friction force influencing the ball screw. 53

3.12. [EXP+SIM] Comparison of the angular velocity $\dot{\phi}_M$ with attached transmission and ball screw of the test-bed (a) and the drive-train model (b). Both systems got a sinusoidal current input of $i_M = 3.5$ A and a frequency of $f = 1$ Hz. Simulation and experiment show similar apex values and the behavior around a zero velocity is also similar. 54

3.13. [SIM+EXP] Comparison of the position of the carriage x_{bs} with attached transmission and ball screw of the test-bed ((a), movement from inital position and (b), movement until hit of bed-stop) and the drive-train model ((c), movement from initial position). Both systems got a sinusoidal current input of $i_M = 3.5$ A and a frequency of $f = 1$ Hz. All three cover a distance of approximately $l = 0.03$ m during the oscillation. The behavior of the test-bed is not very steady. Reasons for this lie probably in a location dependent behavior of the ball screw and the non-ideal current control of the motor. 55

3.14. [SIM] The relationship between the velocity of the bearing and the friction force at the bearing of the hip $F_{fr,h}$. The parameters for the calculation of the friction force are $v_s = 0.001$ m/s, $\delta_s = 1$, $F_{c,h} = 4$ N, $F_{s,h} = 5$ N, $F_{v,h} = 5$ Ns/m. 60

3.15. [SIM+EXP] The comparison between the fall of the segmented leg in the simulation (solid line) and in an experiment (dashed line) from a certain release height $x_{h,0} \approx 0.5$ m. The parameters for the calculation of the friction force are $v_{s,h/f} = 0.001$ m/s, $\delta_{s,h/f} = 1$, $F_{c,h} = 4$ N, $F_{c,f} = 3.6$ N, $F_{s,h} = 5$ N, $F_{s,f} = 4$ N,$F_{v,h/f} = 5$ Ns/m. 61

4.1. [SIM] Comparison between the simulation of the multi-body system without (a) and with (b) an attached drive-train. The multi-body system without an attached drive-train acts like a single mass oscillator, as shown before. Both systems are set to the same desired torque at the knee. k_v is set to meet the condition of $\omega_{set} = 6$ rad/s. Shown are the time dependent positions of hip (solid line) and foot (dashed line). All friction forces in the system are turned to zero. The mass distribution is chosen to be like in the test-bed. The solver used is ODE23. 64

4.2. [SIM] Comparison between the simulation of the multi-body system without (a) and with (b) friction in the bearings of hip and foot. Both systems are set to the same desired torque at the knee. k_v is set to meet the condition of $\Delta h = 0.3$ m. Shown are the time dependent positions of hip (solid line) and foot (dashed line). The vertical solid line shows the position of the stretched leg/'take-off'(the leg hits the knee stop). The mass distribution is chosen to be like in the test-bed. The solver used is ODE23. 65

4.3. Control block diagram of the bang-bang control approach. The darker boxes show the basic (feedforward) control mechanism for a SLIP based virtual model control (VMC). The lighter loss compensation box is an optional mechanism that enhances the performance of the real system. It contains the additional current values $i_{\text{M-}}$ and $i_{\text{M+}}$ compensating the effects of the ball screw (see chapter 4.1.1). 66

4.4. [SIM] Comparison of hopping motions of the multi-body system with free fall and without (a) or with (b) the effect of friction at the linear bearings at the hip and the foot. Shown are the plots of the position of hip and foot. The vertical solid line shows the position of the stretched leg/'take-off'(the leg hits the knee stop). $\Delta h = 0.15$ m in this setup. The switching points are set to $x_{\text{h+}} = 0.45$ m and to $x_{\text{h-}} = 0.22$ m. Both systems can produce stable hopping motions. The solver used is ODE23. 67

4.5. [SIM] Comparison between the simulation of the multibody-system without (a) and with (b) attached drive-train. Friction forces are neglected. The bang-bang control method is used with $\Delta h = 0.15$ m. The switching points are set to $x_{\text{h+}} = 0.45$ m and to $x_{\text{h-}} = 0.22$ m. Shown are the time dependent positions of the hip and the foot. The vertical solid line shows the position of the stretched leg. The solver used in the simulation is ODE23. 68

4.6. [SIM] Comparison between the simulation of the multi-body system with drive-train and the consideration of friction forces (b) and the simulation of the segmented leg without drive-train but the same parameters for the friction models (a). The method of free fall is used with $\Delta h = 0.15$ m. The switching points are set to $x_{\text{h+}} = 0.45$ m and to $x_{\text{h-}} = 0.22$ m. Shown are the time dependent positions of the hip and the foot. The solver used in the simulation is ODE23. 69

4.7. [SIM+EXP] Comparison between the simulation of the multi-body system with drive-train and included friction effects (a) and an experiment with the same control parameters with the test-bed (b). The method bang-bang control is used with $\Delta h = 0.3$ m, $x_{\text{h-}} = 0.22$ m and $x_{\text{h+}} = 0.45$ m. The last ten seconds of the experiment are shown. The solver used in the simulation is ODE23. 70

4.8. Control block diagram of the continuous change of spring stiffness approach. As before the black boxes show the basic feed-forward mechanism of the system. An additional stiffness Δk is added to the system dependent on the positions of hip and foot. The compensation of losses in the real system can enhance the performance of the system. It contains the additional current values $i_{\text{M-}}$ and $i_{\text{M+}}$ compensating the effects of the ball screw (see chapter 4.1.1). 71

4.9. [SIM] Comparison of hopping motions of the multi-body system with a continuous change of spring stiffness during the upward movement. In (a) the friction in the bearings have been turned to zero. In (b) realistic friction forces act in the bearings. The switching points are set to $x_{\mathrm{h+}} = 0.45$ m and to $x_{\mathrm{h-}} = 0.22$ m. The solid black lines show the behavior with a $\Delta W = 0$ J, while the dashed black lines show the behavior with $\Delta W = 3$ J. A stable hopping motion is producable in the system without friction. The friction lets the oscillations decease. The solver used is ODE23. 72

4.10. [SIM] Comparison between the multi-body system with (b) and without (a) an attached drive-train. Both simulations were performed under the influence of friction forces. The approach to control the movement is a combination of constant energy supply with $\Delta W = 3$ J and free fall during the downward motion. A solid vertical line marks the position of the complete stretched leg. The solver used in the simulation is ODE23. 74

4.11. [SIM+EXP] Comparison of the simulated test-bed with attached drive-train (a) and the real test-bed (b). The approach to control the movement is a combination of constant energy supply with $\Delta W = 5$ J and free fall during the downward motion. A solid vertical line marks the position of the complete stretched leg. The solver used in the simulation is ODE23. 75

4.12. Control block diagram of the continuous change of spring stiffness approach with an additional PID-force-control part. As before the darker boxes show the basic feed-forward mechanism of the system. An additional stiffness Δk is added to the system dependent on the positions of hip and foot. The error resulting from the desired- and actual force is used to control the system with a PID-controller. The compensation of losses in the real system can enhance the performance of the system. It contains the additional current values $i_{\mathrm{M-}}$ and $i_{\mathrm{M+}}$ compensating the effects of the ball screw (see chapter 4.1.1). 76

4.13. [SIM] Comparison of the motion patterns of a segmented leg with drive-train under the influence of a force PID-control (solid line). The system without PID-control is shown by the dashed lines. The control parameters are set to $k_{\mathrm{P}} = 1$, $k_{\mathrm{D}} = 0.03$ and $k_{\mathrm{I}} = 33.3$. The vertical solid line shows the position of the stretched leg. The injected energy through the control is set to $\Delta W = 5$ J. The solver used in the simulation is ODE23. 79

4.14. [SIM] The integrated error $F_{\mathrm{err,\,int}}$ over the parameters k_{P} in the range 0.1 to 2 and k_{D} in the range 0.01 to 0.2. The simulation is performed over a time period of 3 seconds. There is a optimum point for the control parameters. The solver used in the simulation is ODE23. 80

4.15. [SIM] Comparison of the motion patterns of a segmented leg with drive-train under the influence of a force PID-control (solid line). The system without PID-control is shown by the dashed lines. The control parameters are set to $k_{\mathrm{P}} = 0.5$, $k_{\mathrm{D}} = 0.03$ and $k_{\mathrm{I}} = 18.75$. The vertical solid line shows the position of the stretched leg. The injected energy through the control is set to $\Delta W = 5$ J. The solver used in the simulation is ODE23. 81

4.16. [SIM] The integrated error $F_{\mathrm{err,\,int}}$ over the parameters k_{P} in the range 0.1 to 2 and k_{D} in the range 0.01 to 0.2. The simulation is performed over a time period of 3 seconds. The solver used in the simulation is ODE23. 83

4.17. [SIM] Comparison of the motion patterns of a segmented leg with drive-train under the influence of a force PID-control (solid line). The system without PID-control is shown by the dashed lines. The control parameters are set to $k_P = 2$, $k_D = 0.03$ and $k_I = 34$. The vertical solid line shows the position of the stretched leg. The injected energy through the control is set to $\Delta W = 5$ J. The solver used in the simulation is ODE23. 84

4.18. [SIM] The integrated error $F_{\text{err, int}}$ over the parameters k_P in the range 0.1 to 2 and k_D in the range 0.01 to 0.2. The simulation is performed over a time period of 3 seconds. $\Delta W = 5$ J and the current is limited to $i_M = 10.5A$. The solver used in the simulation is ODE23. 85

4.19. Control block diagram of an alternative to the continuous change of spring stiffness approach. The current is now controlled with an additional PID-force-control part. As before the darker boxes show the basic mechanism of the system. An additional stiffness Δk is added to the system dependent on the positions of hip and foot. The error resulting from the desired- and actual force is used to control the system with a PID-controller. The compensation of losses in the real system can enhance the performance of the system. 86

4.20. [SIM] Comparison of the motion patterns of a segmented leg with drive-train under the influence of a force PID-control. The control parameters are set to $k_P = 2$, $k_D = 0.03$ and $k_I = 34$. The vertical solid line shows the position of the stretched leg. The injected energy through the control is set to $\Delta W = 5$ J. The difference of both systems lies in the limitation of the current. In (a) the current is not limited, while in (b) the current is limited by $i_{M,,max} = 10.5$ A. The solver used in the simulation is ODE23. 87

4.21. Possible attachment place of a spring in the drive-train. The elasticity is attached between the carriages of the drive-train. The position of both carriages could be determined (the left one through the motor position, the right one with a potentiometer position sensor, comparable to the one used to measure the foot position). With these positions a force/position control could be implemented. . . 88

5.1. [SIM] Power consumption of the motor P_M (a) (calculated with the angular velocity of the motor ϕ_M and the load torque on the motor τ_M) and motor current i_M (b) during the hopping experiment shown in Fig. 4.11. The injected energy is tuned to be $\Delta W = 5$ J. 90

5.2. [SIM] Comparison of the relationship between ground reaction force and rest length of a single hop with a control tuned to $\Delta W = 1$ J. Friction forces are turned to zero. The single mass oscillator (a) has a mass of $m = 1$ kg. Different line-types stand for the different calculation methods for k. The solid line has a fixed value of k, a linear spring. For the dashed line the stiffness was changed in the fashion of the continuous change of stiffness with bang-bang control. The segmented leg (b) is tuned with its real masses. 91

5.3. Comparison of the patterns of motion and ground reaction force of the segmented leg and a human hopping motion. The human hopping data (a) is from [17]. Parameters of the experiment in (b) are $\Delta W = 1$ J and switching points of $x_{h+} = 0.45$ m and $x_{h-} = 0.22$ m. The solver used is ODE23. 92

5.4. [EXP] The course of the desired (black line) and the actual motor current (lighter line) during an experiment on the test-bed. 94

List of Tables

3.1. Properties of the segmented leg 35
3.2. Properties of the drive-train 38
3.3. Properties of *item* Profil 5 40x20, natur, Art. No. 0.0.370.04 40
3.4. Displacement of adapter due to maximum force 41
3.5. Properties of the segments "“shank"” and "“thigh"” used in the model 47
3.6. Properties of the roller bearings for the estimation of the friction torque 49
3.7. Properties of the motor used in the model 51
3.8. Properties of the transmission used in the model 52
3.9. Properties of the ball screw used in the model 56
3.10. Properties of the carriages in the simulation 57
3.11. Properties of the cable in the model 58
3.12. Properties of the ground models for hip and foot 59

4.1. Parameters of the experiments with bang-bang control and continuous change of the stiffness 75
4.2. Benchmark parameters of the experiment with bang-bang control and continuous change of the stiffness 77

Nomenclature

Greek symbols

α_{bs}	slope angle ball screw	[rad]
$\delta_{\mathrm{s,-}}$	stribeck exponential parameter	[-]
$\dot{\phi}$	angular velocity of the knee	$[\frac{\mathrm{rad}}{\mathrm{s}}]$
η_{bs}	efficiency of ball screw	[-]
η_{c}	efficiency of the cable	[-]
η_{T}	efficiency of motor transmission	[-]
ω_0	eigen frequency	$[\frac{\mathrm{rad}}{\mathrm{s}}]$
ω_{des}	desired frequency of an oscillation	$[\frac{\mathrm{rad}}{\mathrm{s}}]$
ϕ	knee angle	[rad]
ϕ_{bs}	angle of ball screw	[rad]
ϕ_{max}	maximum knee angle	[°]
ϕ_{M}	angle of the motor	[rad]
ψ	angle between upper leg segment and rail	[rad]
ρ_{al}	density of aluminum	$[\frac{\mathrm{kg}}{\mathrm{m}^3}]$
ρ_{bs}	friction angle ball screw	[rad]
ρ_{steel}	density of steel	$[\frac{\mathrm{kg}}{\mathrm{m}^3}]$
τ	torque at the knee	[Nm]
τ_{des}	desired torque	[Nm]
$\tau_{\mathrm{fr,f}}$	friction torque of the roller bearing at the foot	[Nm]
$\tau_{\mathrm{fr,h}}$	friction torque at the hip joint	[Nm]
$\tau_{\mathrm{fr,k}}$	friction torque at the knee joint	[Nm]
τ_{ks}	torque by the knee stop	[Nm]
τ_{L}	load torque motor	[Nm]
θ_{l}	mass moment of inertia leg segment	$[\mathrm{kgm}^2]$
θ_{bs}	mass moment of inertia ball screw	$[\mathrm{kgm}^2]$
$\theta_{\mathrm{M,sum}}$	effective mass moment of inertia motor	$[\mathrm{kgm}^2]$
θ_{M}	mass moment of inertia motor	$[\mathrm{kgm}^2]$
θ_{T}	mass moment of inertia transmission	$[\mathrm{kgm}^2]$

Latin symbols

Δx_{g}	displacement of the ground	[m]
$\dot{x}_{\mathrm{TO}}$	velocity during take off	$[\frac{\mathrm{m}}{\mathrm{s}}]$
A_{c}	cross section of the cable	$[\mathrm{m}^2]$
c_{switch}	logical operator control	[-]
d_{bs}	diameter shaft ball screw	[m]
d_{c}	diameter of the cable	[m]
d_{g}	damping rate ground model	$[\frac{\mathrm{Ns}}{\mathrm{m}}]$

d_k	damping constant of the knee stop	$[\frac{\mathrm{Nms}}{\mathrm{rad}}]$
d_M	damping constant motor	$[\frac{\mathrm{Nms}}{\mathrm{rad}}]$
E_al	E-modulus aluminum	$[\frac{\mathrm{kN}}{\mathrm{mm}^2}]$
E_kin	kinetic energy	[J]
E_pot	potential energy	[J]
E_steel	E-modulus steel	$[\frac{\mathrm{kN}}{\mathrm{mm}^2}]$
F_des	desired force	[N]
$F_\mathrm{err,int}$	integrated absolute force error	[N]
F_err	deviation from the desired force	[N]
$F_\mathrm{bearing,\ a}$	axial force roller bearing	[N]
$F_\mathrm{bearing,\ r}$	radial force roller bearing	[N]
$F_\mathrm{bs,v}$	velocity dependent force in the ball screw	[N]
$F_\mathrm{c,-}$	stribeck force parameter ‘coulomb’	[N]
$F_\mathrm{dt,M}$	maximum force by the motor after transmissions	[N]
F_dt	force between carriages in the drivetrain	[N]
$F_\mathrm{fr,f}$	friction force of the linear bearing at the foot	[N]
$F_\mathrm{fr,h}$	friction force of the linear bearing at the hip	[N]
F_GRF	ground reaction force	[N]
F_HF	force between foot and hip-stop	[N]
F_kx	force in x-direction at the knee joint	[N]
F_ky	force in y-direction at the knee joint	[N]
F_pl	pre-load on force sensor	[N]
$F_\mathrm{s,-}$	stribeck force parameter ‘stiction’	[N]
$F_\mathrm{v,-}$	stribeck force parameter ‘viscous’	[N]
g	gravitation constant	$[\frac{\mathrm{kg\ m}}{\mathrm{s}}]$
h_l	height of leg segment	[m]
$i_\mathrm{M+}$	additional motor current to compensate friction, positive	[A]
$i_\mathrm{M-}$	additional motor current to compensate friction, negative	[A]
$I_\mathrm{y,iP}$	area moment of inertia ITEM profile	$[\mathrm{cm}^4]$
i_bs	transmission ratio ball screw	[-]
$i_\mathrm{M,\ max}$	nominal current	[A]
i_M	motor current	[A]
i_T	transmission ratio motor transmission	[-]
K	amplification factor differential amplifier	[-]
k	spring rate	$[\frac{\mathrm{N}}{\mathrm{m}}]$
$k_\mathrm{bs,v}$	parameter ball screw damping alternative	[N]
k_c	stiffness of the cable	$[\frac{\mathrm{N}}{\mathrm{m}}]$
k_E	rotation speed constant motor	$[\frac{1}{\mathrm{V\ min}}]$
k_g	spring rate ground model	$[\frac{\mathrm{N}}{\mathrm{m}}]$
k_M	torque/current constant motor	$[\frac{\mathrm{mNm}}{\mathrm{A}}]$
k_v	spring rate of the virtual spring	$[\frac{\mathrm{N}}{\mathrm{m}}]$
l_0	rest length of the spring single mass oscillator	[m]
l_leg	leg length	[m]
l_bs	length shaft ball screw	[m]
l_c	length of the cable	[m]

l_{iP}	length of ITEM profile	[m]
l_{l}	length of leg segment	[m]
L_{M}	inductance motor	[mH]
m	mass of single mass oscillator	[kg]
m_1	mass at the hip	[kg]
m_2	mass of one leg segment	[kg]
m_3	mass at the knee	[kg]
m_4	mass at the foot	[kg]
m_{bs}	mass shaft ball screw	[kg]
n_{bearing}	rotational speed of roller bearing	$[\frac{\mathrm{U}}{\mathrm{min}}]$
p_{bs}	slope shaft ball screw	[m]
R	electric resistance	[Ω]
r_{bs}	radius shaft ball screw	[m]
R_{M}	internal resistance motor	[Ω]
r_{p}	effective radius of pulley at the knee	[m]
T	length of an experiment	[s]
T_{bearing}	operating temperature roller bearing	[°C]
U	voltage	[V]
U_{a}	output voltage differential amplifier	[V]
U_{e1}	output voltage 1 sensor	[V]
U_{e2}	output voltage 2 sensor	[V]
U_{Sout}	output voltage sensor	[V]
$v_{\mathrm{s,-}}$	stribeck velocity parameter	$[\frac{\mathrm{m}}{\mathrm{s}}]$
w	displacement of a bended beam	[m]
w_{l}	width of leg segment	[m]
x	position of single mass oscillator	[m]
x_0	initial position of mass m	$[m]$
x_2	foot position of the single mass oscillator	[m]
x_{c2}	position of the carriage attached to the cable	[m]
$x_{\mathrm{h+}}$	switching point control, high	[m]
$x_{\mathrm{h-}}$	switching point control, low	[m]
x_{bs}	position of ball screw	[m]
x_{f}	position of the foot	[m]
$x_{\mathrm{h,0}}$	initial hip position	[m]
x_{hs}	position of the hip stop	[m]
x_{h}	position of the hip	[m]
x_{max}	apex height of single mass oscillator	$[m]$

1 Introduction

1.1 Preface

Human machine interaction holds many possibilities but also challenges. The interfaces of such must be thought through thoroughly. Especially in the field of robotics and assistive devices like orthoses and prostheses a high level of harmonic interaction has to be reached, to support humans in the best possible way.

Research in the field of locomotion and the development of legged robotics holds the possibility to use inspiration from biological role models to improve this interaction. Control strategies for the actuation of these systems have to be simple and inherit a high level of performance. The search for and development of robust control strategies, which work with a minimum of sensor information, a high level of robustness and a low energy consumption, are important goals to reach.

For a long time assistive devices used to be passive and supported the human in a way, which is not comparable to real legs. Active adaptive assistance devices can improve the performance, usability and acceptance of the users and raise the life quality of people dependent on these devices.

To understand basic relationships and to test actuation and control strategies, robotic legs are built. One of these robotic legs lays the basis of this thesis.

1.2 Models of human hopping/locomotion

To built legged robots or assistive devices for humans, the principles behind legged locomotion have to be understood. It has been shown that one basic part of the human locomotion is the hopping motion [28]. An analysis and understanding of this motion may lead to the ability of building and controlling leg-like structures.

The segmented leg is able to perform a linear translational motion of the body through the combination of rotational movements of the segments. A hopping motion is a complex non-linear control task if the concentration lies on a separated control of the different driven joints. A simplified description of the motion is helpful to investigate control strategies.

Different templates of the human hopping motion have been developed to describe the complex inner behavior with its basic effects and behavior of the system "“leg"”, respectively the motion of the whole human body. Templates describe "“[...] the simplest model (least number of variables and parameters) that exhibits a targeted behavior."” [11]. Some of the templates, used to describe human locomotion, will be shown in the next section.

1.2.1 Spring loaded inverted pendulum

The spring loaded inverted pendulum (SLIP) model has been developed by *Blickhan* [8]. The basic idea is to describe the human running and hopping motions through the motion and force effects of a single mass oscillator.

The SLIP model consists of one mass m and an attached spring with the stiffness k and the rest length l_0. Because the model is also able to describe running motions, the angle of attack of the spring in respect to the ground α is also an important parameter. For a hopping motion this angle is equal to zero. The position of the mass corresponds to the position of the center of mass (COM) of the human (near to the hip) while the end of the spring determines the contact point of the human with the ground, the foot.

Despite its simplicity the SLIP model is able to describe the behavior of a human or an animal in running or hopping motions [8]. The compared entities are the movement pattern of the position of mass, respectively the COM of the human/ animal, and the ground reaction force as the measurable effect on the environment. Certain ranges of locomotion parameters like the "“chosen"” frequencies and resulting heights of the hopping can be explained through the examination of the SLIP model.

Advanced approaches based on the SLIP model

Further developments of the SLIP model have been made. The basis of the single mass oscillator has been extended to explain certain effects during human locomotion in a more precise way. One example is the ESLIP model by *Ludwig* et al. [19]. In this model stiffness k and rest length l_0 are no longer fixed values but are adapted through experimental measured changes of the system energy after each step. A matching sequence of steps can be calculated, which is not possible by the energy conservative SLIP model.

Another method is the variable leg spring (VLS) method [26] by *Riese* and *Seyfarth*. The SLIP parameters spring rate k and rest length l_0 are varied during the stance phase of the hopping/running motion. Increasing stiffness and decreasing rest-length during this phase result in stable hopping motions with and also without the consideration of damping effects. The findings are valid for a wide range of spring parameters.

A third approach, mentioned at this point, is a method in which the spring stiffness is varied. In [17] energy management methods working with a variation of spring stiffness during ground contact where presented by *Kalveram* et al. Stable hopping motions, even in perturbed cases, could be achieved.

More examples of advanced templates can be presented. In this work control strategies for a segmented leg shall be developed. First examinations will be made with the simplest templates before a possible enhancement of performance through advanced models will be examined.

1.2.2 Inverted pendulum

A second simple mathematical model for the explanation of human locomotion is the inverted pendulum or "“ballistic walking"” model by *Mochon* and *McMahon* [21]. In this model the leg length is fixed during the locomotion process. A running gait is realized by alternate swing phases of the two legs driven by initial conditions, produced by muscle forces, and the influence of gravitation on the swinging leg.

This model can not be used to realize hopping motions and, therefore, is not regarded further on.

1.3 Test-beds legged locomotion

In the past, different test-beds for the research on legged locomotion have been built. Mostly robotic systems that come near to a biological role model were assembled. There are a lot of different approaches from single-leg robots [31] over different two legged robots (e.g. "“BioBiped"” [30] and [25], "“Spring Flamingo"” [24] or "“ATLAS"” by Boston Dynamics) to robots with four or more legs (e.g. BigDog by Boston Dynamics).

For the research on hopping motions, a test-bed with only one leg is necessary. For this purpose, the leg has to move only in one direction. It is possible to fix the segmented leg in space and to leave only two 1-D degrees of freedom for each, the foot- and hip position. Through this systems simple and robust structures are feasible. Two of those hopping research test-beds will be presented. Also a third recent test-bed will be described for its closeness to the topic of this work.

1.3.1 Marco Hopper

In order to investigate different energy management methods inspired from human hopping motions, a test-bed called MARCO (Mechanical adjustable reflexive-compliant) Hopper was developed [29](see fig. 1.1). The structure of MARCO comes close to the SLIP model, for the motor is controlled to act in a spring-like behavior. Masses are only moved in one direction. Therefore, the test-bed does not come very close to the structure of a real leg.

The one actuator driving the system can mimic the behavior of different drive-train properties through suitable control laws. For instance, it is possible to influence the control signal in the motor to reproduce muscle-reflex dynamics and to produce stable hopping motions [29]. Different physical drive-train setups can not be realized.

In these points lie the limitations of the test-bed. Energy management methods could be investigated but the research on segmented structures (near to real legs) and variable drive-trains is not possible. An extended test-bed is necessary, which does not inherit these limitations.

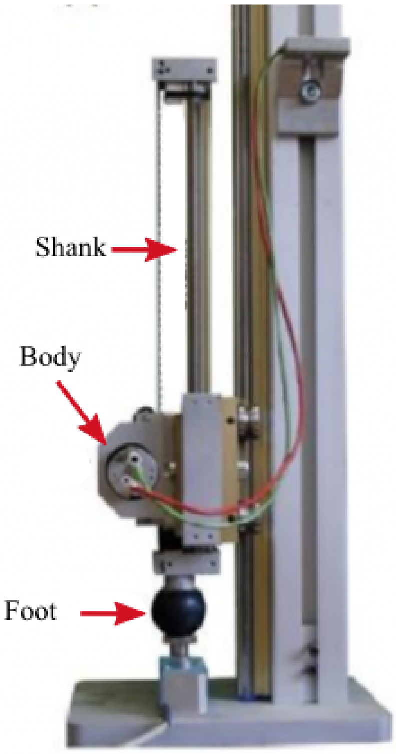

Figure 1.1.: The test-bed MARCO Hopper consists of a foot, a shank and a body. The weight of the motor and the attached transmission serves as the body mass. A tooth-belt connected to the ends of the shank and the output shaft of the motor makes it possible to move the motor up and down the shank. A second rail guides the whole structure in the vertical direction. The foot is equipped with a ball of highly damping material, to absorb the impact energy of the landing and prevent damages on the structure [17].

1.3.2 Development of the test-bed Marco Hopper II

The test-bed MARCO Hopper II was developed during an advanced design project (ADP)[1] in the year 2013 [9] at TU Darmstadt. The task of this student project with the title "'Human motions and robotics"' was the development of a demonstrator for lessons and research on bio-inspired actuator concepts. One purpose for the test-bed is the research on serial elastic actuator concepts. As shown in section 1.3.2 serial-elastic-actuators can be used to model biological muscles.

The role model for the actuated biological structure is the human leg. Its structure has been reduced and the essential parts have been built in the test-bed. Compared to an actual human leg, the concept of actuation was strictly simplified. The actuation of the test leg takes only place on the knee. Through the use of a cable in combination with an electric motor and an attached transmission-system (drive-train) a torque in the knee is generated. This torque moves the leg and can be used to control squats and hopping motions.

The figure 1.2 shows a photo of the test-bed. The demonstrator consists of different mechanical parts representing structures in a real human leg. Thigh and shank are represented by two metal

---

[1] http://wiki.ifs-tud.de/adp_laufrobotik/adp_2013

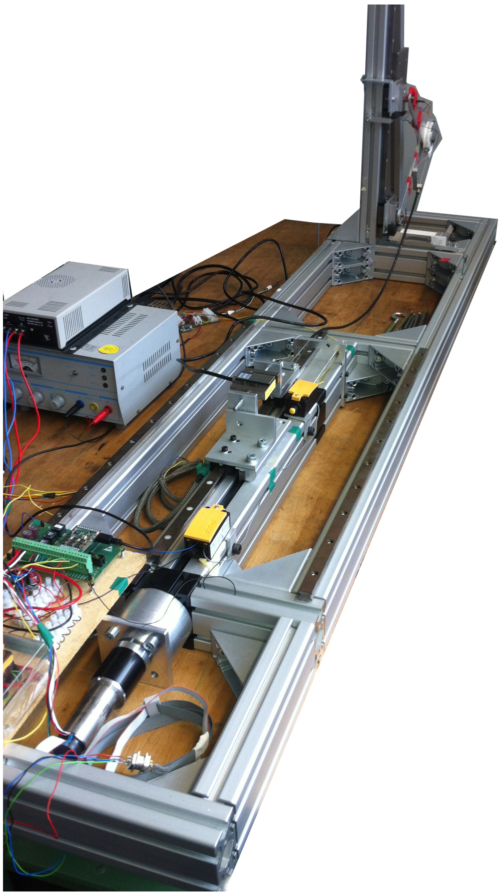

Figure 1.2.: Picture of the test-bed Marco Hopper 2.0

segments. The hip-, knee- and ankle-joint are given by three ball-bearings. The design of the knee contains an pulley that guides the cable around the knee to produce the driving torque. Hip and foot are guided by linear bearings.

Only motions in the vertical direction by hip and foot are possible. The position of the hip and the foot in the vertical direction are tracked by potentiometer position sensors. The motions of hip and foot are limited by mechanical stops in the negative vertical direction. These "“rest"” positions determine the initial condition of every motion of the leg.

During the project only a concept of the test-bed has been developed. The construction was performed by the staff of the IMS subsequent to the ADP. When the project was over, a control for the test-bed has not been developed yet.

This thesis bases on the test-bed MARCO II. All control strategies, models and parameter choices were developed for MARCO II. General findings can be used for other projects and the abstract idea of hopping motions. The results can be used to improve the performance of MARCO II and also other legged robots.

Series elastic actuators

The test-bed MARCO Hopper II serves also as a platform for testing the effects of different actuating strategies. Different muscle models can be expressed through the combination of mechanical components like springs and dampers shown by *Hill* [16] or in an extended form by *Haeufle* [15].

The most simple approach is to combine an actuator in series with a spring. Through this measure the biological functions of muscle and tendon are represented in a first approximation.

The series elastic actuator (SEA) [32] concept serves also additional purposes. A very important goal regarding virtual model control is the need of actuators with a low output impedance. The use of SEA results in a low impedance of the actuators as seen in [24]. A second reason is the possibility that the use of SEA contains a lesser energy consumption than direct driven actuators. As shown in [9] a spring in series with the actuator can reduce the needed motor energy per jump. Third, elasticity in series with an actuator protects actuators from impacts. Peaks of force (e.g. when driving in a rigid resistance) can be reduced.

All this influences and theories can be examined with the possibilities given by the test-bed MARCO II.

1.3.3 Single legged robot with variable knee stiffness - L-MESTRAN

Recently *Vu* et al. [31] published a paper containing research results on a hopping robot very similar to the one studied in this thesis. The purpose of their research was to measure the influence of an actuator with variable stiffness, especially on the energy consumption of the robot. Differences to the robot examined in this thesis are the actuated parts, the movement of the structure and the control mechanisms.

The segmented leg of the presented robot has also two links but in difference to MARCO II two actuated joints. The hip joint is driven by torque, provided by an electric motor. A system that provides variable stiffness is connected to the knee. The movement of the robot is not restricted to a vertical movement. It is also able to move on a circle in the horizontal direction. Motions of the robot are controlled by the torque, provided at the hip (position control policy of the hip [31]). The spring at the knee is a passive structure that is not dynamical adjustable.

There are some important findings of the paper:

- there are optimal parameter settings regarding the energy consumption of the actuator for the knee stiffness for different stride frequencies, therefore these should also exist for different hopping frequencies [31][p. 12]
- "“the model-based analysis suggested that the energy efficiency of hopping locomotion is significantly related to the eigen-frequency of the system, which can be used as an effective indicator of the adjustment of knee stiffness"” [31][p. 14]

The results gained with the variable knee stiffness can be applied to the variable drive-train of MARCO II. To make this possible eigen-frequencies of the system have to be calculated and evaluated.

1.4 Virtual model control

Virtual model control forms the basic idea of the control approach presented in this thesis. The concept has been developed by *Pratt* in [23] as an simplified approach to control legged robots. A first application is found in the control of "‘spring turkey"', a bipedal robot.

The idea behind virtual model control is to attach virtual components to a real structure to realize a desired behavior. Existing actuators, in this case actuators producing joint torques, are controlled by a law that mimics the effects of the virtual components. In the choice of the virtual component the developer is not constrained by possibilities feasible in reality. The virtual component can inherit all thinkable properties.

"‘This control technique uses simulations of virtual mechanical components to generate actuator torques (or forces) thereby creating the illusion that the simulated components are connected to the real robot"'[23]

Benefits of virtual model control are:

- "‘no matrix or function inverses need be computed for serial links"'[23][p. 12]
- "‘all equations can be precomputed in closed form and optimized"' [23][p. 12]
- "‘multiple virtual components can be independently computed and superposed since their outputs, joint torques, are linearly additive"' [23][p. 12]

Pratt presents five steps to implement virtual components to a controlled system [23][p. 17]:

1. definition of the virtual model reference frames
2. computation of the forward kinematics
3. calculation of a Jacobian Matrix
4. computation of the joint torques
5. definition of the virtual model force function

Three coordinate systems are necessary for each virtual component of a virtual model control approach - the "‘Action Frame"', the "‘Reaction Frame"' and the "‘Reference Frame"' [23][p. 17]. They describe the "‘attachment"' points of the virtual component and a global coordinate system, in which forces and motions are described.

Forward kinematics means that through the knowledge of all degrees of freedom of the serial manipulator the position of the end of the chain is clear. It is described by the rotation matrices, which contain the information about the rotation of each coordinate system attached to one rigid body to the next in the chain.

The Jacobian Matrix relates joint velocities to Cartesian velocities [10][p. 150]. It is also used to transform generalized forces to joint torques [23][p. 19].

Next, the joint torques are computed. The Jacobian Matrix is used to transform the forces produced by the virtual component to joint torques. The computed joint torques will have the same effect as the virtual forces by the virtual component. It is important that the forces can be realized using the available joint actuators. Through looking at the Jacobian Matrix it can be decided whether or not a force can be realized [23][p. 19].

The next step is to find a relation between the relative displacement and rotations of the action and reaction frames and the generalized forces to be applied to the action frame. This force function that describes virtual forces can be controlled by any desired control method [23][p. 20].

The method presented can be used to control very complicated structures with a lot of dependent actuators and degrees of freedom. A control approach to control MARCO II performing hopping motions needs only a single virtual component. Therefore the mentioned steps to derive a virtual model control law become very simple and the presented implementation steps have not to be performed.

In this thesis the virtual model control approach is performed by the equal setting of different dynamic systems. The effect of a virtual component on a chosen degree of freedom shall be the same as the effect, which the real actuator has. This procedure serves to hold the clearness of the method on a high level. The results of both procedures are the same.

2 Development of models for the control of hopping motions

The starting point of this thesis is the concept of the test bed MARCO II [9] and a realized version of it.

To prepare the start-up of the test bed a control has to be developed and implemented. In preparation for this task and to have the possibility to test control algorithms, a model of the test bed has to be created. Also mathematical models of ascending complexity have to be developed, which make make it possible to use templates of hopping motions in complex systems. In this chapter equations, which describe the laws used to control a stable hopping motion, are derived.

The model equations of the problem will be implemented in *Matlab/Simulink*. Parts of the models will be realized by *SimMechanics*, the multi-body simulation environment provided by *Matlab*. The control of the multi-body system will be developed with *Matlab/Simulink*. All figures shown will have a sign determining if the result is from a simulation ([SIM]) or from experiment ([EXP]). This procedure was chosen in the style of [23].

There are different parts of the models that are necessary to create a valid model of the reality.

1. **Structure of the test bed (links, bearings, mechanical constraints):**
   This part contains all mechanical parts of the test bed. Important for a realistic simulation model are correct assumptions regarding mass-distribution, friction and damping by the bearings and a correct modeling of the constraints (in this case parameters for damping and deformation). Most of the data is obtained by data sheets of the used parts. If necessary there have to be experiments to determine single parameters.

2. **Sub-model for the contact between ground and the "‘foot"’:**
   The contact between foot and ground is either constant (during squats) or divided in contact- and flight-phases (during hopping). In both cases the contact between foot and ground has to be modeled. Depending on the dynamic values of the system the ground reaction force gets higher (or lower) than in the static case [27]. The impact through the landing after each jump has to be regarded and modeled correctly.

3. **Sub-model for the actuation of the knee (drive-train model):**
   The knee is the only actuated part of the structure. Therefore, the control variable will be the torque generated at the knee. A cable, different linear bearings, a transmission and in an extended model even springs or dampers connect the actuator with the knee. All these parts and the actuator itself have to be modeled. The realistic behavior of the model can only be obtained, if all this influences are considered.

The complexity of the sub-models and models will increase during the development of the different approaches. One first step is to develop a theory for the control of the knee torque in a manner that produces hopping motions. A simple template model for hopping motions (the

SLIP model) is investigated to gain a desired behavior by the adjustment of its parameters. This behavior is transferred to more realistic models that come closer to reality through every step.

For the development of dynamic equations basic ideas from the textbooks "“Technische Mechanik"” 1 [12], -2 [13] and -3 [14] have been used.

2.1 Dynamic equations of models with ascending complexity - squats

The basis of a hopping motion is given through an oscillating movement of the hip between initial position $x_{\mathrm{h},0}$ and the apex point $x_{\mathrm{h},\max}$ (squats). A hopping motion is given if a flight phase (the foot leaves the ground for a certain time) is added to this pattern. An understanding of the laws describing squats is necessary to expand the controlled movement to hopping.

2.1.1 Harmonic oscillator with single mass

The sketch of a single mass oscillator is shown in Fig. 2.1. It consists of one mass m with one degree of freedom x. The movement happens only in this direction. Attached to the mass is a spring with the rate k and the rest length l_0. A certain deflection of the spring results in a force F attacking the mass and an equal ground reaction force F_{GRF}. The importance of this model lies in the equivalence of the behavior of this oscillating system to a human's hopping pattern, as shown by *Blickhan* in [8]. The derived movement and ground reaction force serves as template respectively benchmark for other systems that should produce hopping motions.

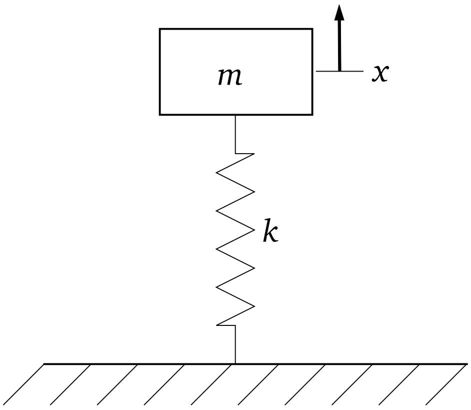

Figure 2.1.: Sketch of a single mass oscillator. The mass m has got one degree of freedom x. A spring with the rate k and the rest length l_0 attached to the mass drives the oscillation of the system. The lower end point of the spring never leaves the ground.

The equation of motion for this system is described by:

$$\ddot{x} = \left(\frac{k(l_0 - x) - mg}{m}\right)$$
$$\text{with:} \qquad (2.1)$$
$$\omega_0 = \sqrt{\frac{k}{m}}$$

ω_0 describes the eigen-frequency of the system and therefore the oscillating behavior. The system's behavior is influenced by the mass m, the rest length l_0 and the spring-stiffness k. The initial conditions, like the initial position x_0 and the initial velocity $\dot{x}_0$, also influence the movement pattern of the system. Throughout this thesis the initial velocity is set to zero. A movement always starts from a rest position.

In the real test bed the masses will have fixed values. Therefore the system's behavior can only be changed by adjusting k or l_0. Since both values will only be virtual values with no real counterpart they have not to be fixed. A variable stiffness or rest length is possible. The calculation of the "‘correct"’ value of k depends on the wished movement.

Adjustment to a desired apex height of the oscillation

The beginning of a hopping motion is given if the mass m reaches the rest length of the spring and the velocity of the mass $\dot{x}$ is bigger than zero. For the spring is not attached to the ground, no force in negative x-direction besides gravitation takes an effect on the mass. The kinetic energy at this point sets the height of the hopping motion if losses are neglected.

To reach a certain apex height $x_{\max}$ from an initial position x_0 and with a rest length of l_0 the necessary value for k has to be derived from the equation of motion of the system. For a single mass oscillator it can be written:

$$\begin{aligned} x &= \left(x_0 - l_0 + \frac{g}{\omega_0^2}\right)\cos(\omega_0 t) + l_0 - \frac{g}{\omega_0^2} \\ x &= x_{\max} \textbf{ if: } \omega_0 t = \pi \\ x_{\max} &= 2l_0 - x_0 - \frac{2g}{\omega_0^2} \\ \omega_0^2 &= \frac{2g}{2l_0 - x_0 - x_{\max}} \end{aligned} \tag{2.2}$$

The value of k for an apex height $x_{\max}$ is now given by:

$$k = \frac{2gm}{2l_0 - x_0 - x_{\max}} \tag{2.3}$$

There are borders for a reasonable behavior of the oscillation. The denominator of eq. 2.3 sets this borders. It always has to be positive and not equal to zero. A negative stiffness k is not reasonable and a denominator equals zero would produce unsteadiness.

$$x_{\max} < 2l_0 - x_0 \tag{2.4}$$

So far movements that do not go further than $x_{\max} = l_0$ are considered. A negative value of $x_{\max}$ does not make sense under the assumption of hopping motions. So the lower and upper limit of the apex height are set.

The same procedure could be used for more complex systems. All that is needed is the equation of motion of the top mass.

Adjustment to a desired frequency of the oscillation

If the resulting frequency of the motion is of interest, the equation of motion of the system is also needed to identify the eigen-frequency ω_0. For a desired frequency ω_{des} the spring stiffness is determined by:

$$k = \omega_{\text{des}}^2 m \tag{2.5}$$

The apex height resulting from a certain frequency of movement with fixed values for l_0, x_0 and ω_{des} is calculated by:

$$x_{\max} = 2l_0 - x_0 - \frac{2g}{\omega_{\text{des}}^2} \tag{2.6}$$

For a limited movement area there is a certain range of ω_{des} that leads to useful results. An apex height lower than zero is not reasonable for the given problem of hopping movements. The lower border ω_{des} is determined by:

$$\begin{gathered} 0 < 2l_0 - x_0 - \frac{2g}{\omega_{\text{des}}} \\ \omega_{\text{des}} > \sqrt{\frac{2g}{2l_0 - x_0}} \end{gathered} \tag{2.7}$$

The upper border is given when ω_{set} reaches infinity. An apex height of the movement is then given by:

$$x_{\max} = 2l_0 - x_0 \tag{2.8}$$

This apex height is only valid for a spring attached to the ground. The movement is limited by the rest length of the spring for resulting squats.

Another important frequency is the point where a hopping motion begins. This point is set by the condition that the apex height of the movement gets higher than the rest length of the spring. The resulting border-frequency is set by:

$$\begin{gathered} w_{\text{des}} > \sqrt{\frac{2g}{l_0 - x_0}} \\ k > \frac{2gm}{l_0 - x_0} \end{gathered} \tag{2.9}$$

Tuned systems that meet this condition produce hopping motions if the spring is not attached on the ground.

2.1.2 Single mass oscillator with flight phase

If the frequency of the motion is set slightly above the frequency mentioned in 2.9, the apex point is higher than the rest length of the spring. For the spring is not attached to the ground, the foot leaves the ground and a flight phase is initiated.

The height of this hop depends on the velocity the mass has at take off $\dot{x}_{\mathrm{TO}}$. Through the comparison of kinetic and potential energy of the single mass oscillator it can be shown that the apex height of the flight (the hopping height) is given by:

$$\begin{aligned} E_{\mathrm{kin,TO}} &= \frac{1}{2} m \dot{x}_{\mathrm{TO}}^2 \\ E_{\mathrm{pot,xmax}} &= mg(x_{\mathrm{max}} - l_0) \\ E_{\mathrm{kin,TO}} &= E_{\mathrm{pot,xmax}} \\ x_{\mathrm{max}} &= \frac{1}{2g} \dot{x}_{\mathrm{TO}}^2 + l_0 \end{aligned} \tag{2.10}$$

The velocity the mass has at take off can be determined by:

$$\dot{x}_{\mathrm{TO}} = -\omega_{\mathrm{des}} \left(x_0 - l_0 - \frac{g}{\omega_{\mathrm{des}}^2} \right) \sqrt{1 - \left(\frac{g}{\omega_{\mathrm{des}}^2 x_0 - \omega_{\mathrm{des}}^2 l_0 + g} \right)^2} \tag{2.11}$$

Through the adjustment of a proper value for ω_{des} and, therefore, k the hopping height of a single mass oscillator can be determined.

In reality there are always energy losses during hopping movements. The energy balance between kinetic and potential energy is given no more. Therefore, an ideal border value for the hopping height is presented in eq. 2.10.

Summary single mass oscillator

The equations derived from the single mass oscillator and especially the border frequencies are important as soon it is possible to control more complex systems in the fashion of a single mass oscillator. The same behavior (desired frequencies, apex points, border frequencies) can be applied on these systems. Some laws that have been developed (e.g. hopping height through the kinetic energy) may change for the changed proportion of masses. But they give directions for the choice of parameters and the resulting behavior non the less.

2.1.3 Multi-body system with one mass

For the geometries of the robot are more complex than of the single mass oscillator the true geometry should be regarded. For reasons of simplicity it gets started with a single mass with one translational degree of freedom x and two mass-less links with the length l_l representing the segments of the leg (shown in Fig. 2.2).

The first link is attached to the mass and encloses an angle ψ with the translational direction x. The second link is connected to the first link at the knee (enclosed angle ϕ). The segment is also attached to the ground, for the leg should not leave the ground in this phase. The angle between the lower segment and the vertical direction is also ψ. Geometric constraints set the proportion of the angles and the position of the mass to:

$$\begin{aligned} \psi &= \frac{\pi}{2} - \frac{\phi}{2} \\ x &= 2\, l_1 \sin\left(\frac{\phi}{2}\right) \end{aligned} \tag{2.12}$$

The actuation of the whole structure is implemented in the knee, the point where the two links are connected. A torque τ drives the movement of the multi-body structure.

Multi-body system driven by an ideal torque

So far an ideal torque τ for the actuation of the whole structure is assumed. In this example the resulting movement resulting by this method of actuation will be shown. The regarded multi-body system is shown in Fig. 2.2. There is only one mass in this system. The links will be regarded mass-less and rigid. So the resulting movement of the mass is made comparable to a single mass oscillator, which was introduced before.

As to see in Fig. 2.2 a spring is attached between the mass and the ground. This spring is a virtual spring which causes no actual force on the mass or the ground. The effect the torque τ has on the mass is supposed to be the same effect the spring would have. This is the central idea of the virtual model control.

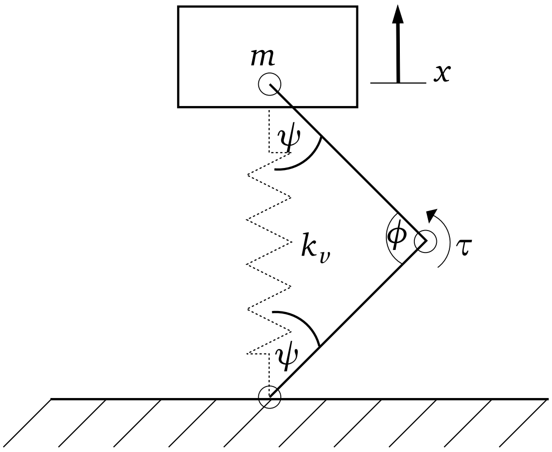

Figure 2.2.: Sketch of the multi-body system driven by an ideal torque τ. The structure got one degree of freedom x. The torque τ should act like a force by the virtual spring with the stiffness k_v.

The acting forces on the links of the system are displayed in Fig. 2.3. Through a cut of the system at the knee and the bearings of hip and foot the acting forces are exposed. The mass on top causes a gravitational force mg on this point while the constraint of the movement of the mass causes a reaction force $F_{1\mathrm{y}}$. At the knee there is a torque τ at the upper link introduced. The intersection of the knee exposes the reaction forces F_{kx} and F_{ky}. Also the movement of the foot is constrained in one direction. The reaction forces of the bearing and the ground are given by $F_{2\mathrm{y}}$ and F_{GRF}. Through the equations of equilibrium of the forces and the torques, the equation of motion for the top mass can be found. The equilibrium of forces and torques leads to the following equations. Super-scripted numbers relate to the described sub-system in Fig. 2.3.

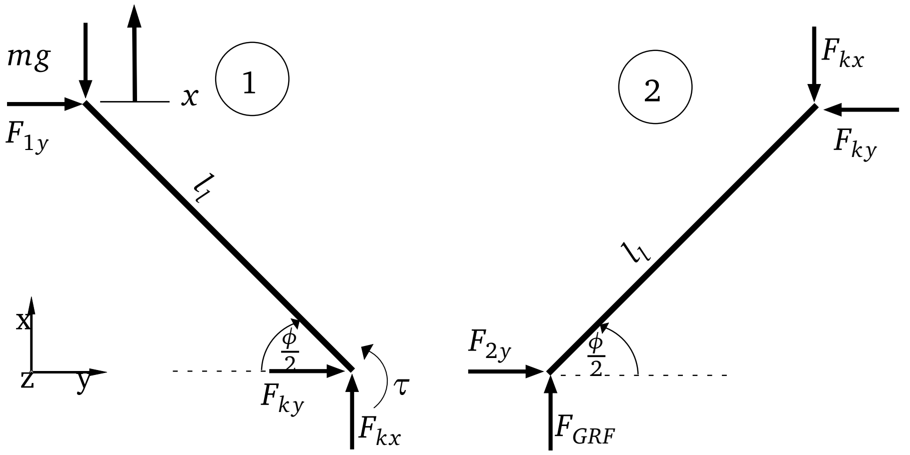

Figure 2.3.: Sketch of the multi-body system of two segments with the length l_l driven by an ideal torque τ. The system is divided in two parts through a cut at the knee and underneath the foot. Forces acting at the section planes are shown.

$$
\begin{aligned}
&\Sigma F_\mathrm{x}^1 : \; m\ddot{x} = F_\mathrm{kx} - mg \\
&\Sigma F_\mathrm{y}^1 : 0 = F_{1\mathrm{y}} + F_\mathrm{ky} \\
&\Sigma \tau^1 : 0 = -F_\mathrm{kx}\cos\left(\frac{\phi}{2}\right) l_\mathrm{l} - F_\mathrm{ky}\sin\left(\frac{\phi}{2}\right) l_\mathrm{l} + \tau
\end{aligned}
$$

$$
\begin{aligned}
&\Sigma F_\mathrm{x}^2 : 0 = -F_\mathrm{kx} + F_{2\mathrm{x}} \\
&\Sigma F_\mathrm{y}^2 : 0 = F_{2\mathrm{y}} - F_\mathrm{ky} \\
&\Sigma \tau^2 : 0 = F_\mathrm{kx}\cos\left(\frac{\phi}{2}\right) l_\mathrm{l} - F_\mathrm{ky}\sin\left(\frac{\phi}{2}\right) l_\mathrm{l}
\end{aligned}
$$

Through some transformations the equation of motion for the top mass m follows:

$$
m\ddot{x} = \frac{\tau}{2\cos\left(\frac{\phi}{2}\right) l_\mathrm{l}} - mg \tag{2.13}
$$

The torque τ sets the mass in motion. One goal is to gain a behavior of the structure similar to a single mass oscillator with one spring. Therefore, the driving terms of the single mass oscillator and the multi-body system, with the rest length l_0 of the spring have to be equal.

$$
\frac{\tau}{2\cos\left(\frac{\phi}{2}\right) l_\mathrm{l}} = k(l_0 - x) \tag{2.14}
$$

If the torque τ in the following form is added at the knee, the structure moves like a single mass oscillator. The generation of the torque depends only on the degree of freedom of the mass x, for ϕ and x are dependent values. The stiffness k is changed to k_v, for it is now representing a virtual component in the multi-body system.

$$\tau = 2\cos\left(\frac{\phi}{2}\right) l_1 k_\mathrm{v}(l_0 - x) \tag{2.15}$$

The necessary requirement is that the mass is the same in both systems.

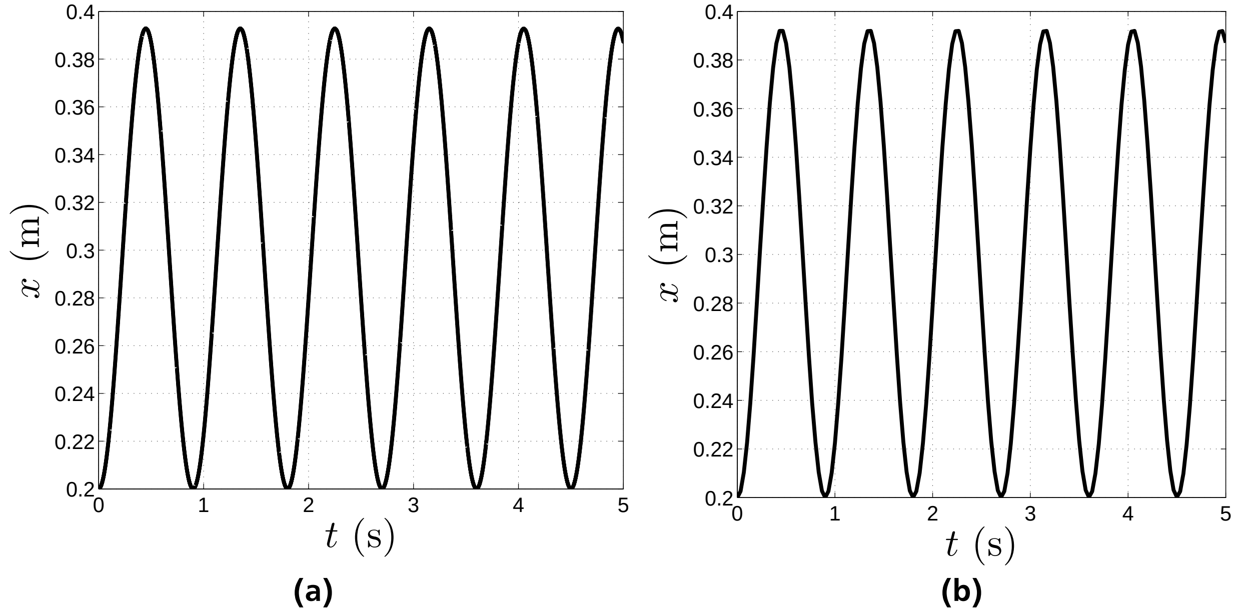

(a) **(b)**

Figure 2.4.: [SIM] Comparison of the oscillation of the single mass oscillator (a) and the multi-body system (b). The stiffness of the spring k_v is adjusted for a stable oscillation of $\omega = 7$ rad/s. The initial position of the mass is $x = 0.2$m and the rest length $l_0 = 0.5$m. The solver used for the single mass oscillator is ODE45 and for the multi-body system ODE23. The resulting oscillations are equivalent.

The comparison of the oscillations in figure 2.4 shows that both systems act equal. Results for the frequency and also the amplitude are for both systems the same. The derived law for the torque is able to make a multi-body system behave like a single mass oscillator.

Multi-body system driven by a force

As seen before, the actuation of the knee with an ideal torque τ is simple. Looking at the real test-bed it is seen that the assumption of an ideal torque at the knee is not realistic. The torque at the knee is realized by a cable attached to a pulley with the radius r_p on the thigh. This can be compared to a force F attacking on a lever arm with the length r_p at the knee (see Fig. 2.5). The

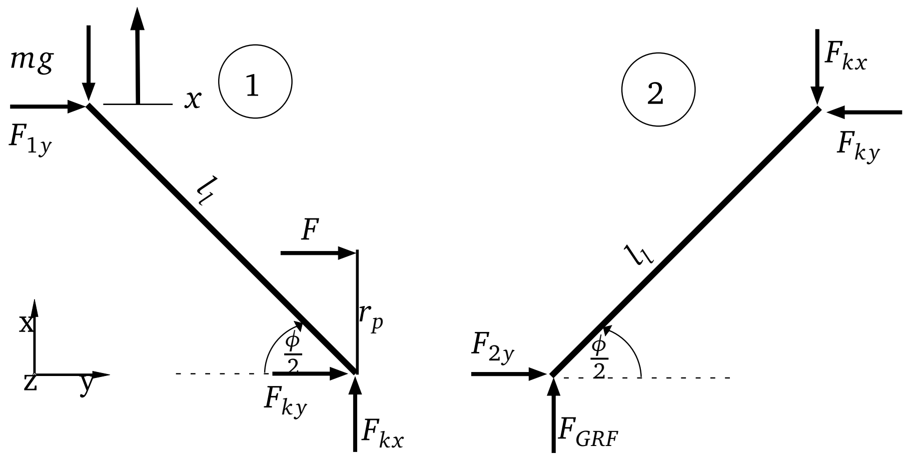

Figure 2.5.: Sketch of the multi-body system of two segments with the length l_l driven by a force F attacking on a lever arm with the length r_p. The lever arm is parallel to the rail/direction of x in the initial position. The system is divided in two parts through a cut at the knee and underneath the foot. Forces acting at the section planes are shown.

equations of equilibrium are developed similar to the system with the torque at the knee. After some transformations of the equations, the equation of motion for the top mass m follows:

$$m\ddot{x} = -\frac{1}{2}F\left(\cos\left(\frac{\phi}{2}-\arcsin\left(\frac{1}{2}\frac{x_0}{l_\mathrm{l}}\right)\right)\tan\left(\frac{\phi}{2}\right)-\sin\left(\frac{\phi}{2}-\arcsin\left(\frac{1}{2}\frac{x_0}{l_\mathrm{l}}\right)\right)-\frac{r_\mathrm{p}}{2\cos\left(\frac{\phi}{2}\right)l_\mathrm{l}}\right)-mg \tag{2.16}$$

The influence of the force F on the movement of the mass depends on ϕ in a form like:

$$\begin{aligned} m\ddot{x} &= -\frac{1}{2}Ff(\phi)-mg \\ f(\phi) &= \cos\left(\frac{\phi}{2}-\arcsin\left(\frac{1}{2}\frac{x_0}{l_\mathrm{l}}\right)\right)\tan\left(\frac{\phi}{2}\right)-\sin\left(\frac{\phi}{2}-\arcsin\left(\frac{1}{2}\frac{x_0}{l_\mathrm{l}}\right)\right)-\frac{r_\mathrm{p}}{2\cos\left(\frac{\phi}{2}\right)l_\mathrm{l}} \end{aligned} \tag{2.17}$$

To get the same result of the system acting like a single mass oscillator, the force must be computed in the following manner:

$$F = \frac{2k_\mathrm{v}(l_0-x)}{f(\phi)} \tag{2.18}$$

The comparison between this method and the single mass oscillator is shown in figure 2.6. The results are similar and comparable to the behavior gained by the calculation of the torque at the knee in Fig. 2.3.

A law for the force at the knee is more complicated and depends on the initial position of the force in the system. This shown relationships hold for the assumption that the lever arm of

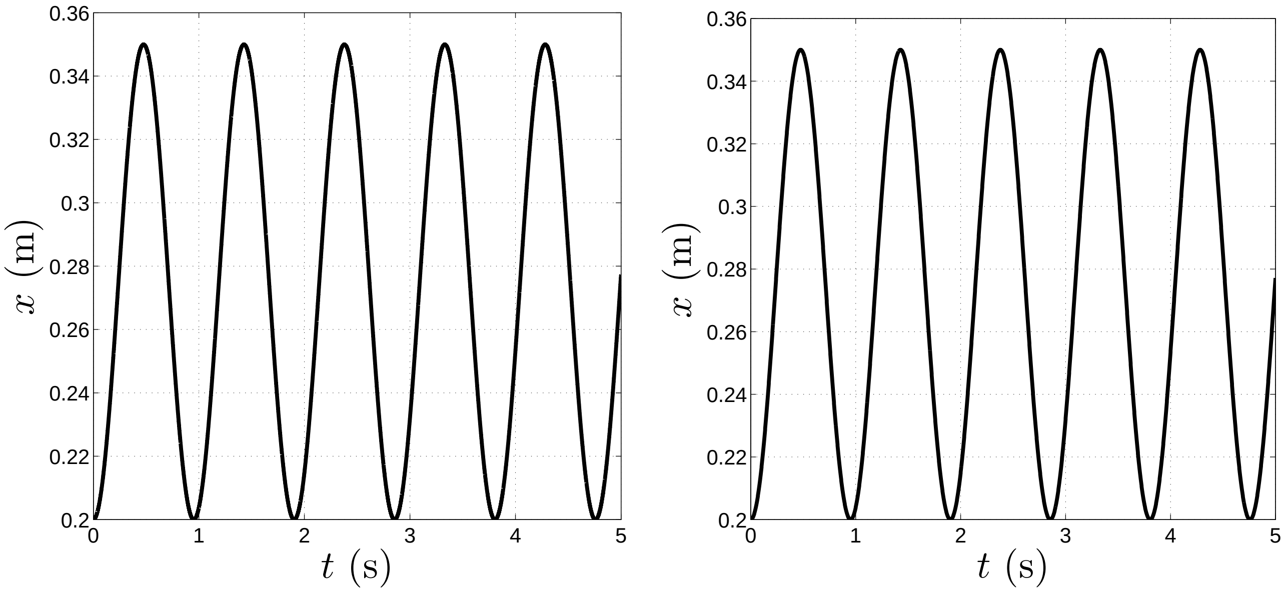

Figure 2.6.: [SIM] Comparison of the oscillation of the single mass oscillator and the multi-body system driven by a force F on a lever arm at the knee. The stiffness of the spring k_v is adjusted for a stable oscillation with the frequency $\omega = 7$ rad/s. The initial position of the mass is $x = 0.2$m and the rest length $l_0 = 0.5$m. The solver used for the single mass oscillator is ODE45 and for the multi-body system ODE23.

the force is parallel to the travel direction of the mass in the initial position of the system. All transformations introduced are valid for this initial condition. This condition is expressed through the term:

$$\phi_0 = \arcsin\left(\frac{1}{2}\frac{x_0}{l_1}\right) \tag{2.19}$$

Small deviations of the initial angular condition of the lever arm have a large impact on the movement of the structure, for the force calculation law to mimic single mass oscillator behavior bases on the initial condition. These angular deviation is introduced through adding $\Delta\beta$ in the initial condition of the system, but not in the equation of the force F (eq. 2.17). For the real initial position of the lever arm on the test-bed is not known, these deviations are likely when the law is implemented on the control of the test-bed. The new initial condition of the attacking force is now given by:

$$\phi_0 = \arcsin\left(\frac{1}{2}\frac{x_0}{l_1}\right) + \Delta\beta \tag{2.20}$$

The force generation law assumes a specific position of the lever arm for each position of the mass. The result of changing the real angular-position of the lever arm without adapting the force generation law is shown in figure 2.7.

Amplitude and frequency of the oscillation change even for small deviations. For it is not easy to adjust the force generation law to the initial lever arm position on the test-bed, the method for the force control presented in this paragraph, shall not be used. The calculation law for the torque shown in eq. 2.15 is much simpler and does not depend on the attacking point of the force. Therefore it is chosen as a valid generation law for the transformation of virtual spring force to knee torque for the following development of more complex systems.

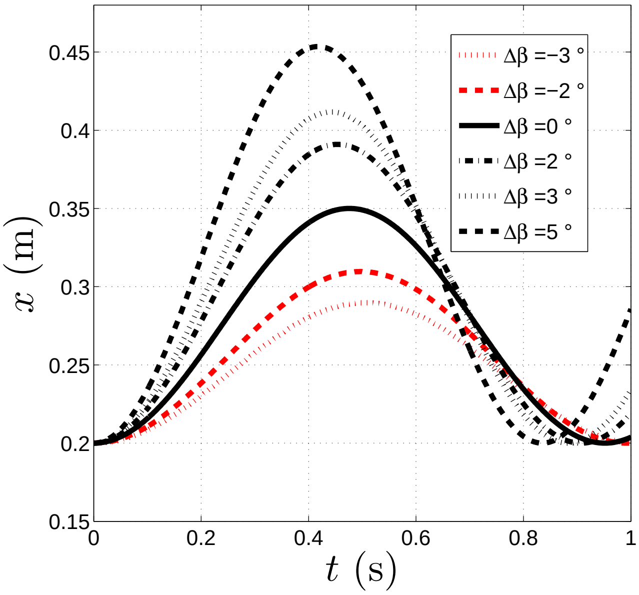

Figure 2.7.: [SIM] Oscillation of the top mass of an multi-body system with deviation of the initial angle of the lever arm $\Delta\beta$. The force generation law is not adapted, so a "'wrong"' force is effective for each position. The used solver is ODE23.

Summary multi-body system with one mass

The result from the examination of the single mass multi-body system is that it is possible to control the abstracted leg through a torque at the knee. The calculation law for the torque is simple and the implementation in the simulation shows comparable behavior of single mass oscillator and single mass multi-body system.

A control of a force attacking a lever arm attached to the thigh leads to more complicated laws with a dependency on initial conditions that react very sensitive to deviations. Although the assumption of a controlled force would be more realistic, the handling is far more prone to errors through imprecise assumptions of geometries.

2.1.4 Multi-body system with distributed masses

After the examination of multi-body systems with a single mass the influence of distributed masses on the multi-body system is debated. In Fig.2.8 the additional mass m_2 and inertia θ_l of the link are added to the system. θ_l is the moment of inertia of a segment of the leg relative to the hip bearing or the foot bearing and depends on the mass of a segment m_2 and the length l_l and width w_l of a segment.

$$\theta_l = \frac{1}{12} m_2 \left(l_l^2 + w_l^2\right) + m_2 \left(\frac{l_l}{2}\right)^2 \tag{2.21}$$

For the moments of inertia of the two links compensate each other in their influence on the movement of x, the calculation of those and the values are not of interest at this point. The

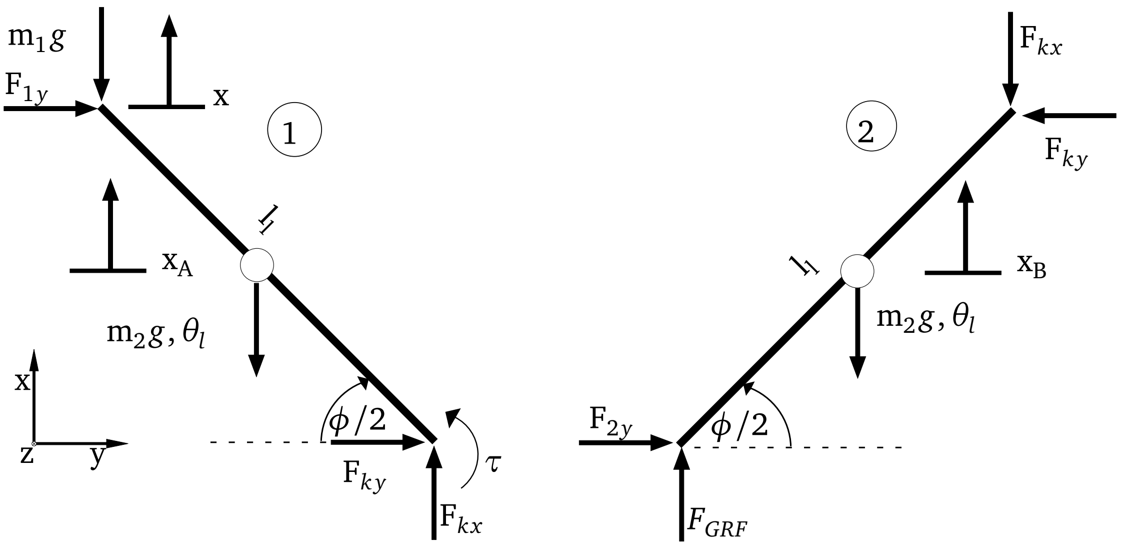

Figure 2.8.: Sketch of the multi-body system driven by an ideal torque τ. There are three masses in the system, the mass on top of the leg m_1 and the masses of each link m_2, which are considered as concentrated in the center of mass of each segment. Moments of mass inertia are calculated relative to the foot or the hip/ the end point of the segments. The structure got one degree of freedom x. The torque τ should act like a force by the virtual spring with the stiffness k_v. The system is divided in two parts through a cut at the knee and underneath the foot. Forces acting at the section planes are shown.

equations of equilibrium for this extended system are given by:

$$\begin{aligned}
\Sigma F_x^1 :& m_1\ddot{x} + m_2\ddot{x}_\mathrm{A} = F_\mathrm{kx} - (m_1 + m_2)g \\
& \textbf{with:} \\
& \ddot{x}_\mathrm{A} = \frac{3}{4}\ddot{\phi}\cos\left(\frac{\phi}{2}\right)l_1 - \frac{3}{8}\dot{\phi}^2\sin\left(\frac{\phi}{2}\right)l_1 = \frac{3}{4}\ddot{x} \\
& \left(m_1 + \frac{3}{4}m_2\right)\ddot{x} = F_\mathrm{kx} - (m_1 + m_2)g \\
\Sigma F_y^1 :& m_2\ddot{y}_\mathrm{A} = F_\mathrm{1y} + F_\mathrm{ky} \\
\Sigma M^1 :& \theta\ddot{\phi} = -F_\mathrm{ky}\sin\left(\frac{\phi}{2}\right)l_1 - F_\mathrm{kx}\cos\left(\frac{\phi}{2}\right)l_1 + m_2 g\cos\left(\frac{\phi}{2}\right)\frac{l_1}{2} + \tau \\
\Sigma F_x^2 :& m_2\ddot{x}_\mathrm{B} = -F_\mathrm{kx} + F_\mathrm{GRF} - m_2 g \\
& \textbf{with:} \\
& \ddot{x}_\mathrm{B} = \frac{1}{4}\ddot{\phi}\cos\left(\frac{\phi}{2}\right)l_1 - \frac{1}{8}\dot{\phi}^2\sin\left(\frac{\phi}{2}\right)l_1 = \frac{1}{4}\ddot{x} \\
& \frac{1}{4}m_2\ddot{x} = -F_\mathrm{kx} + F_\mathrm{GRF} - m_2 g \\
\Sigma F_y^2 :& m_2\ddot{y}_\mathrm{B} = -F_\mathrm{ky} + F_\mathrm{2y} \\
\Sigma M^2 :& \theta\ddot{\phi} = F_\mathrm{kx}\cos\left(\frac{\phi}{2}\right)l_\mathrm{link} - F_\mathrm{ky}\sin\left(\frac{\phi}{2}\right)l_1 + m_2 g\cos\left(\frac{\phi}{2}\right)\frac{l_1}{2}
\end{aligned} \tag{2.22}$$

This equations (Eq.2.22) lead to the expression:

$$\ddot{x} = \frac{\frac{\tau}{2\cos\left(\frac{\phi}{2}\right)l_1} - (m_1 + m_2)g}{m_1 + \frac{3}{4}m_2} \tag{2.23}$$

If the calculation law for τ from eq. 2.15 is used, the equation of motion for the described system is given by:

$$x = \left(x_0 - l_0 + \frac{m_1 + m_2}{\omega_{0,\mathrm{MB}}^2 \left(m_1 + \frac{3}{4}m_2\right)} g \right) \cos(\omega_{0,\mathrm{MB}} t) + l_0 - \frac{m_1 + m_2}{\omega_{0,\mathrm{MB}}^2 \left(m_1 + \frac{3}{4}m_2\right)} g$$

with:

$$\omega_{0,\mathrm{MB}} = \sqrt{\frac{k_{\mathrm{v}}}{m_1 + \frac{3}{4}m_2}} \tag{2.24}$$

It is assumed that the system with a change of mass relations could be controlled equally to the system with only a single mass on top of the structure (through the torque generation law in eq. 2.15). Changes to the motion resulting from the additional mass m_2 are described by the new eigen-frequency $\omega_{0,\mathrm{MB}}$.

Another way to show resulting differences is to compare the minimum frequency for reaching an apex point higher than the rest length. This frequency is now given by:

$$\omega_{0,\mathrm{MB}} > \sqrt{\frac{2(m_1 + m_2)g}{(l_0 - x_0)(m_1 + \frac{3}{4}m_2)}} \tag{2.25}$$

The frequency now depends on the distribution of masses between top mass m_1 and the distributed mass in one link m_2. Even for an equal sum of masses in the single mass multi-body system and the multi-body system with distributed masses $m_{1,\mathrm{SB}} = m_{1,\mathrm{MB}} + m_{2,\mathrm{MB}}$ the frequency which is needed to reach to reach a certain apex point is not the same. In Fig. 2.9 the different behavior can be seen. The frequency of the movement is slightly different. Also the movement near the apex point is different.

If the circumstance of the distribution of masses is ignored and the equation for finding the frequency for reaching the rest-length resulting from the single mass oscillator (eq. 2.9) is used, we get some differences in the behavior. The resulting oscillations are diagrammed in Fig. 2.10. The border frequency developed with the single mass oscillator is not able to reach the rest-length of the spring.

If a multi-body system should be driven by the laws derived from the analysis of a system with only one mass, to approach the behavior and simplify the calculations, some deviations occur. It is not possible to gain the exact same behavior. These errors result from the assumption that the calculation law for τ (see eq. 2.15) could be used without changes. If the exact behavior of the single mass oscillator ahould be gained, some changes have to be made to the calculation law of τ.

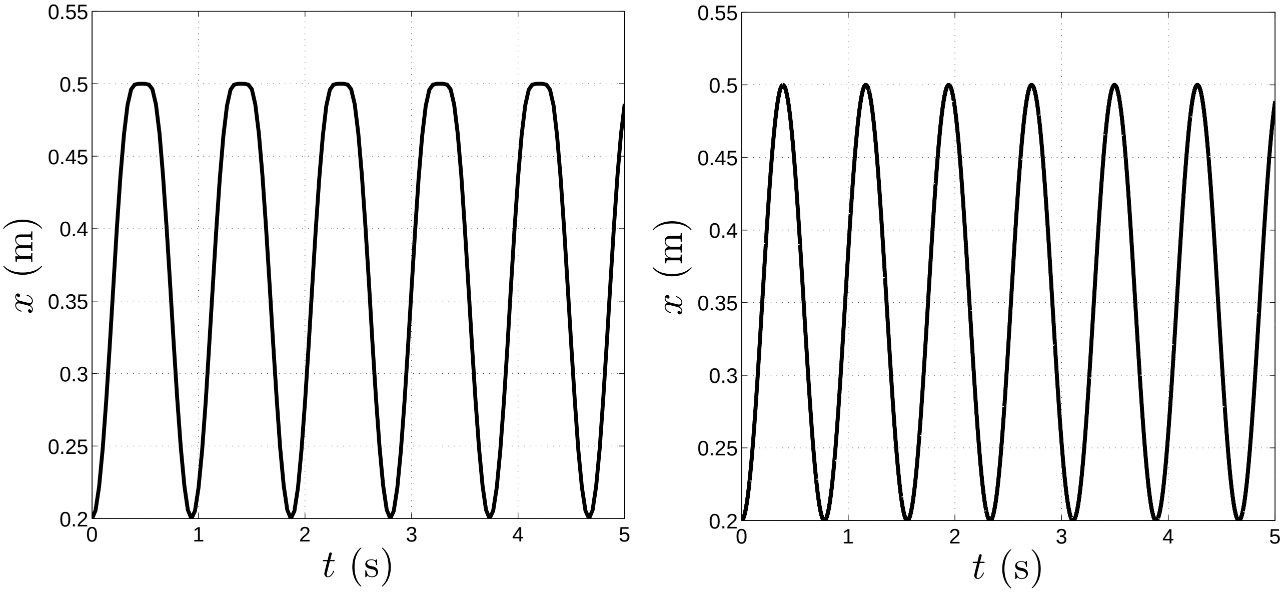

(a) **(b)**

Figure 2.9.: [SIM] Comparison of the oscillation of the single mass oscillator (b) and a multi-body system (a). The stiffness of the spring k_{v} is adjusted for reaching the rest length of the spring of both systems. Both systems have the exact same sum of mass, but a different distribution of masses. The initial position of the top point is $x = 0.2$m and the rest length $l_0 = 0.5$m. The solver used for the single mass oscillator is ODE45 and for the multi-body system ODE23.

SLIP like behavior of the multi-body system

If a similar behavior of the multi-body system and the single mass oscillator should be gained, the condition that eq. 2.1 is equal to eq. 2.23 has to be met. The masses of the systems are given by m_1(mass on the top of the multi-body system), m_2(mass of one link) and m(mass in the single mass oscillator).

A relationship between the torque in the multi-body system τ, the spring rate k_{v} of the single mass oscillator, all the masses of both systems and the kinematics of the multi-body system can be found, to make the multi-body system move like a single mass oscillator with fixed parameters.

$$\begin{aligned} \tau &= \left(\frac{k_{\text{v}}(l_0 - x) - mg}{m} (m_1 + \frac{3}{4} m_2) + (m_1 + m_2) g \right) 2 \cos\left(\frac{\phi}{2}\right) l_1 \\ \textbf{in:} & \\ \ddot{x} &= \frac{\frac{\tau}{2\cos\left(\frac{\phi}{2}\right) l_1} - (m_1 + m_2) g}{m_1 + \frac{3}{4} m_2} \end{aligned} \tag{2.26}$$

A single mass oscillator with a desired behavior (like an apex height or a certain frequency of movement) can be chosen, defined through its mass m, rest length l_0 and its spring-rate k_{v}. The same behavior can be mimicked with a multi-body system with the given values for the masses and the kinematics.

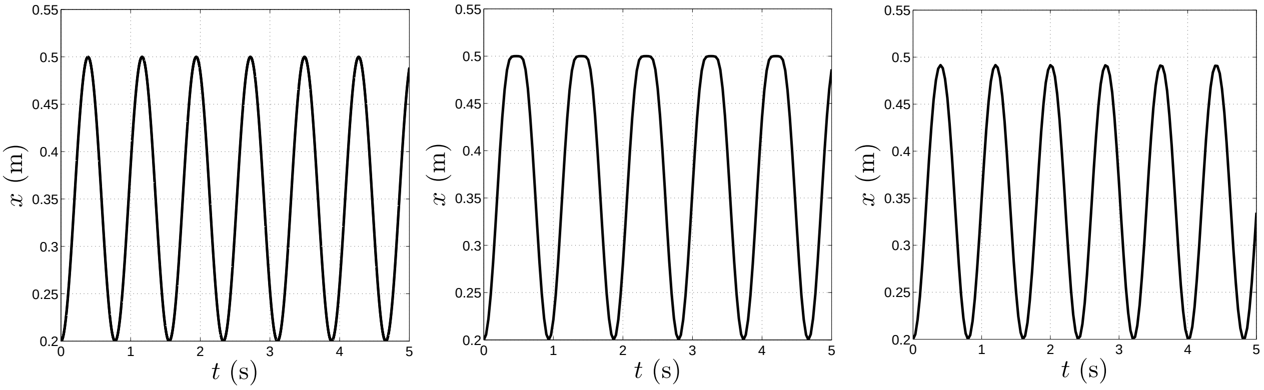

(a) **(b)** **(c)**

Figure 2.10.: [SIM] Comparison of the oscillation of the single mass oscillator (a) and two different multi-body system settings (b+c). The stiffness of the spring k_v is adjusted for reaching the rest length of the spring. In the system (c) the same k_v as in (a) is used. All systems have exact the same sum of mass, but a different distribution of masses. The initial position of the top point is $x = 0.2$m and the rest length $l_0 = 0.5$m. The solver used for the single mass oscillator is ODE45 and for the multibodysystem ODE23.

As shown in Fig.2.11 the oscillations of both systems are exactly the same. The force pattern has the same frequency, but the amplitude of the single-mass system is higher. This circumstance is easily explainable by the chosen parameters of the simulations. The multi-body system was set to the real values of masses of the test bed $m_1 = 0.498$ kg and $m_2 = 0.135$ kg. Whereas, for the single mass oscillator a mass of $m_3 = 1$kg was chosen. The theoretical ground reaction force for the multi-body system is given by:

$$\begin{aligned}
F_{\mathrm{GRF}} =& m_2\ddot{x}_{\mathrm{B}} + F_{\mathrm{kx}} + m_2 g \\
=& m_2\ddot{x}_{\mathrm{B}} + \frac{\tau}{2\cos\left(\frac{\phi}{2}\right) l_1} + m_2 g \\
=& \frac{1}{4} m_2 \ddot{x} + \frac{\tau}{2\cos\left(\frac{\phi}{2}\right) l_1} + m_2 g \\
=& \frac{k(l_0 - x) - mg}{m}(m_1 + m_2) + (m_1 + 2m_2) g \\
\textbf{with: } k =& \omega_{\mathrm{des}}^2 m \\
F_{\mathrm{GRF}} =& \omega_{\mathrm{des}}^2 (m_1 + m_2)(l_0 - x) + m_2 g
\end{aligned} \tag{2.27}$$

To compare the ground reaction force of the multi-body system F_{GRF} with the one of the single mass oscillator $F_{\mathrm{GRF,SM}}$ we derive:

$$\begin{aligned}
F_{\mathrm{GRF,SM}} =& k(l_0 - x) \\
\textbf{with: } k =& \omega_{\mathrm{des}}^2 m \\
F_{\mathrm{GRF,SM}} =& \omega_{\mathrm{des}}^2 m (l_0 - x)
\end{aligned} \tag{2.28}$$

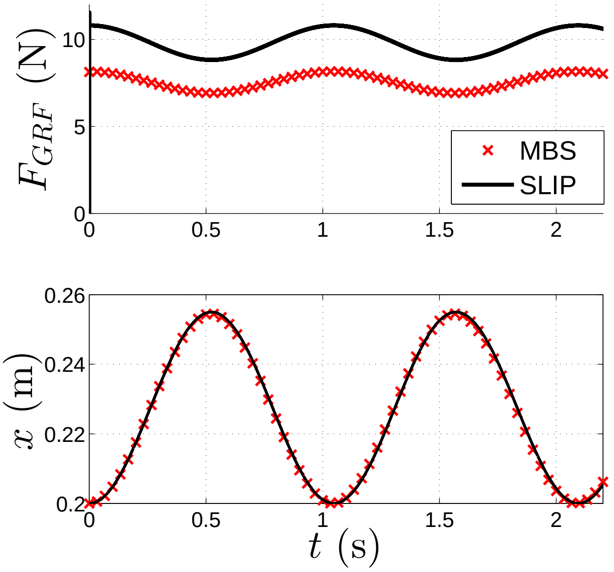

Figure 2.11.: [SIM] Motion- and force-patterns derived from a single mass oscillator model (SLIP) and a multibody-system model (MBS) with distributed masses. The oscillation of the top point is the same for both models. Force patterns of the ground reaction force are different, for the sum of masses in the systems are different. $m = 1$ kg while $m_1 = 0.498$ kg and $m_2 = 0.135$ kg. The solver used for the single mass oscillator model is ODE45 and for the multi-body system ODE23.

In Fig. 2.12 the trend of both forces in dependency of the position of the top point x is compared. As we see in eq. 2.28 and eq. 2.27 the slopes of both force functions are different. Also the offset-points are different. The ground reaction force of the single mass oscillator will become zero for a position of x equal to the rest length of the spring. The spring does not transfer forces if it is unstressed. In the multi-body system the weight-force of one segment causes the offset. Both position-force-relations are linear. A multi-body system can be controlled with a linear force-law to behave like a single mass oscillator.

Non-linear behavior of the multi-body system with attached cable

The leg will be attached to the drive-train with a cable. For the cable is modeled as a spring with the stiffness k_c, the cable and the segmented leg form a system able to perform oscillations. The system can be considered as a kind of mass-spring system with a corresponding eigen-frequency. Resonance and related effects can occur, but also be used to enhance the performance of the system.

For determining this effects, the eigen-frequency has to be calculated. The system shown in Fig. 2.8 is used. The driving torque τ is replaced by a force F resulting from the displacement of the cable/spring when it is loaded with the weight of the segmented leg. So the system is comparable to a mass resting on a spring. The equations to describe the eigen-frequency are given by:

$$\left(m_1 + \frac{3}{4}m_2\right)\ddot{x} = \frac{\tau}{2\cos\left(\frac{\phi}{2}\right)l_1} - (m_1 + m_2)g \tag{2.29}$$

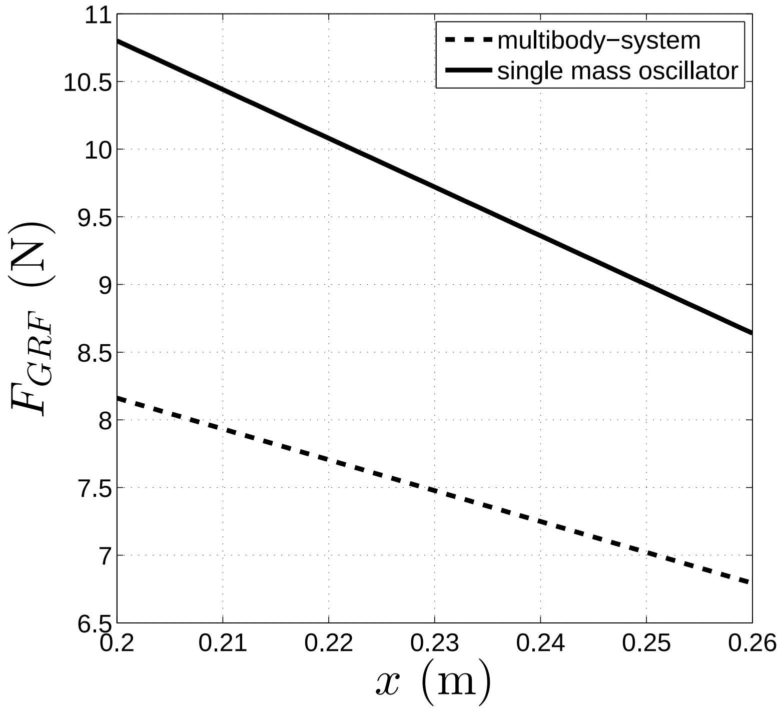

Figure 2.12.: [SIM] Relation between the position of the top point x and the ground reaction forces F_{GRF} for the multi-body system and $F_{\mathrm{GRF,SM}}$ for the single mass oscillator. Both systems are tuned to have the same oscillation pattern (shown in Fig. 2.11. Both courses of the force are linear but have different slopes and offsets. The solver used for the single mass oscillator is ODE45 and for the multi-body system ODE23.

The torque τ can be described by a force attacking on the pulley with the lever arm r_{p}. Force transformations through the cable are exposed to losses. This is described by the efficiency of the cable η_{c}.

$$\tau = F r_{\mathrm{p}} \eta_c \tag{2.30}$$

The force and therefore the torque depends on the deflection of the cable. It can be expressed with the initial angular position ϕ_0 and the current angular position ϕ at the knee.

$$\begin{aligned} F &= k_{\mathrm{c}}(\phi_0 r_{\mathrm{p}} - \phi r_{\mathrm{p}}) \\ \tau &= k_{\mathrm{c}} r_{\mathrm{p}}^2 \eta_c (\phi_0 - \phi) \end{aligned} \tag{2.31}$$

The dependencies of the angle ϕ can be transformed to dependencies of the position x. Through the constant C_1 the initial condition of the system is expressed.

$$\begin{aligned} \sin\left(\frac{\phi_0}{2}\right) &= \frac{x_0}{2l_1} \\ \phi_0 &= 2\arcsin\left(\frac{x_0}{2l_1}\right) = 2C_1 \\ \phi &= 2\arcsin\left(\frac{x}{2l_1}\right) \end{aligned} \tag{2.32}$$

The following transformations serve to implement the relationships in the equation of motion.

$$
\begin{aligned}
F &= 2k_{\mathrm{c}}r_{\mathrm{p}}\left(\arcsin\left(\frac{x_0}{2l_1}\right)-\arcsin\left(\frac{x}{2l_1}\right)\right)\\
2l_1\cos\left(\arcsin\left(\frac{x}{2l_1}\right)\right) &= \sqrt{4l_1^2-x^2}
\end{aligned}
\tag{2.33}
$$

Now the differential equation of motion for the "mass"-spring system is given by:

$$
\ddot{x}-\frac{2k_{\mathrm{c}}r_{\mathrm{p}}^2\eta_c(C_1-\arcsin(\frac{x}{2l_1}))}{\sqrt{4l_1^2-x^2}(m_1+\frac{3}{4}m_2)}=-\frac{m_1+m_2}{m_1+\frac{3}{4}m_2}g
\tag{2.34}
$$

To find a description of the eigen-frequency of the system, the part dependent of x has to be analyzed.

$$
f(x)=\frac{2k_{\mathrm{c}}r_{\mathrm{p}}^2\eta_c(C_1-\arcsin(\frac{x}{2l_1}))}{\sqrt{4l_1^2-x^2}(m_1+\frac{3}{4}m_2)}
\tag{2.35}
$$

A splitting of the relationship in the form of a single mass oscillator to get the eigen-frequency of the system does not seem possible. The simulation of the system leads to the following results. Shown are the resulting oscillations with different initial conditions in Fig. 2.13. The frequency of oscillation for a single mass oscillator is independent of the initial condition. For the segmented leg the eigen-frequency is dependent of the initial condition.

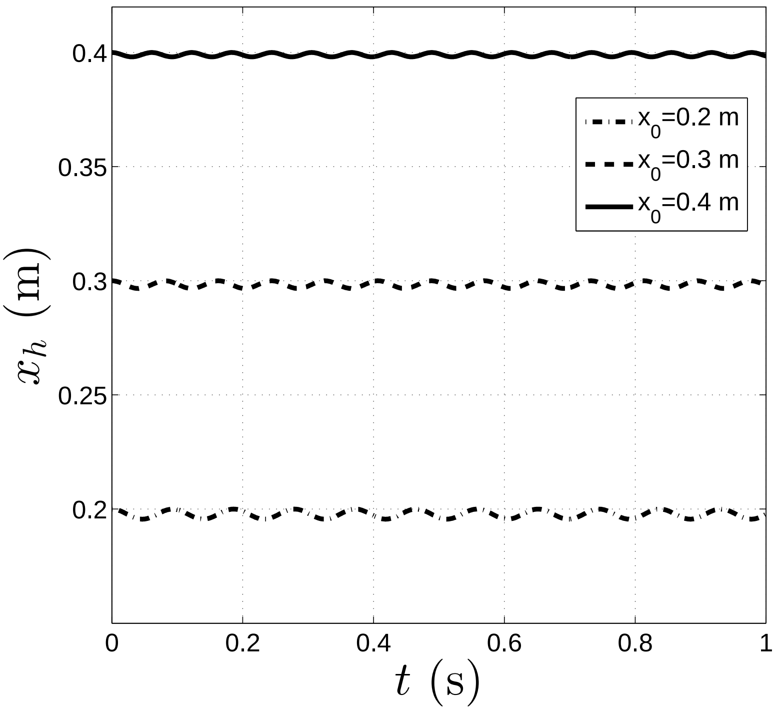

Figure 2.13.: [SIM] The oscillation of the hip position x_{h} of the segmented leg with different initial positions. The cable of the knee is attached to a rigid point.

We assume that the eigen-frequency is fixed for a certain initial condition C_1. Therfore, the eigen-frequency could be determined in the following manner.

$$\begin{aligned}f(x) &= \frac{2k_\mathrm{c} r_\mathrm{p}^2 \eta_c (C_1 - \arcsin(\frac{x}{2l_1}))}{\sqrt{4l_1^2 - x^2}(m_1 + \frac{3}{4}m_2)} = \omega_0^2 x \\ \omega_0 &= \sqrt{\frac{f(x)}{x}} = \sqrt{\frac{2k_\mathrm{c} r_\mathrm{p}^2 \eta_c (C_1 - \arcsin(\frac{x}{2l_1}))}{\sqrt{4l_1^2 - x^2}(m_1 + \frac{3}{4}m_2)x}}\end{aligned} \tag{2.36}$$

This relationship would be valid if the eigen-frequency of the system is independent of the position x.

These findings could be used to develop a serial elastic actuation concept to influence the behavior and energy consumption in the manner of the way presented by *Vu* et al in [31] (see chapter 1.3.3). Because it is not a core task of this work, the idea will not be pursued further.

Summary multi-body system with distributed masses

It has been shown that a multi-body system with distributed masses can be controlled in the fashion of a single mass oscillator while the foot does not leave the ground. Some laws for the generation of the torque at the knee had to be adjusted. The use of the simple laws derived for the single mass oscillator and the segmented structure with one mass lead to errors in the behavior. A possible approach to determine the eigen-frequency region of the system has been shown.

2.2 Dynamic equations of models with ascending complexity - hopping

So far all models were used to show relations while the foot stays on the ground. A hopping motion includes also a flight phase and a landing. These events make the models unsteady for some forces only act during certain time segments of the whole movement.

For example influences the ground model the system only while the leg is on the ground. On the other hand, the movement of the foot mass during the phase of ground contact is near to zero. Forces resulting from this movement are very small. In the moment of take-off the foot mass moves in comparable range to the mass at the hip. Resulting forces from the foot movement only influence the system behavior during the flight phase.

Models will be presented that are able to describe these flight phases and the change of effects between ground contact phase and flight phase. All models will be derived with an ascending complexity again.

2.2.1 Harmonic oscillator

The harmonic oscillator is extended with a foot point that enables the system to leave the ground, therefore it possesses now two degrees of freedom x and x_f (see fig.2.14).

Relevant parameters are the mass on top m, the mass of the foot m_4 and the spring with it's rest length l_0 and spring rate k. The ground exerts forces on the foot mass and is modeled through a spring and damper in parallel with the spring rate k_g and the damping parameter d_g. Ground forces only occur when the displacement of the ground Δx_g becomes bigger than zero. This displacement is equal to a foot position underneath zero. The forces by the ground are always bigger than zero. There will be more explained about the ground models in chapter 3.2.4.

The equations of motion are given by:

$$\begin{aligned} m\ddot{x} &= k(l_0 - x + x_\mathrm{f}) - mg \\ m_4\ddot{x}_\mathrm{f} &= -k(l_0 - x + x_\mathrm{f}) + k_\mathrm{g}(\Delta x_\mathrm{g}) - d_\mathrm{g}\dot{x}_\mathrm{f} - m_4 g \end{aligned} \tag{2.37}$$

The differential equations during the flight phase are given by:

$$\begin{aligned} m\ddot{x} &= k(l_0 - x + x_\mathrm{f}) - mg \\ m_4\ddot{x}_\mathrm{f} &= -k(l_0 - x + x_\mathrm{f}) - m_4 g \end{aligned} \tag{2.38}$$

The second mass m_4 representing the foot point is set to a value near to zero to gain a behavior that comes close to a single mass oscillator. Values for k and ω_0, which are needed to reach certain states of movement during ground contact, have been discussed before (see chapter 2.1.1). Now the range of parameters for reaching a certain hopping height is examined.

It has been shown (see chapter 2.1.2) that the change of height Δh after reaching the rest length of the spring l_0 (equal to the hopping height) depends on the velocity of the top mass $\dot{x}_\mathrm{TO}$ at the moment when it reaches the rest length of the spring ('take-off', the foot-point leaves the ground, for the force by the spring is zero):

$$\Delta h = \frac{1}{2g}\dot{x}_\mathrm{TO}^2 \tag{2.39}$$

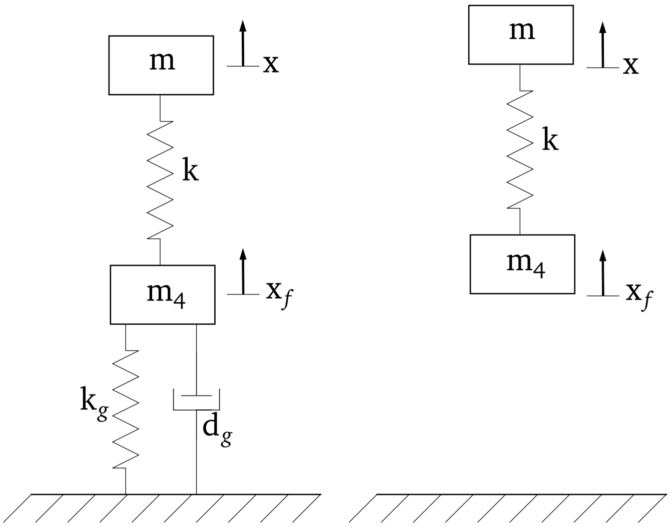

Figure 2.14.: Sketch of the model for the harmonic oscillator. The structure got two degrees of freedom x and x_{f}. A spring with the rate k attached between the hip mass m and the foot mass m_4 drives the oscillation. The ground consists of parallel spring with the rate k_{g} and a spring with the rate d_{g}. The ground forces effect the oscillator only during the stance phase.

The velocity at 'take-off' $\dot{x}_{\mathrm{TO}}$ for a certain rest length l_0, an initial position x_0 of the mass m and a desired eigen-frequency ω_{des} is given by:

$$\dot{x}_{\mathrm{TO}}^2 = \omega_{\mathrm{des}}^2 (x_0 - l_0)^2 + 2g(x_0 - l_0) \tag{2.40}$$

So the change of height Δh after the take-off can be determined by:

$$\Delta h = \left(\frac{\omega_{\mathrm{des}}^2}{2g} (x_0 - l_0)^2 + (x_0 - l_0) \right) \frac{m}{m + m_4} \tag{2.41}$$

The relation of the masses m and m_4 influences the hopping height. The ideal height could be reached for a foot mass near zero . A realistic relation for the masses (see Fig. 3.1 with the distribution of the masses on the test-bed) leads to a reduced hopping height of approximately $\Delta h_{\mathrm{red}} = 0.8 \Delta h(m_4 = 0)$.

A spring rate k can be found that leads to a certain hopping height $x_{\max} = l_0 + \Delta h$ of the harmonic oscillator:

$$k = 2gm \frac{\Delta h \frac{m + m_4}{m} - x_0 + l_0}{(x_0 - l_0)^2} \tag{2.42}$$

This relationship can be used as a first approach to generate a desired hopping height and to compare results of the simulation and the experiment performed with this value.

2.2.2 Multi-body system with distributed masses

This model contains all masses that can be found on the real test-bed and takes them into account (see fig.2.15). The system has two degrees of freedom, the position of the hip x_h and the position of the foot x_f. All other positions (x_A, x_B the positions of the center of mass of the two links; x_K the knee position) and the angle between the segments and the direction of x, ψ and the knee angle ϕ are dependent values.

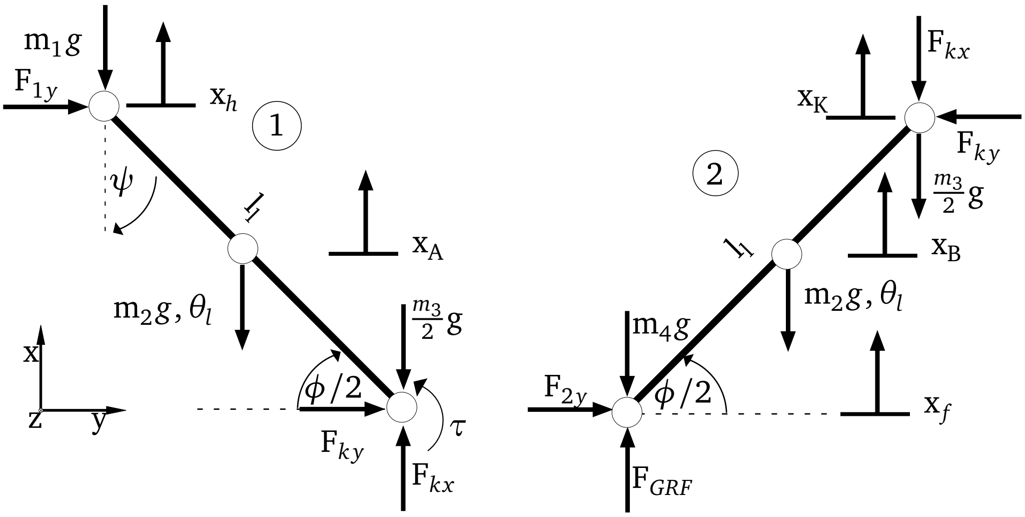

Figure 2.15.: Free body diagram of the multi-body system with all involved forces and torques. (1) represents the upper link (thigh) and (2) the lower link (shank) of the leg. m_1 represents the mass on the top point, m_2 is the mass of a link, m_3 is the additional mass at the knee point and m_4 represents the mass of the foot. All masses produce gravitational and inertial forces. Additionally the mass moments of inertia (related to hip/foot point) of the links presented by θ_l take effect. All forces (F_1y,F_ky,F_kx,F_2y,F_GRF) result from contact forces of the bearings. The torque τ actuates the system. Positions of the masses are given by x_h, x_A, x_K, x_B and x_f. The knee angle is represented by ϕ.

The equations of motion for the system are given by:

Part ①:

$$\begin{aligned}
\Sigma F_x^1 &: m_1\ddot{x}_\mathrm{h} + m_2\ddot{x}_\mathrm{A} + \frac{m_3}{2}\ddot{x}_\mathrm{K} = F_\mathrm{kx} - \left(m_1 + m_2 + \frac{m_3}{2}\right) g \\
&\left(m_1 + \frac{3}{4}m_2 + \frac{1}{4}m_3\right)\ddot{x}_\mathrm{h} = F_\mathrm{kx} - \left(m_1 + m_2 + \frac{m_3}{2}\right) g \\
\Sigma F_y^1 &: m_2\ddot{y}_\mathrm{A} + \frac{m_3}{2}\ddot{y}_\mathrm{K} = F_\mathrm{1y} + F_\mathrm{ky} \\
\Sigma M^1 &: \theta_l\ddot{\psi} + \frac{m_3}{2} l_l^2\ddot{\psi} = -F_\mathrm{ky}\sin\left(\frac{\phi}{2}\right) l_l - F_\mathrm{kx}\cos\left(\frac{\phi}{2}\right) l_l \\
&+ m_2 g\cos(\frac{\phi}{2})\frac{l_l}{2} + \tau + \frac{m_3}{2} g\cos\left(\frac{\phi}{2}\right) l_l
\end{aligned} \tag{2.43}$$

Part ②:

$$\begin{aligned}
\Sigma F_x^2 :& m_2\ddot{x}_\mathrm{B} + m_4\ddot{x}_\mathrm{f} + \frac{m_3}{2}\ddot{x}_\mathrm{K} = -F_\mathrm{kx} + F_\mathrm{2x} - \left(m_2 + \frac{m_3}{2} + m_4\right) g \\
& m_4\ddot{x}_\mathrm{f} + \left(\frac{m_2}{4} + \frac{m_3}{4}\right)\ddot{x}_\mathrm{h} = -F_\mathrm{kx} + F_\mathrm{2x} - \left(m_2 + \frac{m_3}{2} + m_4\right) g \\
\Sigma F_y^2 :& m_2\ddot{y}_\mathrm{B} + \frac{m_3}{2}\ddot{y}_\mathrm{K} = -F_\mathrm{ky} + F_\mathrm{2y} \\
\Sigma M^2 :& \theta_\mathrm{l}\ddot{\psi} + \frac{m_3}{2} l_\mathrm{l}^2 \ddot{\psi} = -F_\mathrm{ky}\sin\left(\frac{\phi}{2}\right) l_\mathrm{l} + F_\mathrm{kx}\cos\left(\frac{\phi}{2}\right) l_\mathrm{l} \\
& + m_2 g\cos\left(\frac{\phi}{2}\right) l_\mathrm{l}/2 + \frac{m_3}{2} g\cos(\frac{\phi}{2} l_\mathrm{l} \\
\text{with:}& \\
& \ddot{x}_\mathrm{A} = \frac{3}{4}\ddot{x}_\mathrm{h}, \ddot{x}_\mathrm{B} = \frac{1}{4}\ddot{x}_\mathrm{h}, \ddot{x}_\mathrm{K} = \frac{2}{4}\ddot{x}_\mathrm{h}
\end{aligned} \tag{2.44}$$

Transformations of the equations lead to:

$$\begin{aligned}
\ddot{x}_\mathrm{h} =& \frac{1}{m_1 + \frac{3}{4}m_2 + \frac{1}{4}m_3}\left(\frac{\tau}{2\cos\left(\frac{\phi}{2}\right) l_\mathrm{l}} - \left[m_1 + m_2 + \frac{m_3}{2}\right] g\right) \\
\ddot{x}_\mathrm{f} =& \frac{1}{m_4}\Bigg(-\frac{\tau}{2\cos\left(\frac{\phi}{2}\right) l_\mathrm{l}} + F_\mathrm{2x} - \left[m_2 + \frac{m_3}{2} + m_4\right] g \\
& - \frac{m_3 + m_2}{4\left(m_1 + \frac{3}{4}m_2 + \frac{m_3}{2}\right)}\left[\frac{\tau}{2\cos\left(\frac{\phi}{2}\right) l_\mathrm{l}} - \left(m_1 + m_2 + \frac{m_3}{2}\right) g\right]\Bigg)
\end{aligned} \tag{2.45}$$

The differential equations for the movement of x_h and x_f can be used to simulate the behavior of a multi-body system. To accomplish the goal of a movement of the multi-body system similar to a single mass oscillator with flight phase, the following equation for a single mass oscillator with two degrees of freedom (position of the mass on top x_SM and the position of the foot $x_\mathrm{f,\,SM}$) and the equation for $\ddot{x}_\mathrm{h}$ have to be equal:

$$\ddot{x}_\mathrm{SM} = \frac{k(l_0 - x_\mathrm{SM} + x_\mathrm{f,\,SM}) - mg}{m} \tag{2.46}$$

The condition $\ddot{x}_1 = \ddot{x}_\mathrm{SM}$ leads to a calculation term for τ:

$$\tau = 2\cos\left(\frac{\phi}{2}\right) l_\mathrm{l}\left(\frac{k_\mathrm{v}(l_0 - x_\mathrm{h} + x_\mathrm{f}) - mg}{m}\left(m_1 + \frac{3}{4}m_2 + \frac{1}{4}m_3\right) + \left(m_1 + m_2 + \frac{m_3}{2}\right) g\right) \tag{2.47}$$

If the system is influenced by a torque generated by this law, a movement similar to a single mass oscillator is possible. The generation law is only valid during the contact with the ground. The mass of the foot m_4 is not moved during this time. After the 'take-off' of the leg the dynamic of the system is also influenced by this additional mass.

In eq. 2.42 a law for determining a certain stiffness k_v of the virtual spring for reaching a desired hopping height is shown.

$$k_\mathrm{v} = 2gm_1 \frac{\Delta h \frac{m_1+2m_2+m_3+m_4}{m_1} - x_0 + l_0}{(x_0 - l_0)^2} \tag{2.48}$$

In this equation we assume that only the mass at the hip m_1 possesses kinetic energy when the rest length is reached. The masses $m_2 - m_4$ have to be accelerated by this available energy. When the potential energy of all masses and the kinetic energy of m_1 during 'take-off' are equal, the apex point of the movement is reached.

Eq. 2.48 sets a lower limit of the hopping height, for m_2 and m_3 also posses kinetic energy before the foot leaves the ground. In reality there are also friction forces acting against the hopping motion. Therefore, the reached hopping height will always be lower than the one anticipated with the presented equations. The purpose is to estimate values for tuning the model and the test-bed that will result in hopping motions. Energy losses that occur during the motion have to be compensated with other methods presented in the control section of this thesis.

3 Test-bed Marco Hopper II

The derived theories have to be tested on a realistic device. Therefore, a mechanic segmented leg has been developed. The drive-train of the structure holds the possibility of testing different concepts of actuation.

3.1 Configuration of MARCO Hopper II and changes

As described in paragraph 1.3.2 the test-bed has already been developed and built [9]. During the development of proper control strategies some adaptions had to be made. This chapter sums up these changes and the properties of MARCO II.

MARCO II consists of two main parts. One part represents the leg and the body on top of it. For the purpose of coming close to the mass proportions of the leg it represents, the masses (m_1-mass at the hip and m_4-mass at the foot) are scalable. The other part is the drive-train which provides the necessary forces to move the leg. Both parts are connected with a cable attached to the knee of the leg and the output of the drive-train.

3.1.1 Segmented leg of MARCO II

The segmented leg consists of different parts with different tasks (see Fig. 3.1). All properties are summed up in Fig. 3.1. The values give the current status of each part of the system. Further changes are mentioned when they are made.

First there are the structural parts of the leg, the segments (representing shank and thigh with length l_l, width w_l, height h_l, density of aluminum ρ_al), the roller- and linear-bearings (representing hip-, knee- and ankle-joint), the pulley at the knee (effective radius r_p), the stop of the knee preventing it from over-extension (allowing a maximum knee angle of ϕ_max) and the mass m_1 that can be added to the upper linear bearing. The masses m_2 (leg segment mass), m_3 (mass at the knee) and m_4 (mass at the foot) are fixed in this setting.

There are three sensors at the leg. The positions of hip x_h, foot x_f and the knee angle ϕ are measured by a potentiometer position sensor and via an inertial measurement unit (IMU). The third sensor is a strain gauge force sensor measuring the ground reaction force F_GRF beneath the foot. The IMU and also the force sensors were not part of the original concept and have been added in the process of this work.

Changes to the segmented leg during the development

There are a few changes made to the leg during the process of this thesis. The changes are shown in Fig. 3.1. First the concept of torque generation at the knee was changed. In the original setup

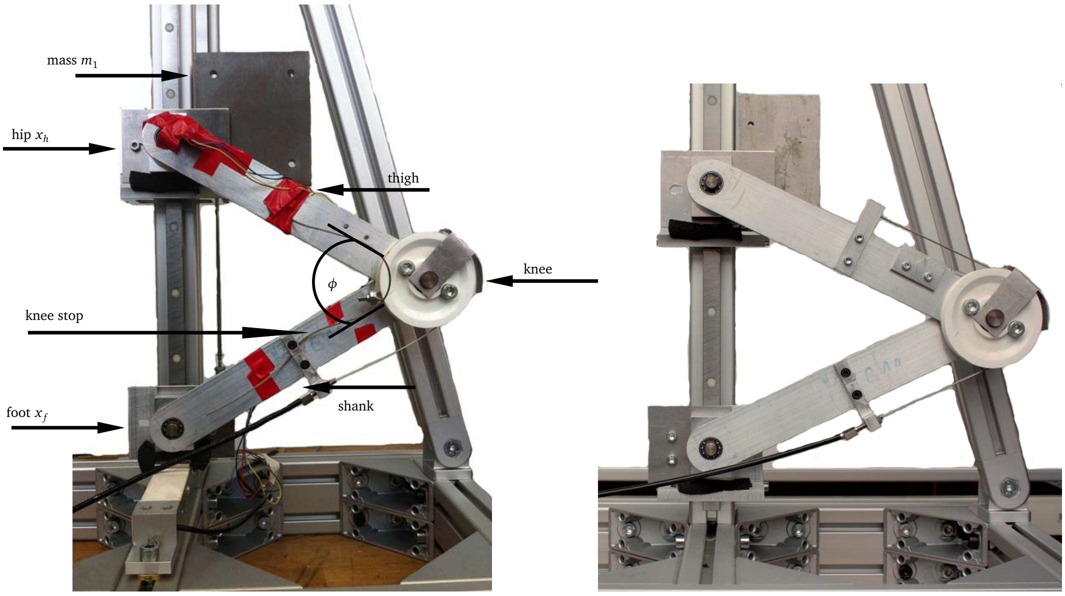

(a) (b)

Figure 3.1.: The segmented leg of MARCO Hopper II. (a) shows the leg in the current state. (b) shows it in the beginning of the thesis. The two segments thigh and shank got a length of l_l with a knee angle ϕ enclosed between them. Thigh and shank are connected by a roller bearing at the knee. The pulley is fixed on the shank with the cable glued on it. Positions of hip and foot are given by x_h and x_f. The foot and the hip are connected to the vertical sledge via linear bearings and to the segments via roller bearings. Also an additional mass m_1 could be added at the hip. The knee stop is realized via a cable, limiting the knee angle. Underneath the foot a force sensor is mounted measuring the ground reaction force F_GRF. The potentiometer position sensor is fixed to the foot. On the hip, near the joint, the IMU is mounted.

the cable was fixed on the thigh. Therefore no torque could be generated at the knee. The force moving the leg was a horizontal force generated by the shortening of the cable. Fixing the cable on the pulley generates a torque at the knee/ at the lower part of the thigh. The mass at the hip m_1 was changed. In the old configuration the mass of $m_1 = 0.498$ kg generated not enough inertia to let the whole leg jump. Also the sensors to measure the knee angle ϕ, the foot position x_f and the ground reaction force F_GRF were added.

3.1.2 Drive-train of Marco Hopper II

The drive-train consists of the parts motor, motor encoder, transmission, ball screw, carriages and the force sensor. The properties of each part can be found in chapter 3.2.3.

In the original concept a spring was included in the drive train to investigate the behavior and energy consumption of a system under the influence of a drive-train with SEA. The current setup of the drive-train uses a force sensor in the place of the spring. A picture of the drive-train is shown in fig. 3.2.

Table 3.1.: Properties of the segmented leg

properties segmented leg	
length of leg segment	$l_l = 0.25$ m
width of leg segment	$w_l = 0.005$ m
height of leg segment	$h_l = 0.04$ m
effective radius pulley	$r_p = 0.034$ m
maxiumum knee angle	$\phi_{max} = 120°$
current mass at the hip	$m_1 = 1.102$ kg
mass of one segment	$m_2 = 0.135$ kg
current mass at the knee	$m_3 = 0.3$ kg
current mass at the foot	$m_4 = 0.297$ kg
density of aluminum	$\rho_{al} = 2700$ kg m^{-3}
roller bearings	SKF No. 61800
linear bearings	item Industrietechnik GmbH, PS 4-15
pulley at the knee	Burckhardt, No. C178 002 560/80
potentiometer position sensor	Burster Präzisionsmesstechnik, No. 8709-5150
IMU	MPU6050 3-axis acceleration sensor + gyro - 6DOF module [4]
force sensor - load cell	Watterott electronic, 0-30 kg [3]

The current of the motor is managed with a motor controller from MAXON. An internal PI current controller sets the desired current to the motor. The internal control of current tends to oscillations due to high steps in the desired values during a hopping motion. Some problems resulting from this will be discussed in chapter 5.2.1.

An embedded controller for managing sensor and control signals is given by the NATIONAL INSTRUMENTS *MyRIO*. It receives all signals of the test-bed and handles all information together with a PC-workstation. The software used to control the test-bed is NATIONAL INSTRUMENTS LABVIEW. The test-bed is supplied with energy through two power sources. One supplies the motor and the control devices connected to it. The other power source supplies all the sensors and necessary signal amplifiers.

Changes to the drive-train during the development

The changes of the drive-train were limited to the development of some adapter pieces to include the force sensor in the drive-train and a device to pre-load the force sensor.

For the changes are concentrated on the connection between the two carriages on the rail over the ball screw, a comparison is shown in fig. 3.3.

The pre-load device is built up of a threaded rod, a screw nut and a shim. For attaching the threaded rod in the flux of force of the force sensor, the left end is fixed in a threaded part connected to the sensor. The right part connected to the sensor has a drill hole without thread. Screw nut and shim can be adjusted to pre-load the sensor. If an additional tensile force on the

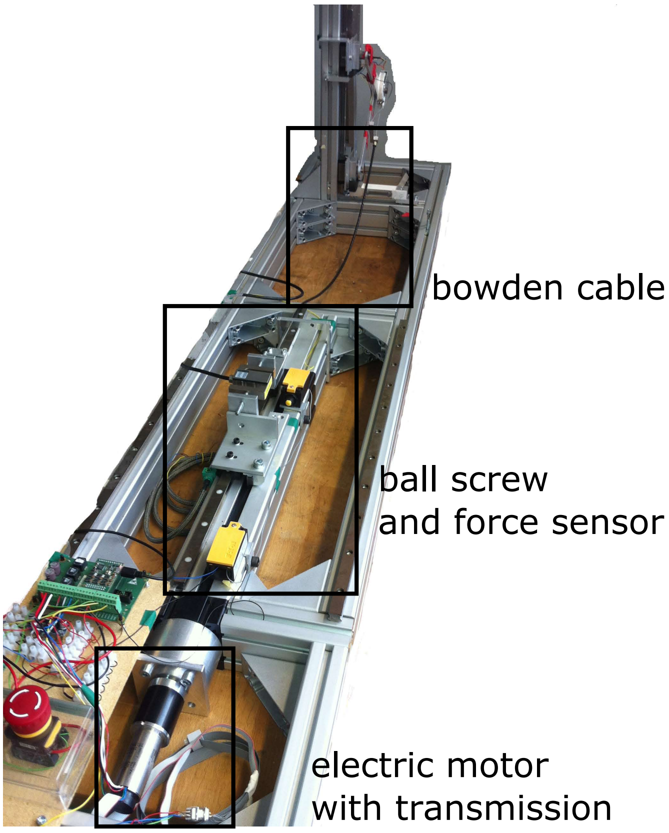

Figure 3.2.: The drive-train of MARCO Hopper II. It consists of an electric motor with mounted transmission and encoder to measure the position of the motor. A ball screw converges the rotation of the motor in a translational movement of the carriages attached to the ball screw. The two carriages move on the rail and are connected to each other with a force sensor. The second carriage is attached to the Bowden cable which is connected to the pulley of the leg.

sensor is raised the threaded rod can move freely. The pre-loading of the sensor is necessary to get linear behavior of the sensor.

3.1.3 Sensor concept and implementation

To be able to implement a proper control and to measure and evaluate the motion of the robot leg, the test-bed is in need of different sensors. Two types of dimensions, rotational- and translational positions and forces have to be measured. The sensors used on the leg and on the drive-train have been mentioned before. Now the settings and implementation of those is described.

Position sensors

The existing test bed contained already some position sensors. Through potentiometer sensors the positions of the hip x_h, the foot x_f and the carriage with the attached cable are measured. An encoder measures the angle of the motor ϕ_M and through some kinematic equations (expressed

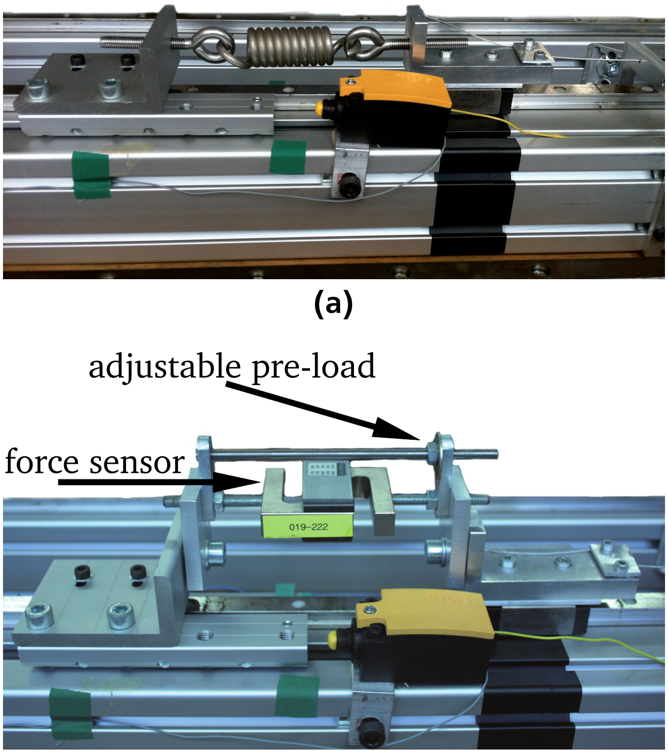

Figure 3.3.: The different concepts of the connection in the drive-train are shown. In (a) a spring is fixed between the two carriages. SEA concepts can be investigated. In (b) the force sensor takes the place of the spring. A force-control approach is possible. Over the sensor the device for pre-loading the sensor is shown.

through the transmission rations of motor transmission i_{T} and ball screw i_{bs}) it measures the position of the carriage x_{bs} attached to it.

$$x_{\mathrm{bs}} = \frac{\phi_{\mathrm{M}}}{i_{\mathrm{T}} i_{\mathrm{bs}}} \tag{3.1}$$

A disadvantage of the available sensors on the hip and the foot were the limitation of travel. The position of the foot can be measured with the existing sensors and some new designed adapters. For measuring the position of the hip and also the angle of the knee ϕ an IMU has been attached to the leg.

Encoder at the motor

The encoder of the motor is a device provided by Maxon (see Fig. 3.2). It measures the current angle of the motor. Through that also the angular velocity of the motor $\dot{\phi}_{\mathrm{M}}$ could be determined.

Some problems with the encoder made it difficult to work with it in a proper way. An internal error leads to the misinterpretation of direction of rotation. When the error occurs, one direction of travel is not recognized. A proper position or velocity control based on sensor information provided by the motor is not possible until the error will be found. For the control concept of these work does not depend on this information, the error will be neglected.

Table 3.2.: Properties of the drive-train

properties drive-train	
motor	maxon EC-4pole, $P = 200$ W
transmission	maxon GP 42 C, $i = 91/6$
ball screw	item Industrietechnik KGT VK14, $i = 314$
carriages	item Industrietechnik GmbH, PS 4-15
force sensor	Scaime, ZF 0-100 kg No. 031018
motor controller	Escon Module 50/5, 4-Q, No. 438725
motor controller motherboard	Escon Module Motherboard, No. 438779
motor encoder	maxon Motor AG, Encoder MR, Typ ML, No. 225778
power source - motor	U=22-29 V, I=10.5 A, P=300 W
power source - sensors	U=24 V, I=0.01-2 A
embedded hardware device	NI, myRIO

Potentiometer position sensor of the foot

For measuring the position of the foot x_f, a potentiometer sensor provided by BURSTER PRÄZISIONSMESSTECHNIK is used (see fig. 3.1). It is attached to the linear bearing of the foot. A drawing for the used adapter can be found in the appendix (see fig. A.3). The signal is received by the MYRIO.

IMU at the thigh

The position of the hip x_h and the angle of the knee ϕ are determined with the sensor information provided by the IMU attached to the thigh.

Basically the IMU measures the angle enclosed by the thigh and the vertical rail of the linear bearings ψ. The angle of the knee is calculated internally.

$$\phi = 2\left(\frac{\pi}{2} - \psi\right) \tag{3.2}$$

Also the position of the hip x_h is calculated with the information of foot position x_f, the length of one leg segment l_l and the angle ψ.

$$x_\mathrm{h} = x_\mathrm{f} + 2\sin\left(\frac{\pi}{2} - \psi\right) l_\mathrm{l} \tag{3.3}$$

During impacts, when the leg becomes stretched and when the foot hits the ground, the rate of change of ψ is very high. At this points the signal from the IMU tends to high peaks that do not reflect the real values for ψ. Therefore, the signal for the calculation of the knee angle, the hip position and all their derivations is not very precise at this moment. All measures to control the system with these values have to be designed with these circumstances in mind.

Force sensors

Force sensors have not been a part of the original concept of the test-bed. At two points the measurement of forces is necessary. Ground reaction forces are one important quantity for evaluating motions, which should mimic legged locomotion. Therefore, the inquiry of this data is important.

The knowledge of the force attacking on the end of the bowden cable makes the evaluation of the effective knee torque much easier. A force sensor between the carriage connected to the drive train and the other carriage attached to the bowden cable gives insight into this matter.

Two kinds of force sensors were used, a load cell [3] in the form of a beam (see fig. 3.4) and a different force sensor ("“S"”-double beam) [2] (see fig. 3.3). Both sensors base on the change of resistance due to deflections of strain gauges.

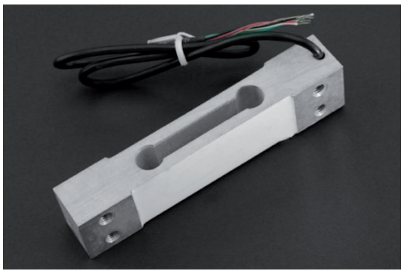

Figure 3.4.: The force sensor used to measure the ground reaction force F_{GRF} [3].

Determining properties of the force sensors

Load cells are used for measuring the forces. A load on the sensor leads to a change of the output voltage. For there are no data sheets for the sensors available, the load - output voltage relationship has to be determined.

For identifying the load/ output voltage relationship, a simple experiment is conducted. The load cell is rigidly attached on its one end. A variable weight is added to the other end. The resulting output voltage can be related to the attached weight and therefore to the actual force on the sensor. Resulting data from the calibration can be found in fig. A.1. Especially the sensor for measuring the force in the drive-train has to be calibrated properly though it measures the controlled variable. The used force sensors inherit a measuring range in which the output voltage depends linear from the force. Beneath a certain force value, the output signal gets non-linear. Therefore, the force sensors have to be pre-loaded to deliver reliable information.

Implementation of the force sensor - force in the drive train

The derived linear law for calculating force values F_{dt} from the output voltage U_{Sout} is:

$$F_{\mathrm{dt}} = \frac{g}{1000}\left(-\frac{0.0332223}{2.56466}10^{5}U_{\mathrm{Sout}}\right) - F_{\mathrm{pl}} \tag{3.4}$$

The sensor will be pre-loaded with a force $F_{\mathrm{pl}} = 200$ N necessary to leave the non-linear range of the sensor. Before each experiment including force-control the pre-load device is tuned to set the output force to $F_{\mathrm{dt}} = 0$.

For implementing the force sensor in the drive train an adapter had to be developed. Drawings for these can be found in the appendix (see fig. A.1). A second force sensor with an extended range of measurement can be used. The alternative for the adapter can also be found in the appendix in fig. A.2.

The used force sensor can be replaced by a sensor similar to the sensor used to measure the ground reaction force. These type of load cells are cheaper and an alternative should be presented, for the current force sensors can not be used permanently in the test bed. One alternative construction for the implementation is presented.

For the construction of the adapter already available aluminum profiles from *item Industrietechnik GmbH* with a length of $l_{\mathrm{iP}} = 0.1$ m could be used. This profile acts like a beam with one end rigid attached to the ground while the other end is attached to a parallel motion. The force takes effect at the end with the parallel motion.

A drawing of the possible solution is shown in fig. 3.5. The mechanical drawings could be found in the appendix (see fig. A.5 and fig. A.6). A solution for the calculation of resulting forces and deflections of this kind of problem can be found in [14][p. 125]. The properties of the profile used for this calculation are summarized in the table 3.3.

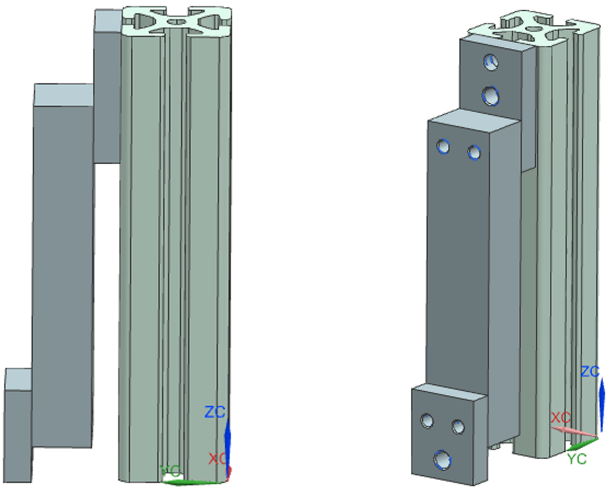

(a) **(b)**

Figure 3.5.: Drawing of the the adapter for the alternative sensor measuring the force in the drive-train. The long gray part connected with two drilled parts to the ITEM profile represents the sensor (beam load cell). The connection to the carriages is possible via the free threaded hole and the ITEM profile.

Table 3.3.: Properties of *item* Profil 5 40x20, natur, Art. No. 0.0.370.04

properties ITEM profile	
material	aluminum
$I_{\mathrm{y,iP}}$	$5.14\ \mathrm{cm}^4$
E modulus aluminum E_{al}	$7.09\ \mathrm{kN\ mm}^{-2}$
mass per length	$0.89\ \mathrm{kg\ m}^{-1}$
length l_{iP}	$0.1\ \mathrm{m}$

The author used the smallest available profile for the calculation. If the smallest profile passes the test, possible other profiles could easily provide the desired stiffness values.

To determine, if the stiffness of the developed adapter is sufficient, a threshold for the displacement of the adapter has to be given. The threshold is set to $w = 1\text{mm}$.

The displacement w of the chosen profile can be calculated by:

$$w_{\text{max}}(l) = \frac{F_{\text{dt}} l_{\text{iP}}^3}{12\, E_{\text{al}} I_{\text{y,iP}}} \tag{3.5}$$

Values for the displacement depend on the force F_{dt} applied at the end of the profile. Two examples for possible forces shall be regarded.

On the one hand the motor can generate a maximum force $F_{\text{dt,M}}$ limited by the motor properties (maximum current $i_{\text{M, max}}$, torque constant k_{M}) and transmission properties of the drive-train (transmission ratios of motor transmission i_{T} and ball screw i_{bs} and the efficiencies of both, η_{T} and η_{bc}; see fig. 3.7, fig. 3.8 and fig. 3.9).

$$F_{\text{dt,M}} = i_{\text{M, max}} k_{\text{M}} i_{\text{T}} \eta_{\text{T}} i_{\text{bs}} \eta_{\text{bs}} \tag{3.6}$$

This value is regarded as an upper limit. On the other hand there is a range of torque, the knee is operated with. It is not likely that there will be much higher forces during the operation of the test-bed.

Table 3.4.: Displacement of adapter due to maximum force

Force F	Displacement w_{max}
$F_{\text{dt,M}} = 471$ N	0.01 μm

Values of the resulting displacement can be found in the table 3.4. Even for the maximum force, the displacement is very low and does not even comes close to the threshold of $w = 1\text{mm}$. The stiffness of the used profile is regarded as sufficient.

Another thing to be determined is the signal quality of the force sensor. A certain noise signal overlays the force signal. One measure to make the signal better is to calculate an average over a certain number of signal values N. In Fig. 3.6 there is shown the signal of the force sensor without load and a different level of average calculation. The measuring frequency used is $\omega = 200$ Hz. The time used to get an average value is given by:

$$T = \frac{N}{200\ \text{Hz}} \tag{3.7}$$

The effective measuring frequency decreases, because only for a frequency of $200/N$ Hz a new value is given after the average calculation. For this reason the number of signals used to calculate an average value is set to $N = 20$ in the test-bed. The noise is reduced while the dynamic of the sensor stays on an acceptable level.

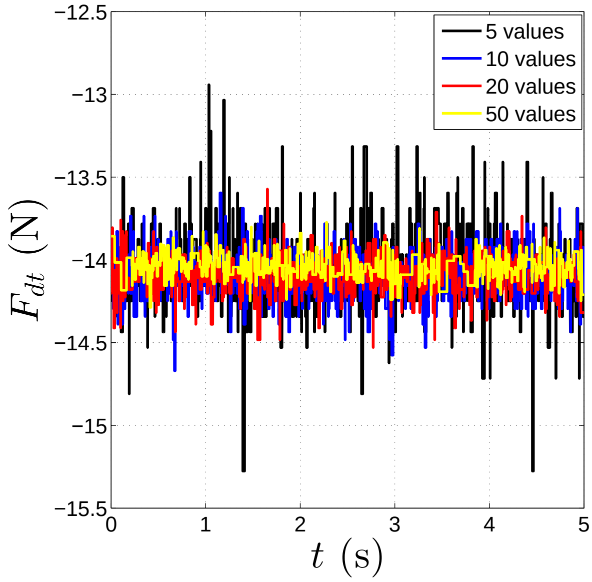

Figure 3.6.: The signal of the force sensor without load. Measured is the force in the drivetrain F_{dt}. Different colors of the plot show the signal with a certain quantity of signal values used to calculate the average signal.

Implementation of the force sensor - ground reaction force

The implementation of the force sensor for the ground reaction force is similar to the implementation of the sensor for the force in the drive-train. Also a law for calculating the force dependent on the output voltage can be derived through an experiment.

$$F_{\mathrm{GRF}} = \frac{g}{1000}\left(-\frac{0.0215042}{6.51085}10^5 U_{\mathrm{Sout}}\right) \tag{3.8}$$

In the case of this sensor a pre-loading is not necessary. The force resulting from the weight of the leg resting on the sensor is sufficient as a pre-load. Also the calculation of an average signal value was not be regarded necessary. The sensor signal should not be used for control tasks. Therefore, a signal processing during experiments is not necessary at the moment.

An adapter for mounting the sensor beneath the foot has been developed. The mounted sensor is shown in fig. 3.1. Mechanical drawings of the adapter can be found in the appendix (see fig. A.4 and A.5).

Implementation of an signal amplifier

For the output voltage of both force sensors are very low (in the range of mV), the signals have to be amplified. A self-made differential amplifier takes this task.

$$U_{\mathrm{a}} = U_{e2}\frac{R_1+R_2}{R_1}\frac{R_4}{R_3+R_4} - U_{e1}\frac{R_2}{R_1} \tag{3.9}$$

All used force sensors give out two voltage values U_{e1} and U_{e2}. The difference between both voltage values varies and depends on the deflection of the sensors, which depends on the force.

An operational-amplifier (op-amp) in a circuit with certain resistances (R_1, R_2, R_3 and R_4) can amplify the signal (see fig. 3.7).

An amplification factor K is equal to the proportion of the resistances $\frac{R_2}{R_1}$ if $R_1 = R3 = 1k\Omega$ and $R_2 = R_4 = 100k\Omega$ [1]. The value for the amplification was chosen to $K = 100$ because, in this case, the sensor signals fit in the range of $U = 0-5$ V, which is the input range of the *MyRIO*.

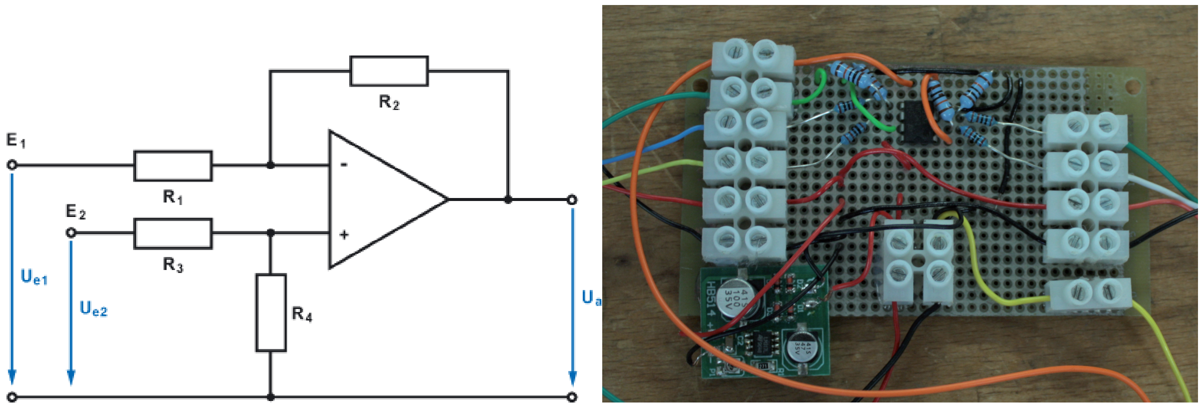

(a)

(b)

Figure 3.7.: (a) Principle of a differential amplifier. It amplifies the differential signal $U_{e2} - U_{e1}$ by the factor K. [1](b) Implementation of the amplifier. The signals of both force sensors have to be amplified. Both are amplified with the same factor. The amplifier needs an own voltage source (down left). Sensors are provided with $U = 10$ V and the amplifier with $U = 25$ V.

3.2 Simulation models Marco Hopper II

To validate the analytical derived findings and to test possible control strategies, simulation models have been developed. They serve different purposes, which are explained in the following. As a simulation environment *MATLAB Simulink* and parts of *SimMechanics* were used. All presented simulation models can be found on the attached CD or on the wiki-page[1].

Selection of suitable solvers for different models

The chosen solvers for a model has a big influence on the results. Early experiments showed this and, therefore, all available solver were tested for their performance. An example illustrates this circumstance.

A single mass oscillator is simulated. For a certain spring rate k and an initial condition for the mass $x = x_0$ the system performs oscillations over a certain time $T = 10$ s. The multi-body system developed with the relationships in chapter 2.1.3 should show the same behavior tuned with the same parameters $k_\text{v} = k$ and $x_{\text{h},0} = x_0$. The chosen solver of the multi-body model has an influence on the simulated oscillation. For this reason the gained results with each solver have been compared.

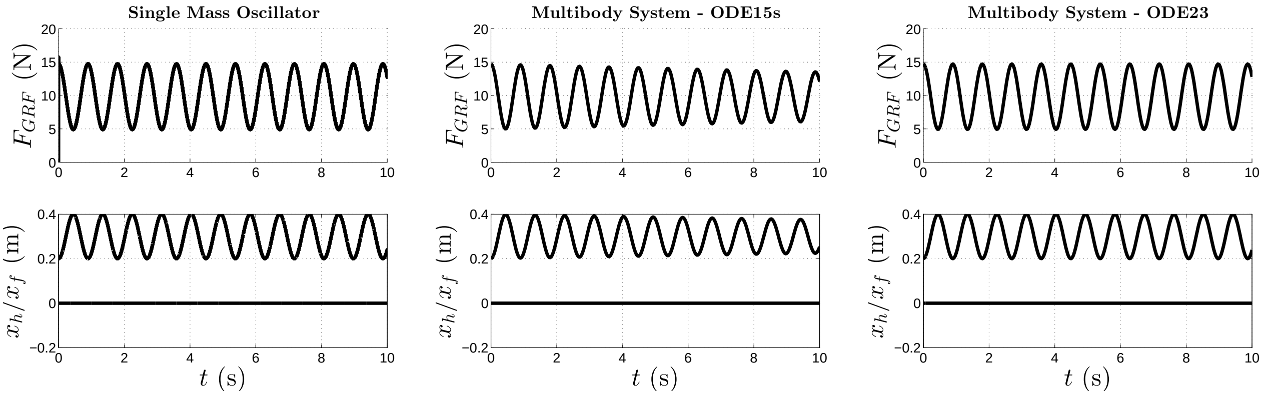

Figure 3.8.: [SIM] Motion- and force-patterns derived from a single mass oscillator model and a multi-body system model. The parameters are set to $m = m_1 = 1$ kg, $k = k_\text{v} = 36$ $^{N}/_{m}$,$x_0 = x_\text{h} = 0.2$ m. The solver ODE15s for the multibody-system brings some kind of damping in the simulated system. The oscillation ceases. For the solver ODE23 used for the multi-body model and ODE45 for the single mass oscillator the simulation results are equal.

As to see in Fig. 3.8 the use of different solvers gains different results for the same model and simulation parameters. The figure in the middle shows a ceasing oscillation that hints to a damping effect/ energy loss during the oscillation. For there are no energy sinks or damping models active, the shown behavior is falsified through the solver. All solvers have been tested to gain the most similar results to the single mass oscillator.

---

[1] http://wiki.ifs-tud.de/biomechanik/abschlussarbeiten/oehlke

The best results could be gained with the solver ODE23 for the multi-body model. Therefore, it will be used further on for multi-body simulations. For the single mass oscillator model the standard solver ODE45 will be used. The structure of the different models will be presented in the following chapters.

No further changes to the simulation settings have been made. The simulation is performed with variable time steps internally calculated by the solver. Zero-crossing detection was disabled in all used blocks. The nature of the simulated test-bed makes this necessary. A lot of zero-crossings for different velocities, accelerations and positions happen during a regular hopping motion. For these values are also used for different force models a lot of sub-systems are involved. Each of them could bring the simulation to abortion due to much zero-crossings. As a consequence all detection of this event is disabled.

3.2.1 Single Mass Oscillator

The single mass oscillator model is founded on the set of differential equations discussed in chapter 2.1.1. The equation eq. 2.1 describes the core behavior of the system.

Up to now, all models performed oscillations without leaving the ground. Additional the simulated system should be able to perform a hopping motion. The differential equations are expanded with another degree of freedom. A foot point x_f with an extra mass m_4 and a reaction force by the ground F_GRF are inserted (see fig.3.9). Now the equations of motion have to be separated for a phase with ground contact (stance phase) and a phase without ground contact (flight phase). The differential equations for the stance phase are set through:

$$\begin{aligned} m\ddot{x} &= k(l_0 - x + x_\mathrm{f}) - mg \\ m_4\ddot{x}_\mathrm{f} &= -k(l_0 - x + x_\mathrm{f}) + F_\mathrm{GRF} - m_4 g \end{aligned} \tag{3.10}$$

The differential equations during the flight phase are given by:

$$\begin{aligned} m\ddot{x} &= k(l_0 - x + x_\mathrm{f}) - mg \\ m_4\ddot{x}_\mathrm{f} &= -k(l_0 - x + x_\mathrm{f}) - m_4 g \end{aligned} \tag{3.11}$$

During the flight phase the system is not influenced by the ground. This behavior is realized with a *switch*-block in *Matlab*. The ground reaction force takes only effect on the foot when the conditions $x_\mathrm{f} < 0$ (the foot is on the ground) and $F_\mathrm{GRF} \geq 0$ (the force by the ground can only push the foot) are met. If not, the force is set to zero.

In Fig. 3.9 an example for a possible ground model is shown. The ground behaves like a parallel mechanism of a spring and a damper. For the ground model is explained in a later chapter, this simple ground model serves to show the principle. The preset for the ground spring stiffness rate and the ground damping rate are $k_g = 100000$ N/m and $d_g = 100$ Ns/m. An alternative ground model can be used easily.

The stiffness of the spring k could be adjusted in different ways. For simple experiments k got a fixed value. It is also possible to implement a variable k after a certain law during the movement. The model for this variable k is explained when used. This equations are represented as a block diagram in MATLAB Simulink. The used solver is ODE45. For a single mass oscillator with flight phases is simulated, the value for m_4 is set near to zero.

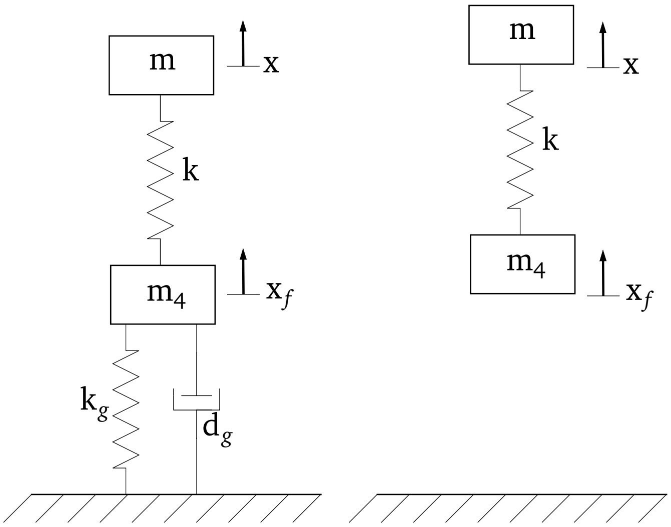

Figure 3.9.: Sketch of the model for the single mass oscillator. The structure got two degrees of freedom x and x_f. A spring with the rate k attached between the hip mass m and the foot mass m_4 drives the oscillation. The ground consists of a parallel spring with the rate k_g and a damper with the rate d_g. The ground forces effect the oscillator only during the stance phase.

3.2.2 Simulation of the segmented leg

A second model is built with the *SimMechanics* library of *MATLAB Simulink*. The goal is to simulate the dynamic behavior of the multi-body system given through the existing test bed. In *SimMechanics* rigid bodies with their dimensions, distributed masses and resulting dynamic behavior can be simulated. The bearings that connect rigid bodies with each other are represented by certain degrees of freedom, which the bodies got to each other. Also forces exerted in the bearings can be included in their effects on the system. The behavior of the system is the same like the one described through the equations in chapter 2.1.4.

Masses in the simulated system

The segments of the leg ("thigh" and "shank") are represented by rigid bodies with distributed masses. The dimensions of the links in the test bed were chosen according to the reality (see Fig.3.5 and [9]). In difference to the real links the segments in the simulation are rectangular prisms with the density of aluminum ρ_al. The connections with the roller bearings are at the exact end of each link and not through drill holes in the links.

In the test-bed the segments are not rectangular but have rounded ends behind the drill holes. Therefore, the mass of the segments in simulation is slightly less than the mass of the real segments. This changes were made to simplify the simulated structure. The masses at the foot m_4, the knee m_3 and the hip m_1 come into account as point masses. As they move only translational, this assumption is valid [13]. All masses can be tuned to check the effects of changes to the test bed and to find an ideal distribution of masses between foot, hip, knee and links.

Table 3.5.: Properties of the segments "'shank"' and "'thigh"' used in the model

Properties of segment	
length link	$l_l = 0.25$ m
width link	$w_l = 0.005$ m
height link	$h_l = 0.04$ m
density aluminium	$\rho_{al} = 2700$ kg m^{-3}

Bearings in the system

The bearings of the real test bed are represented as kinematic constraints between the rigid bodies. Connected bodies have one degree of freedom (rotational or translational) to each other in this case. All other degrees of freedom of the connected parts are locked. In these directions forces and torques are transferred to the next part in the leg.

There are two linear bearings (hip and foot) and three rotational bearings (hip-, knee- and ankle-joint) in the system. The rotational bearings/ joints represent actual behavior of a real leg. The linear bearings represent the constraints given by the one degree of freedom hip x_h and foot x_f should have during a hopping motion.

Forces that take effect on the system behavior through the linear bearings should be minimized, for they have no counterpart in biological legs and falsify results. This measures can only be executed in the test-bed. The model only represents the test-bed and is therefore near to the real device. In all bearings friction forces influence the motion. Models for each bearing were developed and are presented in the next section.

Through the bearings forces and torques can be added to the system. All external and internal forces, besides the gravitational forces on the masses, are added at a bearing.

External and internal forces on the segmented leg

Forces influence the behavior of the system at different places of the segmented leg (see Fig. 3.10). In the following they are divided by the corresponding bearing, on which they exert influence. Reaction forces between the segments are not included.

Forces on the linear bearing at the foot

There are three forces influencing the linear bearing of the foot. The first two forces are reaction forces due to stops in the test-bed, the ground reaction force F_{GRF} and the force by the hip stop F_{HF}.

Both forces base on the ground model of the system, which will be explained in a later chapter. They hold only non-zero values if certain conditions are met. Similar to the model of the single mass oscillator the ground reaction force is equal to zero $F_{GRF} \neq 0$ if the conditions $x_f < 0$ and $F_{GRF} \geq 0$ are given. The force at the hip-stop is unequal to zero $F_{HF} \neq 0$ if the foot position

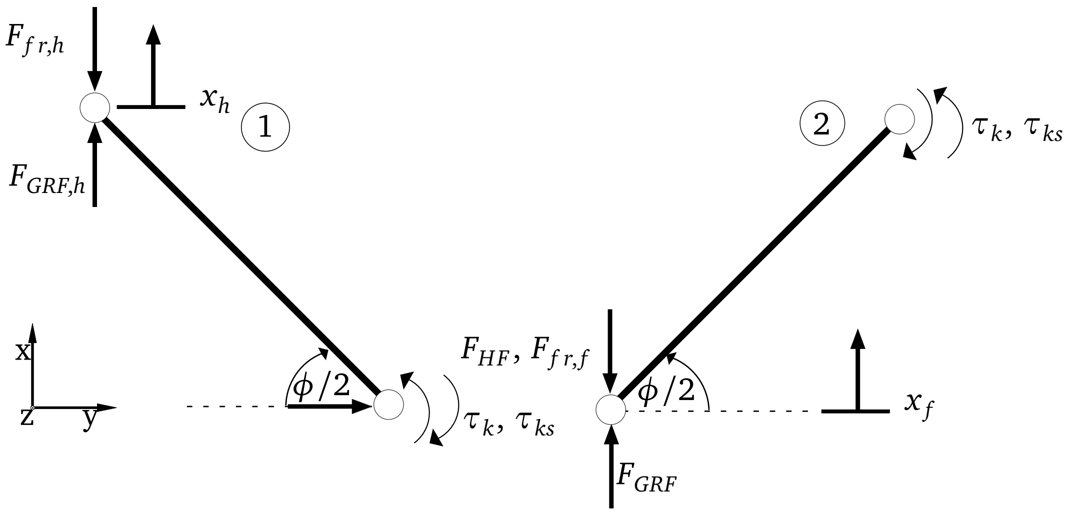

Figure 3.10.: Forces and torques introduced through the bearings in the simulation. Friction forces $F_{\mathrm{fr,h}}$ and $F_{\mathrm{fr,f}}$ and reaction forces of the stops F_{GRF}, $F_{\mathrm{GRF,h}}$ and F_{HF} act on the foot and the hip. On the knee two torques take influence, the actuation torque τ_{K} and the torque by the knee stop τ_{ks}.

gets higher than the position of the hip-stop $x_{\mathrm{f}} > x_{\mathrm{hs}} = 0.2$ m and the force is lower than zero $F_{\mathrm{GRF}} \leq 0$ (the foot is pushed back by the hip-stop). When the foot hits the hip-stop, a force limits the movement.

The third force, which influences the movement of the foot, is the friction force in the bearing $F_{\mathrm{fr,f}}$. This force always apposes the direction of movement. A special set of parameters has been developed for the friction model of the linear bearing at the foot. The parameters for all friction models are summarized in chapter 3.2.5.

Torques on the rotational bearing at the foot

The second bearing of the foot is a roller bearing in which also a friction torque $\tau_{\mathrm{fr,f}}$ influences the movement of the foot-shank connection. Friction torques due to roller bearings are comparatively low.

For the rotational roller bearings a constant friction torque can be estimated by tools provided by the producer of the bearings [6]. Necessary for that are radial and axial loads of the bearing $F_{\mathrm{bearing,\ r}}$ and $F_{\mathrm{bearing,\ a}}$, a maximum rotational speed of the bearing n_{bearing} and some operating conditions like temperature T_{bearing} and the used grease. The viscosity of the grease LGMT2 can be found in [7]. Both bearing load forces have been estimated.

The axial load is estimated to be zero because no load in this direction is induced. For the radial load a higher value is estimated, than will occur in the reality, to make sure that the real friction force is underneath the estimated one. Experiments show a ground reaction force of $F_{\mathrm{GRF,max}} \approx 60$ N for simple hopping experiments. This is a rough estimation of the radial load, which the roller bearings will see in the leg. A force of $F_{\mathrm{bearing,\ r}} = 100$ N seems not to far away from reality to estimate resulting friction torques in the roller bearings. This resulting friction torque is added as an additional torque at the hip-, knee- and ankle-bearing of the model. The data used to estimate the friction torque could be found in Fig. 3.6.

Table 3.6.: Properties of the roller bearings for the estimation of the friction torque

Properties roller bearings	
bearings used	SKF roller bearing 61800
radial load	$\mathrm{F}_{\text{bearing, r}} = 100$ N
axial load	$\mathrm{F}_{\text{bearing, a}} = 0$ N
maximum rotational speed	$\mathrm{n}_{\text{bearing}} = 40$ U min^{-1}
operating temperature	$\mathrm{T}_{\text{bearing}} = 23$ °C
viscosity grease LGMT2	$\nu_{\text{grease, 40°C}} = 110$ mm$^2 s^{-1}$
resulting max. friction torque	$\tau_{\text{fr}} = 0.00122$ Nm

A resulting friction torque of $\tau_{\text{fr}} = 0.00122$ Nm is compared to the other forces in the system so low that it shall be neglected for all roller bearings in the simulation.

Torques on the rotational bearing at the knee

The actuation of the leg takes place at the knee through the torque τ. One important difference between the test-bed and the simulation model lies within the method the torque is introduced to the knee.

On the test-bed, the pulley is fixed on the shank. The torque generated by the cable takes effect on the lower end of the thigh, not on the knee-joint itself. There is no anti-torque on the shank, because the counteracting force of the force attacking at the pulley, attacks outside the leg in the drive-train (see Fig. 2.15).

In the simulation model the torque is directly generated in the knee-joint. A torque and a counteracting torque are generated in thigh and shank where the knee is attached (see Fig. 3.10). To gain the same effect with a torque in the simulation model as in the reality, only half of the torque has to be used. The following dynamic equations show the difference.

$$
\begin{aligned}
&m\ddot{x} = F_{\text{kx}} \\
&\textbf{equilibrium of torques, subsystem thigh, at the hip:} \\
&\sum \tau_h : 0 = \tau + F_{\text{ky}} \sin\left(\frac{\phi}{2}\right) l_1 + F_{\text{kx}} \cos\left(\frac{\phi}{2}\right) l_1 \\
&\textbf{equilibrium of torques, subsystem shank, at the foot:} \\
&\sum \tau_f : 0 = -\tau - F_{\text{kx}} \cos\left(\frac{\phi}{2}\right) l_1 + F_{\text{ky}} \sin\left(\frac{\phi}{2}\right) l_1 \\
&F_{\text{kx}} = -\frac{\tau}{\cos(\frac{\phi}{2}) l_1} \\
&m\ddot{x} = -\frac{\tau}{\cos(\frac{\phi}{2}) l_1}
\end{aligned}
\tag{3.12}
$$

These equations describe the relationships in the simulation with torque and counter-torque at the knee joint. The following equations describe the relationships in the test-bed. There is no counter-torque for τ at the shank.

$$\begin{aligned}
&m\ddot{x} = F_{\mathrm{kx}} \\
&\textbf{equilibrium of torques, subsystem thigh, at the hip:} \\
&\sum \tau_h : 0 = \tau + F_{\mathrm{ky}} \sin\left(\frac{\phi}{2}\right) l_1 + F_{\mathrm{kx}} \cos\left(\frac{\phi}{2}\right) l_1 \\
&\textbf{equilibrium of torques, subsystem shank, at the foot:} \\
&\sum \tau_f : 0 = -F_{\mathrm{kx}} \cos\left(\frac{\phi}{2}\right) l_1 + F_{\mathrm{ky}} \sin\left(\frac{\phi}{2}\right) l_1 \\
&F_{\mathrm{kx}} = -\frac{\tau}{2\cos(\frac{\phi}{2}) l_1} \\
&m\ddot{x} = -\frac{\tau}{2\cos(\frac{\phi}{2}) l_1}
\end{aligned} \tag{3.13}$$

A comparison shows that for the same amount of acceleration $\ddot{x}$ of the mass m on the test-bed, two times the torque as with a counter-torque in the knee is required. Therefore, the simulation model is introduced with half the torque generated in the real test-bed to gain the same results.

Second, there is the torque at the knee produced by the knee-stop preventing over-extension of the knee joint τ_{ks}. The torque is introduced in the manner of a linear rotational damper with a very high damping constant acting only in one direction, against the extension.

$$\tau_{\mathrm{ks}} = -\dot{\phi}\, d_{\mathrm{k}} \tag{3.14}$$

The torque is non-zero if a certain knee angle is reached $\phi = \phi_{\mathrm{max}}$ and the angular velocity of the knee is bigger than zero.

The third torque influencing the knee joint is the friction torque of the roller bearing $\tau_{\mathrm{fr,k}}$. As shown before this torque is very low, so it is neglected.

Forces on the linear bearing at the hip

Two forces influence the linear bearing at the hip. The first one is the force at the hip stop $F_{\mathrm{GRF,h}}$. It is a kind of ground reaction force for it is only non-zero when the position of the hip is underneath the hip-stop $x_{\mathrm{h}} < x_{\mathrm{hs}}$, the force can only be positive $F_{\mathrm{GRF,h}} > 0$ and the model for the force bases on a ground model.

The second force is the friction force in the bearing $F_{\mathrm{fr,h}}$. The parameters of this force are also summarized in chapter 3.2.5.

Forces on the rotational bearing at the hip

The only torque, influencing the behavior of the hip joint, is the friction torque of the roller bearing $\tau_{\mathrm{fr,h}}$. For it is very low, it is neglected.

3.2.3 Drive-train model

After a simulation model of the segmented leg has been presented, a model of the drive-train with its different components is presented next.

Motor

The motor of the drive-train is represented by a set of differential equations, describing the equilibrium of torques and the electric properties of the motor [22] (p. 186). Necessary for this description are the mass moment of inertia of the drive-train $\theta_{\text{M, sum}}$, the motor torque constant k_M, the motor damping constant d_M, the load torque of the motor τ_L, the motor current i_M and derivations of the angular motor position ϕ_M. To describe the electric equilibrium of the motor, the voltage of the motor U, the internal electric resistance R_M, the inductance L_M and the rotation speed constant k_E are necessary.

$$\begin{aligned} \theta_{\text{M, sum}}\ddot{\phi}_\text{M} &= i_\text{M} k_\text{M} - \tau_\text{L} - \dot{\phi}_\text{M} d_\text{M} \\ U &= L_\text{M}\dot{i} - R_\text{M} i - k_\text{E}\dot{\phi}_\text{M} \end{aligned} \tag{3.15}$$

The moments of mass inertia of the transmission θ_T and the ball screw θ_bs are taken into account in the equation of motion of the motor. Necessary for that are the mentioned moment masses of inertia and the transmission ratio of the ball screw i_bs.

$$\theta_{\text{M, sum}} = \theta_\text{M} + \theta_\text{T} + (1/i_\text{bs})\theta_\text{bs} \tag{3.16}$$

All constants are gained from the data sheet of the motor. Only the damping constant of the motor d_M is not known. It is suggested to estimate this parameter by a value near to zero. For the parameter can not be determined exactly, it is set to $d_\text{M} = 0.00005$ Nms/rad. Therefore, the behavior of the motor will come close but not exact to the real behavior.

Table 3.7.: Properties of the motor used in the model

Properties of the motor maxon EC-4pole 30	
nominal current	$\text{i}_{\text{M, max}} = 10.5$ A
resistance	$\text{R}_\text{M} = 0.102\ \Omega$
inductance	$\text{L}_\text{M} = 0.0163$ mH
rotation speed constant	$\text{k}_\text{E} = 700\ \text{V}^{-1} min^{-1}$
torque constant	$\text{k}_\text{M} = 13.6\ \text{mNm A}^{-1}$
mass moment of inertia	$\theta_\text{M} = 3.33 * 10^{-6}\ \text{kgm}^2$
damping constant	$\text{d}_\text{M} = 0.00005\ \text{Nms rad}^{-1}$

Transmission

The transmission after the motor is represented by a transmission ratio i_T and an efficiency η_T. Also it possesses a mass moment of inertia θ_T. This value is given by the data sheet of the component.

Table 3.8.: Properties of the transmission used in the model

Properties transmission maxon GP42 C	
transmission ratio	$i_T = 91/6$
efficiency	$\eta_T = 0.81$
moment of mass inertia	$\theta_T = 15 * 10^{-6}$ kgm^2

Ball screw

The ball screw in the drive-train changes translation into rotation (forces F to torques τ, respectively between translational- x_{bs} and rotational movement ϕ_{bs}) and vice versa. There are different possible models to include all effects in the simulation.

There have been different models developed for this thesis and each one shows certain weaknesses. No model was able to explain every situation during the tests. For the simulation should be similar to the test-bed during the hopping motion, a model that reaches the closest results for this special case of movement should be regarded as the best model.

Direction dependent behavior

The ball screw is included in the simulation model by a transmission ratio i_{bs} and an efficiency η_{bs}. In [22] p.51 f. it can be found a relationship for the transmission ratio of ball screws dependent on the radius of the ball screw r_{bs}, its slope angle α_{bs} and its friction angle ρ_{bs}.

$$\begin{aligned}\tau &= F r_{bs} \tan(\alpha_{bs} \pm \rho_{bs}) \\ &\text{and:} \\ x_{bs} &= r_{bs} \tan(\alpha_{bs}) \frac{\phi_{bs}}{2\pi} \\ x_{bs} &= \frac{\phi_{bs}}{i_{bs}}\end{aligned} \tag{3.17}$$

The ratio of transformation between axial force F and torque τ depends on the direction of the movement of the load at the ball screw. This is influenced and quantified by the friction angle ρ_{bs}. With the efficiency $\eta_h = 0.85$, the slope p_{bs} and the diameter d_{bs} of the ball screw given by the producer, $\rho_{bs,ideal}$ can be estimated.

$$\begin{aligned}\alpha_{bs} &= \arctan\left(\frac{p_{bs}}{\pi d_{bs}}\right) \\ \rho_{bs,ideal} &= \arctan\left(\frac{\tan(\alpha_{bs})}{\eta_h}\right) - \alpha_{bs}\end{aligned} \tag{3.18}$$

The resulting value for $\rho_{bs,ideal}$ presents an optimum for a new ball screw in the best condition. To gain a realistic behavior ρ must be bigger than the optimum ρ_{ideal}. For lack of a better value the friction angle is set to $\rho = 1.2\,\rho_{ideal}$. Experiments show a realistic behavior with this value (see Fig. 3.12 and Fig. 3.13). The behavior of the ball screw changes with the change of direction of the movement, which is taken into account through this measurements.

One additional property of the ball screw that can be found, is a velocity dependent friction. A stiction force that is bigger than the coulomb friction force, has to be taken into account. To include this in the simulation model, a velocity dependent force $F_{\mathrm{bs,\,v}}$ acting against the direction of movement is added. It bases on a friction model by *Stribeck* [18]. In chapter 3.2.5 it is explained properly. At this point only the found parameters to gain realistic behavior are presented.

$$F_{\mathrm{bs,\,v}} = \left(F_{\mathrm{c,bs}} + (F_{\mathrm{s,bs}} - F_{\mathrm{c,bs}}) \exp\left(- \left| \frac{\dot{x}_{\mathrm{bs}}}{v_{\mathrm{s,bs}}} \right|^{\delta_{\mathrm{s,bs}}} \right) \right) \tanh(800\dot{x}_{\mathrm{bs}}) + (F_{\mathrm{v,bs}}\dot{x}_{\mathrm{bs}}) \qquad (3.19)$$

The friction force $F_{\mathrm{bs,\,v}}$ is dependent on different parameters $F_{\mathrm{c,bs}}$, $F_{\mathrm{s,bs}}$, $v_{\mathrm{s,bs}}$, $\delta_{\mathrm{s,bs}}$ and $F_{\mathrm{v,bs}}$, which represent the behavior of the force in different regions of velocity $\dot{x}_{\mathrm{bs}}$.

For example a high force is necessary to start the movement of the drive-train. The coulomb friction is relative low compared to this force. A course of the force over a velocity is shown in Fig. 3.11. At every turning point of the movement (the velocity is zero) high force values are necessary to start the movement again.

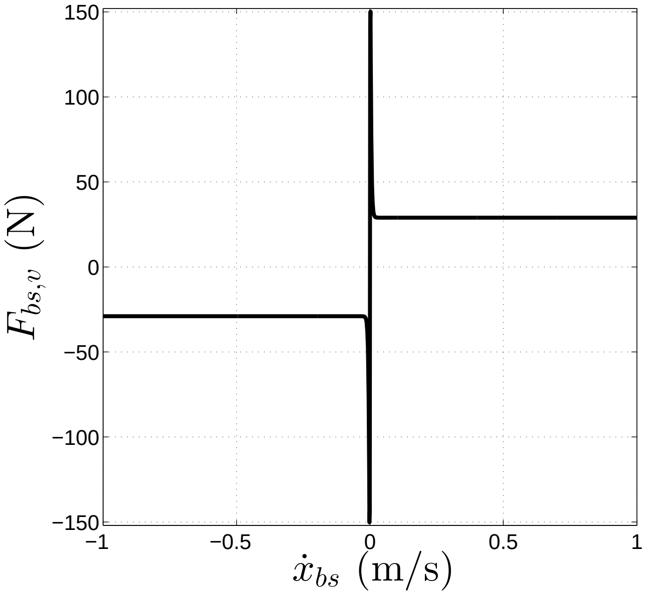

Figure 3.11.: The course of the friction force influencing the ball screw.

The whole force-torque transmission by the ball screw is now given by:

$$\tau = F r_{\mathrm{bs}} \tan(\alpha_{\mathrm{bs}} \pm \rho_{\mathrm{bs}}) - F_{\mathrm{bs,\,v}} \qquad (3.20)$$

The values for the friction model are varied to meet the real conditions in the ball screw. To compare the test-bed and the simulation model, an experiment with a sinusoidal oscillation of the input current of the motor has been performed.

The oscillation is performed over a time of ten seconds. Results of the simulation show that with fixed values for ρ_{bs} and the friction parameters the oscillation stabilizes to a certain amplitude of angular velocity of the motor (see Fig. 3.12). The difference between the both directions is due

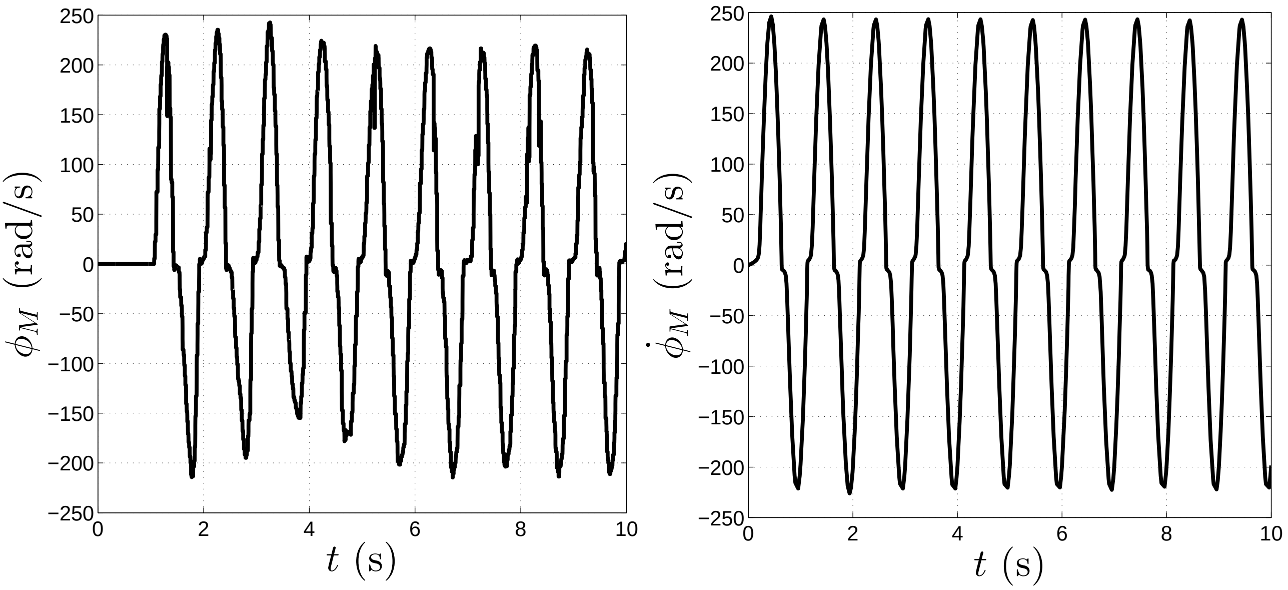

(a)

(b)

Figure 3.12.: [EXP+SIM] Comparison of the angular velocity $\dot{\phi}_\mathrm{M}$ with attached transmission and ball screw of the test-bed (a) and the drive-train model (b). Both systems got a sinusoidal current input of $i_\mathrm{M} = 3.5$ A and a frequency of $f = 1$ Hz. Simulation and experiment show similar apex values and the behavior around a zero velocity is also similar.

to the direction dependent behavior of the ball screw mentioned before. In the simulation and the test-bed similar results for the angular velocity of the motor ϕ_M can be gained. Especially the behavior near a velocity $\dot{\phi}_\mathrm{M} = 0$ is very similar in experiment and simulation.

The movement of the carriage attached to the ball screw is shown in Fig. 3.13. The two left figures((a) and (b)) show experimental behavior of the test-bed. The start from the initial position is shown in Fig. 3.13(a). Fig. 3.13(b) shows the end of the experiment when the carriage hits the bed-stop. The third figure Fig. 3.13(c) shows the behavior of the model.

Each experiment is performed over a period of ten seconds. All three cover a distance of approximately $l = 0.03$ m over this time. The behavior of the test-bed is not very smooth. There are several possible reasons for this.

On the one hand the current of the motor is not as ideal as in the simulation. The internal current control can not result in an exact sinusoidal pattern. Second, the friction can also depend on the current location of the carriage/ball screw. Third, the value for the direction dependency ρ_bs may not be correct. Some motor parameters like the damping constant d_M are also only a approximation of the reality. All this together results in a complicated interdependency of parameters and effects on the results. Therefore, the gained behavior of the simulation model should is regarded as valid with the results achieved by the presented method.

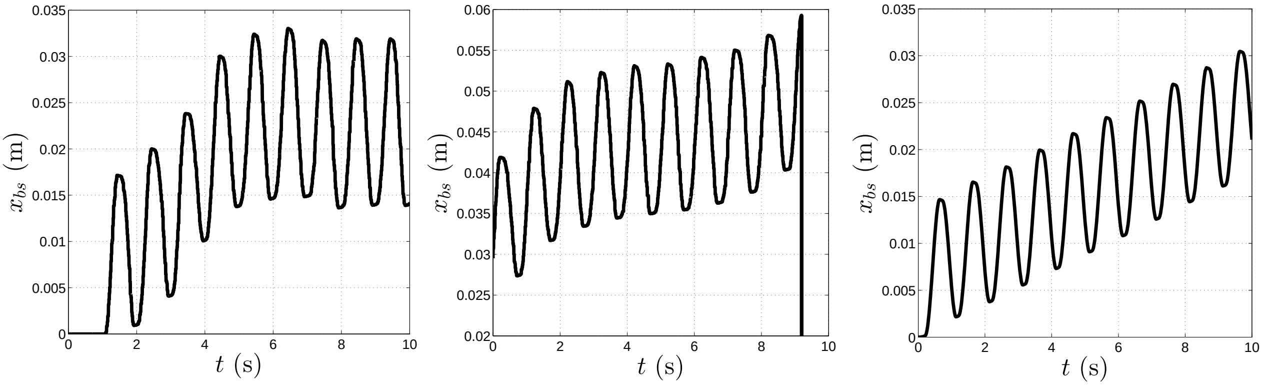

(a) **(b)** **(c)**

Figure 3.13.: [SIM+EXP] Comparison of the position of the carriage x_{bs} with attached transmission and ball screw of the test-bed ((a), movement from inital position and (b), movement until hit of bed-stop) and the drive-train model ((c), movement from initial position). Both systems got a sinusoidal current input of $i_{\text{M}} = 3.5$ A and a frequency of $f = 1$ Hz. All three cover a distance of approximately $l = 0.03$ m during the oscillation. The behavior of the test-bed is not very steady. Reasons for this lie probably in a location dependent behavior of the ball screw and the non-ideal current control of the motor.

Limitation of movement during hopping motion

The presented friction model for the ball screw is unable to explain certain behavior during hopping experiments. Especially the behavior during the fall of the leg after the apex point is slower in the experiment than it is in the simulation. Most likely the current control of the motor is responsible for this behavior. The actual current is oscillating very much, though the desired value is constant (see Fig. 5.4 in chapter 5.2.1).

The assumption is made that these oscillations slow down the fall of the leg. It was not possible to model this behavior of the current to gain the same results. Another way is to model this behavior through a property of the drive train that slows down the fall of the leg similar to the test-bed. It is possible to gain the same behavior in the experiment as in the simulation although not for the same reasons.

One possibility is the presented way.

$$\begin{aligned} F_{\text{bs,v}} &= \tanh(30\dot{x}_{\text{bs}}) \frac{k_{\text{bs,v}}}{\exp(80\dot{x}_{\text{bs}})} \\ \tau_{\text{bs}} &= F r_{\text{bs}} \tan(\alpha_{\text{bs}}) - F_{\text{bs,v}} \end{aligned} \tag{3.21}$$

The suggested function for $F_{\text{bs,v}}$ is over most of the parameter range equal to zero. For a certain velocity lower than zero the function gets a very high slope and limits the velocity of the carriage by the resulting force.

The course of the function is only tuned by one parameter $k_{\text{bs,v}}$. Therefore it is easier to modify and to adjust to the reality, than the friction force in the paragraph before. For hopping experiments this force function is recommended for the easier handling and the agreement with complex experiments.

Mass moment of inertia ball screw

Another value of the ball screw that has to be estimated is the moment of mass inertia θ_{bs}. It is estimated by the moment of mass inertia of a cylinder in respect of its rotational axis.

$$\theta = \frac{1}{2} m r^2 \tag{3.22}$$

The mass of the ball screw m_{bs} is estimated by its length l_{bs}, its diameter d_{bs} and the density of steel ρ_{steel}.

$$m_{\mathrm{bs}} = \pi (\frac{d_{\mathrm{bs}}}{2})^2 l_{\mathrm{bs}} \, \rho_{\mathrm{steel}} \tag{3.23}$$

Table 3.9.: Properties of the ball screw used in the model

Properties of ball screw	
length ball screw	$\mathrm{l_{bs}} = 0.428$ m
diameter ball screw	$\mathrm{d_{bs}} = 0.02$ m
slope ball screw	$\mathrm{p_{bs}} = 0.02$ m
density steel	$\rho_{\mathrm{steel}} = 7900$ kg m^{-3}
mass ball screw	$\mathrm{m_{bs}} = 1.06$ kg
mass moment of inertia ball screw	$\theta_{\mathrm{bs}} = 5.3 * 10^{-6}$ kgm^2
slope angle	$\alpha_{\mathrm{bs}} = 0.31$ rad
friction angle - ideal	$\rho_{\mathrm{ideal}} = 0.05$ rad
friction angle	$\rho = 0.06$ rad
efficiency -ideal	$\eta_{\mathrm{h}} = 0.85$
efficiency	$\eta_{\mathrm{bs}} = 0.72$
friction model "‘stiction"’	$\mathrm{F_{s,bs}} = 290$ N
friction model "‘coulomb"’	$\mathrm{F_{c,bs}} = 29$ N
friction model "‘viscous"’	$\mathrm{F_{v,bs}} = 0$ Ns m^{-1}
friction model "‘velocity"’	$\mathrm{v_{s,bs}} = 0.003$ m s^{-1}
friction model "‘exponential"’	$\delta_{\mathrm{f,bs}} = 1$
friction model, alternative	$\mathrm{k_{bs,v}} = 10$

Carriages

The carriages are defined in the simulation as certain points where friction forces are added. They do not possess any mass or other properties. Only a change of the transmitted force by the friction of the carriage is done.

Also for the carriages the *Stribeck*-model for friction is used. There are four carriages (hip, foot, drive-train at the end of the ball screw and on the end of the cable[they are assumed as one in the model]) in the system, which are tuned with different parameters. An explanation of the way leading to the used friction parameters is explained in chapter 3.2.5. At this place only the summarized parameters are shown in Fig. 3.10.

Table 3.10.: Properties of the carriages in the simulation

Properties of carriages	
friction constant "“stiction"” hip	$\mathrm{F}_{\mathrm{s,h}} = 5\ \mathrm{N}$
friction constant "“coulomb"” hip	$\mathrm{F}_{\mathrm{c,h}} = 4\ \mathrm{N}$
friction constant "“viscous"” hip	$\mathrm{F}_{\mathrm{v,h}} = 5\ \mathrm{Ns\ m}^{-1}$
friction constant "“velocity"” hip	$\mathrm{v}_{\mathrm{s,h}} = 0.001\ \mathrm{m\ s}^{-1}$
friction constant "“exponential"” hip	$\delta_{\mathrm{f,h}} = 1$
friction constant "“stiction"” foot	$\mathrm{F}_{\mathrm{s,f}} = 4.5\ \mathrm{N}$
friction constant "“coulomb"” foot	$\mathrm{F}_{\mathrm{c,f}} = 3.6\ \mathrm{N}$
friction constant "“viscous"” foot	$\mathrm{F}_{\mathrm{v,f}} = 5\ \mathrm{Ns\ m}^{-1}$
friction constant "“velocity"” foot	$\mathrm{v}_{\mathrm{s,f}} = 0.001\ \mathrm{m\ s}^{-1}$
friction constant "“exponential"” foot	$\delta_{\mathrm{f,f}} = 1$
friction constant "“stiction"” drive-train	$\mathrm{F}_{\mathrm{s,dt}} = 5\ \mathrm{N}$
friction constant "“coulomb"”drive-train	$\mathrm{F}_{\mathrm{c,dt}} = 4\ \mathrm{N}$
friction constant "“viscous"”drive-train	$\mathrm{F}_{\mathrm{v,dt}} = 5\ \mathrm{Ns\ m}^{-1}$
friction constant "“velocity"”drive-train	$\mathrm{v}_{\mathrm{s,dt}} = 0.001\ \mathrm{m\ s}^{-1}$
friction constant "“exponential"”drive-train	$\delta_{\mathrm{f,dt}} = 1$

Cable

The cable used in the test-bed is respected in the simulation through a spring with a very high stiffness that only takes effect in one direction (the difference between the position of the carriage and the cable on the pulley must be positive, if negative the force gets zero).

The spring is virtually attached between the position of the carriage x_{bs} and the position of the cable on the pulley and connects the model of the segmented leg and the model of the drive-train. Forces generated through a lengthening of the cable (difference between the positions of carriage and the cable on the pulley) transfer the force from the drive-train to the torque at the leg τ.

$$\tau = r_{\mathrm{p}} \eta_{\mathrm{c}} k_{\mathrm{c}} \left(x_{\mathrm{bs}} - r_{\mathrm{p}} \left(\phi - \arcsin \left(\frac{x_{\mathrm{h},0}}{2\, l_{\mathrm{l}}} \right) \right) \right) \tag{3.24}$$

For this calculation the stiffness k_{c} and the efficiency η_{c} of the cable, the position of the carriage attached to the ball screw x_{bs} and the necessary parameters for calculating the end position of the cable on the pulley (the radius of the pulley r_{p}, the knee angle ϕ the initial position of the hip $x_{\mathrm{h},0}$ and the length of a segment of the leg l_{l}) are necessary.

To calculate the stiffness of the cable some assumptions were made. It is assumed that the stiffness of a cable could be approximated by the tension stiffness of a bar with the same section area A_{c} and a reduced E-modulus $E_{\mathrm{steel,\ red}}$ of the material. The value of 0.75 for the reduction of the E-modulus was chosen because steel in the form of cables inherits a reduced stiffness. The experiments with the test-bed resulted in a similar behavior, the simulation models shows with this parametrization. Therefore, is the value for the reduced stiffness assumed as valid.

$$
\begin{aligned}
A_{\mathrm{c}} &= \pi \left(\frac{d_{\mathrm{c}}}{2}\right)^2 \\
E_{\text{steel, red}} &= 0.75\ E_{\text{steel}} \\
k_{\mathrm{c}} &= A_{\mathrm{c}}\ \frac{E_{\text{steel, red}}}{l_{\mathrm{c}}}
\end{aligned}
\tag{3.25}
$$

As described in chapter 2.1.4 the cable connected to the segmented leg makes it possible to calculate a range for an eigen-frequency for the cable attached to a rigid point while the other end is attached to the segmented leg.

Table 3.11.: Properties of the cable in the model

Properties of cable	
length cable	$\mathrm{l_c} = 0.5\ \mathrm{m}$
diameter cable	$\mathrm{d_c} = 1.5\ \mathrm{mm}$
reduced E-modulus	$\mathrm{E_{steel,\ red}} = 157.5\ \mathrm{kN\ mm^{-2}}$
stiffness cable	$\mathrm{k_c} = 556.65\ \mathrm{kN\ m^{-1}}$
efficiency cable [9]	$\eta_{\mathrm{c}} = 0.9$

3.2.4 Ground model

The ground has an influence on the oscillation when the mass of the foot m_4 is bigger than zero and the motion of the leg includes a flight phase. Impacts of the foot after each hop and the displacement of the ground are the main reason for energy losses.

There are two ground models used in the simulation. The first one contains a spring and a damper in parallel (see Fig. 3.9). Both of them generate a reaction force linear to the displacement Δx_{g} and the velocity $\Delta \dot{x}_{\mathrm{g}}$ of the ground. This displacement is equal to the position of the foot or hip if the position of the foot is lower than zero $x_{\mathrm{f}} < 0$ respectively if the position of the hip is lower than the position of the hip-stop $x_{\mathrm{h}} < x_{\mathrm{hs}}$. Therefore, the ground reaction force is only bigger than zero if this condition is met. A second condition that the ground model must meet is that the ground reaction force must always stay positive. The ground can not pull at the foot or the hip.

$$
\begin{aligned}
F_{\mathrm{GRF}} &= k_{\mathrm{g}}\ \Delta x_{\mathrm{g}} + d_{\mathrm{g}}\ \Delta \dot{x}_{\mathrm{g}} \\
&= k_{\mathrm{g}}\ (x_{\mathrm{f/h,0}} - x_{\mathrm{f/h}}) + d_{\mathrm{g}}\ \dot{x}_{\mathrm{f/h}}
\end{aligned}
\tag{3.26}
$$

This model is used to calculate the reaction force of the hip stop and it shows satisfying results. The parameters k_{g} and d_{g} were tuned by hand in the beginning. They have been changed until the model showed the wished behavior (close to a rigid bed-stop, low oscillations after an impact and fast decay of oscillations).

For the ground beneath the foot shows a different behavior than the hip stop, another model had to be found. This second possibility bases on the ground model used in [31]. A nonlinear spring-damper system generates the ground reaction force opposing the movement of the foot. The two parameters a_g and b_g are slightly adopted values of the ones found in [31]. For the behavior of the second ground model the same conditions are valid as in the first one. The force is only active when the foot goes beneath the zero position and can only produce positive force values.

$$F_{\mathrm{GRF}} = a_g \left|x_g\right|^3 (1 - b_g \dot{x}_g) \tag{3.27}$$

The values for the used ground models are summarized in Fig. 3.12.

Table 3.12.: Properties of the ground models for hip and foot

Properties of ground models	
spring rate ground model 1	$\mathrm{k_g} = 10^6\ \mathrm{N\ m^{-1}}$
damping rate ground model 1	$\mathrm{d_c} = 100\ \mathrm{Ns\ m^{-1}}$
non-linear spring rate ground model 2	$\mathrm{a_g} = 0.25\ 10^9\ \mathrm{N\ m^{-3}}$
damping rate ground model 2	$\mathrm{b_g} = 3\ \mathrm{s\ m^{-1}}$

3.2.5 Friction model

In different places of the test-bed friction forces influence the dynamics of the whole system. Friction forces and torques always act against the direction of movement. The major points, where friction forces effect the system, are the bearings. Existing bearings can be divided in rotational and translational bearings.

The calculation of friction torques in the roller bearings has been discussed in chapter 3.2.2. The outcome was to neglect the friction torque in the roller bearings for the low resulting values.

For the friction force in the translational bearings less information is available. The producer suggests to include a constant force $F_{\text{carriage, trans}} = 10\mathrm{N}$ in the opposite direction of movement [5]. This force results from the contact of the sealing of the bearing against its rail. The actual force is lower than that and has also to respect coulomb- and viscous friction. Experiments with a stiction force $F_{\text{carriage, trans}} = 10\mathrm{N}$ did not result in a behavior observed in the test-bed.

There are different models to respect friction forces F_{fr} in simulations. One way is to add a constant amount of friction force F_1 always in the opposite direction of the movement x at the point of the carriages.

$$F_{\mathrm{fric}} = -\mathrm{sign}(\dot{x}) F_1 \tag{3.28}$$

This model contains only coulomb friction. Possible parts of stiction and velocity dependent friction are neglected. One problem with this type of friction modeling is the numerical chattering in the simulation gained through this method for the *signum*-function is unsteady. Solvable is this problem by replacing the *signum*-function.

$$\mathrm{sign}(\dot{x}) \approx \tanh(C\ \dot{x}) \tag{3.29}$$

For a high value of C the function approximates the signum function. For most friction models in the simulation the parameter is set to $C = 800$.

For a noncontinuous force leads to problems in the simulation, a method is chosen to consider friction forces in a continuous manner. An approach after *Stribeck* is used [18][p. 50]. The approach considers stiction, coulomb- and viscous-friction. A resulting force depends on the velocity $\dot{x}$, the stribeck-velocity v_s, the stribeck exponential shape constant δ_s. In the beginning the values for $v_s = 0.001$m/s and $\delta_s = 1$ were chosen similar to [18][p. 50]. The characteristic forces F_c (coulomb), F_v (viscous) and F_s (stiction) are chosen to gain realistic behavior. Also the approach for replacing the *signum*-function is used.

$$\begin{aligned} F_{\mathrm{fr}} =& F_{\mathrm{Stribeck}} \ \tanh(800\,\dot{x}) + (F_v \dot{x}) \\ F_{\mathrm{Stribeck}} =& F_c + (F_s - F_c) \exp\left(-\left|\frac{\dot{x}}{v_s}\right|^{\delta_s}\right) \end{aligned} \tag{3.30}$$

The relationship between the velocity and the resulting friction force at the linear bearing of the hip is shown in fig.3.14. The behavior of the friction could be adjusted easily to other places in the test-bed were friction force are existent.

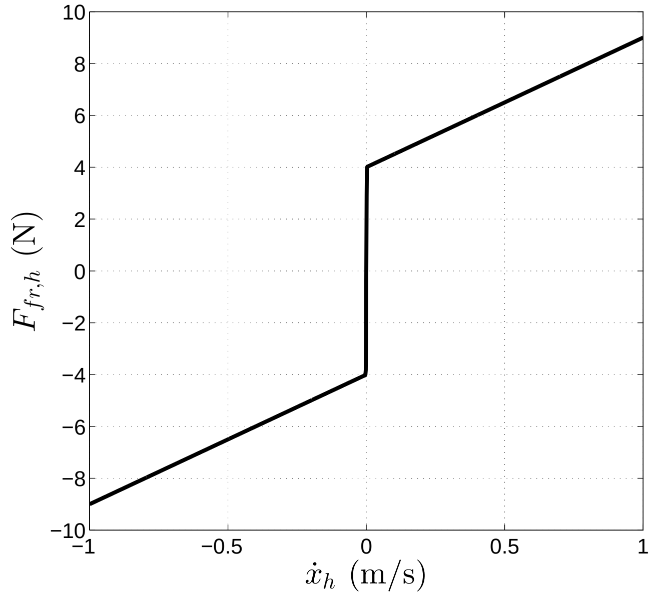

Figure 3.14.: [SIM] The relationship between the velocity of the bearing and the friction force at the bearing of the hip $F_{\mathrm{fr,h}}$. The parameters for the calculation of the friction force are $v_s = 0.001$ m/s, $\delta_s = 1$, $F_{\mathrm{c,h}} = 4$ N, $F_{\mathrm{s,h}} = 5$ N, $F_{\mathrm{v,h}} = 5$ Ns/m.

Different tests for the linear bearings in the test-bed have been performed to adjust each model properly. The test for the adjustment of the friction in the ball screw has been discussed in chapter 3.2.3. The development of the parameters for the carriages of foot and hip is shown here. To determine the parameters of the friction in the hip- and foot-bearing, an experiment in the test-bed was performed. The stretched leg was lifted up to a position near $x_h = 0.5$ m. After that the leg was released and the motion of this fall was recorded. The same experiment has been performed with the simulation model. For only friction forces of the bearings oppose the falling

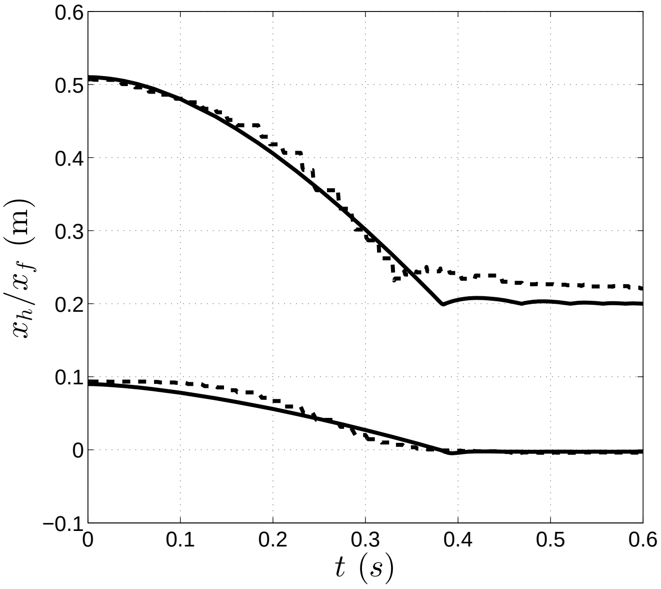

Figure 3.15.: [SIM+EXP] The comparison between the fall of the segmented leg in the simulation (solid line) and in an experiment (dashed line) from a certain release height $x_{\mathrm{h},0} \approx 0.5$ m. The parameters for the calculation of the friction force are $v_{\mathrm{s,h/f}} = 0.001$ m/s, $\delta_{\mathrm{s,h/f}} = 1$, $F_{\mathrm{c,h}} = 4$ N, $F_{\mathrm{c,f}} = 3.6$ N, $F_{\mathrm{s,h}} = 5$ N, $F_{\mathrm{s,f}} = 4$ N,$F_{\mathrm{v,h/f}} = 5$ Ns/m.

motion, the effect of them can be quantified. Values for both friction models have been adjusted until the behavior comes close to each other. The gained values are shown in Fig. 3.10.

4 Control

After the development of a theory to control a segmented leg in the fashion of a single mass oscillator and the work on the test-bed, a control strategy shall be developed.

This strategy bases on the theoretical derived laws for generating a desired torque at the knee in combination with measures that are necessary through limitations or properties of the test-bed. Especially the interaction between drive-train and the segmented leg is a matter, which has not been mentioned before. Laws for calculating desired torque values with the ideal segmented leg without the consideration of a drive-train could show some weaknesses through the coupling of both sub-systems. The goal is to enable the test-bed to perform the theoretically possible hopping motions.

If nothing else is mentioned the maximal current of the motor is set to $i_{\mathrm{M,max}} = 10.5$ A, the nominal current given by the producer.

4.1 Force control - feed forward control

The basic idea of the force control approach in the manner of a feed forward control is that the desired force is given to the motor without the consideration of the actual force at the force sensor. Only properties of the drive-train are considered to calculate a desired current from the desired force.

The desired force F_{des} is calculated from eq. 2.47. This desired torque at the knee is transformed to a force at the end of the drive-train through the radius of the pulley r_{p} and the efficiency of the cable η_{c}.

$$F_{\mathrm{des}} = \frac{\tau_{\mathrm{des}}}{r_{\mathrm{p}}\eta_{\mathrm{c}}} \tag{4.1}$$

With the desired force F_{des}, the transmission ratios of the motor-transmission i_{T} and the ball screw i_{bs} and the efficiencies of these parts η_{T} and η_{bs} a desired current i_{M} can be calculated.

$$i_{\mathrm{M}} = F_{\mathrm{des}} \frac{1}{i_{\mathrm{bs}} i_{\mathrm{T}} \eta_{\mathrm{bs}} \eta_{\mathrm{T}} k_{\mathrm{M}}} \tag{4.2}$$

First experiments with this approach show characteristics of this control scheme.

The first comparison is made between the simulation of the segmented leg driven by an ideal torque and the segmented leg with an attached drive-train. Friction forces and the loss characteristics of the ball screw are neglected at this point.

As shown in fig.4.1 the segmented leg can meet the expectations and perform a motion similar to the single mass oscillator. This movement of the system without drive-train sets the goal to

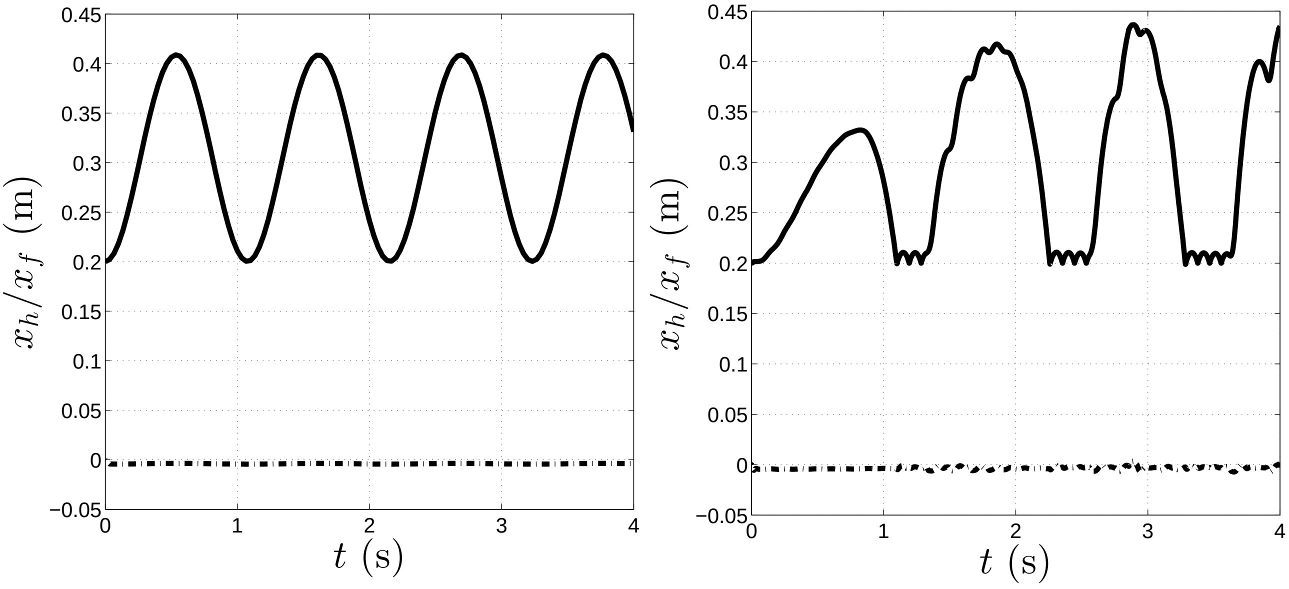

(a) **(b)**

Figure 4.1.: [SIM] Comparison between the simulation of the multi-body system without (a) and with (b) an attached drive-train. The multi-body system without an attached drive-train acts like a single mass oscillator, as shown before. Both systems are set to the same desired torque at the knee. k_v is set to meet the condition of $\omega_\text{set} = 6$ rad/s. Shown are the time dependent positions of hip (solid line) and foot (dashed line). All friction forces in the system are turned to zero. The mass distribution is chosen to be like in the test-bed. The solver used is ODE23.

reach. The segmented leg with the attached drive-train reacts to the given current values with an unstable oscillation. With an open feed forward control neither the desired frequency nor the amplitude of the oscillation can be reached. To control the system only with a feed-forward control approach is not feasible.

In this first experiment friction forces were neglected. If the realistic friction forces are applied to the simulation model of the segmented leg, no oscillation with the parameters, used so far, is possible. The friction acts against the virtual spring and lets the leg stuck at a certain position when the friction forces and the force resulting from the knee torque are balanced (see Fig. 4.2). For the goal of this thesis is the realization of hopping motions, the focus will lie on methods making this possible. The realization of certain frequencies and amplitudes of oscillation will not be a part of the further discussions.

The effect of the friction of the bearings is best shown through some simulations performed with the segmented leg without drive-train. Without friction in the bearings it can behave like a single mass oscillator. The friction changes the behavior very strong. A hopping motion is set through the choice of eq. 2.42 and a desired hopping height of $\Delta h = 0.3$ m. The 'take-off' of the leg occurs before reaching the rest-length of the spring.

The reason for this is that the knee stop prevents a further extension of the leg. The angle of the knee stop is tuned to the possible knee angle in the test-bed. Experiment and simulation are better comparable. In all figures the position of a fully stretched leg will be marked by a blue, solid line.

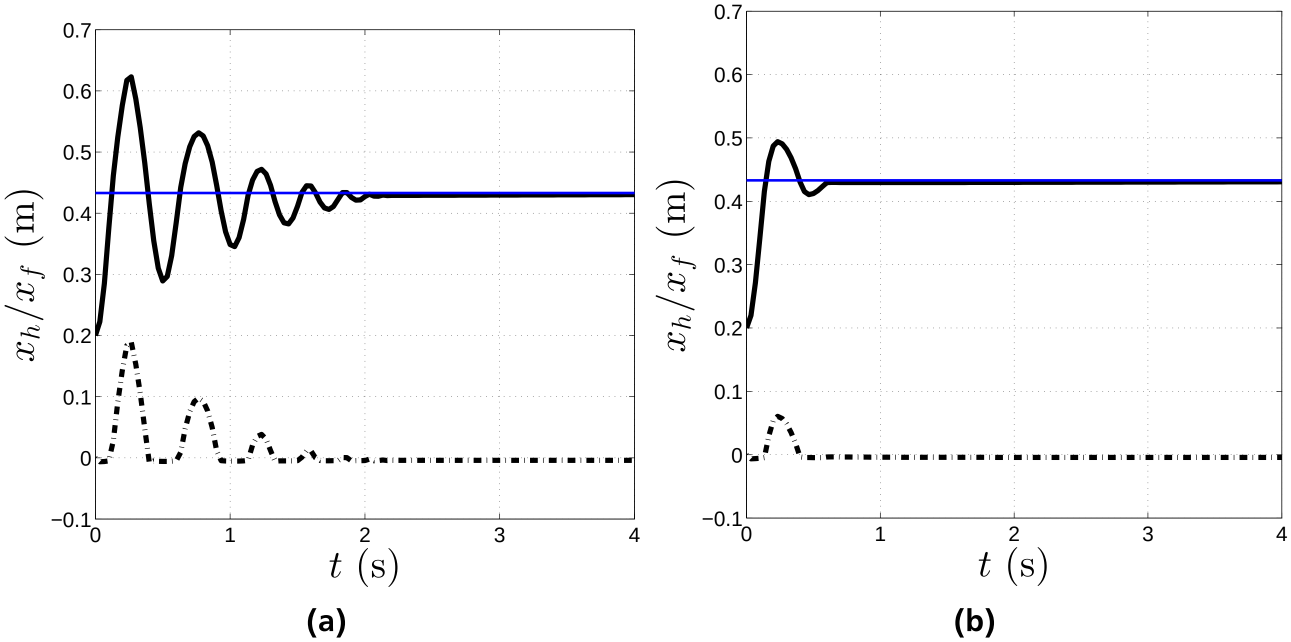

(a)

(b)

Figure 4.2.: [SIM] Comparison between the simulation of the multi-body system without (a) and with (b) friction in the bearings of hip and foot. Both systems are set to the same desired torque at the knee. k_v is set to meet the condition of $\Delta h = 0.3$ m. Shown are the time dependent positions of hip (solid line) and foot (dashed line). The vertical solid line shows the position of the stretched leg/'take-off'(the leg hits the knee stop). The mass distribution is chosen to be like in the test-bed. The solver used is ODE23.

In both systems losses through the ground occur. Therefore, also the system with a friction of zero in the bearings results in a decreasing motion (see Fig. 4.2(a)). The losses in the system with included friction forces in the bearing of hip and foot are bigger (see Fig. 4.2(b)). The hip reaches a far smaller apex height and the movement ceases after one hop. Both systems do not reach the desired hopping height of $l_0 + \Delta h$.

The assumptions made to develop the law in eq. 2.48 are not the same as in the complex system. The change of height after take-off Δh, does not serve anymore as a parameter that determines the exact hopping height, but as a tuning parameter. In the presence of uncertain losses by bearings and ground it is expected that an exact determination of a hopping height through simple models is impossible. The choice of Δh sets a certain amount of energy added to the system. In the case of an ideal model free of losses the additional energy would be transformed in potential energy and, therefore, into a certain hopping height $l_0 + \Delta h$. In the presence of losses, this amount of energy is used to counterbalance the losses. The remaining energy sets the hopping height. For its simplicity, this law is used for first experiments.

There are at least three things in which the real test-bed will differ from the ideal dynamic model shown in chapter 2.2.2.

First, there occur losses through friction and damping in all bearings (bearings at the hip, the foot and in the drive-train). Second, the impact and deformation of the ground causes also losses, which were not respected before. Third, the attachment of a drive-train will influence the behavior of the segmented leg. To realize a stable hopping motion all these influences have to be respected and counter-measures have to be found.

4.1.1 Feed forward control - bang-bang control

The multi-body system is actuated with the same torque law (eq. 2.47) as before . The calculation of the value for k_v is changed to the law derived in chapter 2.2.1 through eq. 2.42. The tuning of k_v is realized by Δh. The idea behind this control is to vary the stiffness k_v during the different phases of the hopping motion. While the motion is directed upward, the stiffness is set to $k_v \neq 0$. At a certain position of the hip x_{h+} the stiffness is set to zero $k_v = 0$. The segmented leg can fall free for the torque at the knee becomes also zero. When the hip reaches a certain height above the stop of the hip x_{x-}, the stiffness k_v is set again to the value bigger than zero. A resulting knee torque stops the fall of the structure and initializes another hop. Shown is the scheme of the idea in Fig. 4.3.

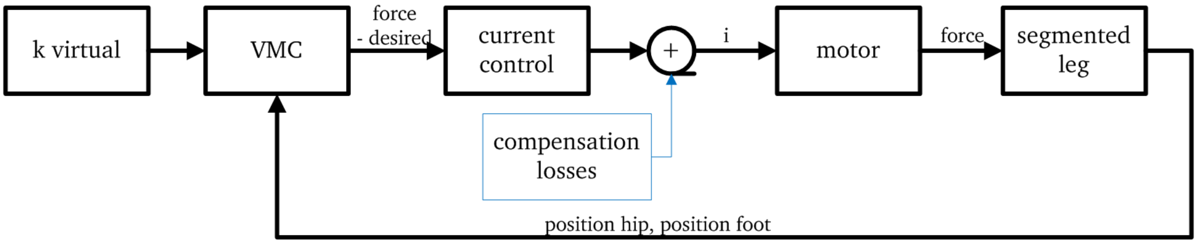

Figure 4.3.: Control block diagram of the bang-bang control approach. The darker boxes show the basic (feedforward) control mechanism for a SLIP based virtual model control (VMC). The lighter loss compensation box is an optional mechanism that enhances the performance of the real system. It contains the additional current values i_{M-} and i_{M+} compensating the effects of the ball screw (see chapter 4.1.1).

As to see in Fig. 4.2 a continuous virtual spring rate bigger than zero results in a decreasing oscillation. The system aspires to the point where the force by the virtual spring and the weight force of the leg are in equilibrium. The friction force and the losses in the ground reduce the amount of energy stored in the system. A non-continuous spring rate injects new energy in every cycle of the movement and could counterbalance the losses.

Comparison of hopping motions with or without included friction forces

In fig. 4.4 a comparison between the system with and without the influence of friction forces is shown. No drive-train is attached to the segmented leg. Only the influence of the friction in the bearings of hip and foot is discussed. The switching points of the control are set to $x_{h+} = 0.45$ m and to $x_{h-} = 0.22$ m. These values showed the wished behavior. In both cases a stable hopping motion is feasible. The friction influences the reached height of the hopping, the frequency of the movement and also the shape of the motion. The influence of the friction disturbs the symmetry of the movement. When the hip moves down it takes longer than the upward movement. During

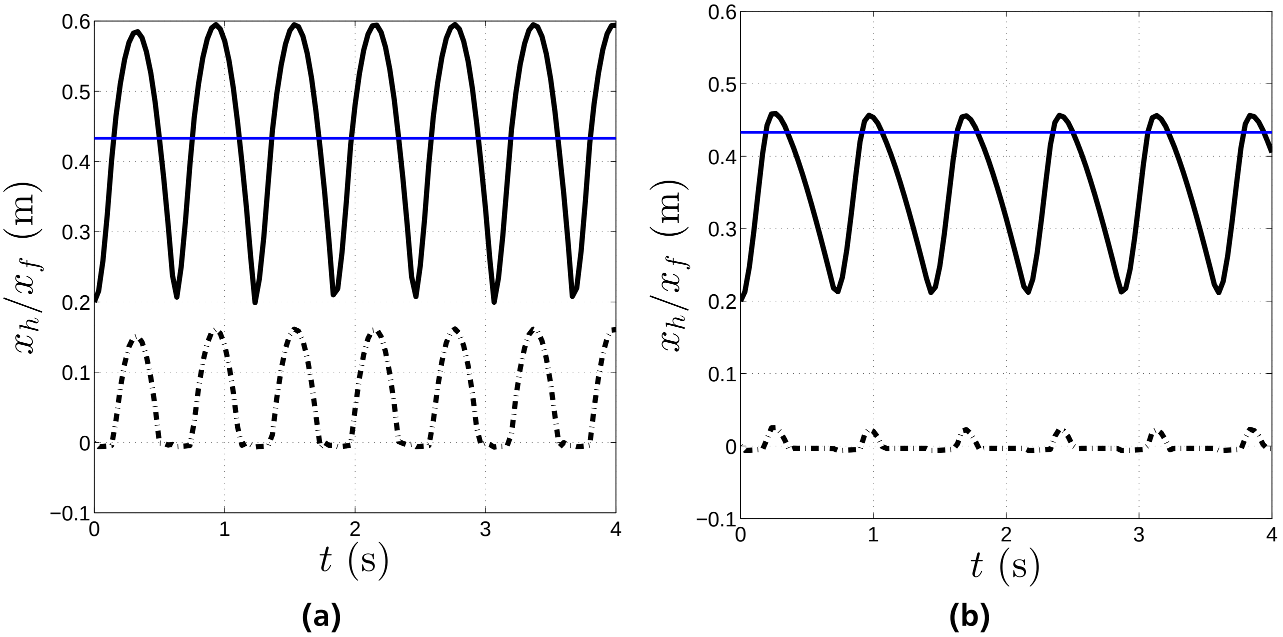

Figure 4.4.: [SIM] Comparison of hopping motions of the multi-body system with free fall and without (a) or with (b) the effect of friction at the linear bearings at the hip and the foot. Shown are the plots of the position of hip and foot. The vertical solid line shows the position of the stretched leg/'take-off'(the leg hits the knee stop). $\Delta h = 0.15$ m in this setup. The switching points are set to $x_{\text{h+}} = 0.45$ m and to $x_{\text{h-}} = 0.22$ m. Both systems can produce stable hopping motions. The solver used is ODE23.

the fall only friction forces oppose the motion. When the hip is accelerated upward, the opposing friction force is compensated through the torque at the knee. The fall is purely passive.

Even the model of the segmented leg is not that far away from the ideal dynamic model developed in chapter 2.2.2, the resulting movement patterns are very different due to the perturbations through the bearings. The approximation of a SLIP model through the test-bed is made difficult by this fact.

Comparison of multi-body system with or without the drive-train

In fig. 4.5 results gained with the multi-body system with and without the drive-train are compared. In both models friction forces are neglected. Without further measures a stable hopping motion with the drive-train is not possible.

The oscillation of the segmented leg is increasing due to the drive-train. A reason for the increasing of the oscillation is that the motor drives in the negative direction, further than its initial position.

When a new cycle of hopping begins, the motor and therefore, the attached carriages on the drive-train which hold the cable, can accelerate over a larger distance and inject more energy in the system. The energy and also the hopping height of the segmented leg increases.

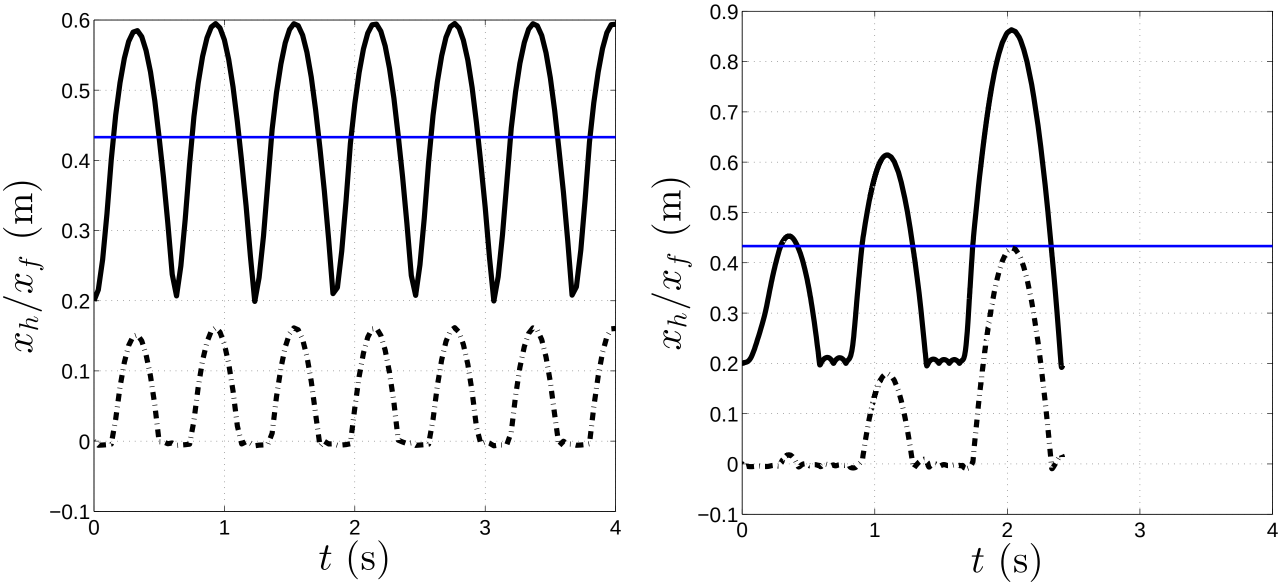

(a) **(b)**

Figure 4.5.: [SIM] Comparison between the simulation of the multibody-system without (a) and with (b) attached drive-train. Friction forces are neglected. The bang-bang control method is used with $\Delta h = 0.15$ m. The switching points are set to $x_{\text{h+}} = 0.45$ m and to $x_{\text{h-}} = 0.22$ m. Shown are the time dependent positions of the hip and the foot. The vertical solid line shows the position of the stretched leg. The solver used in the simulation is ODE23.

In reality this effect is counterbalanced by the friction in the drive-train. The weight of the leg could not move the drive-train on its own. There is always a amount of negative motor current necessary, to move the drive-train back to its initial position.

Segmented leg with drive-train and inclusion of friction forces

When friction forces at all places of the drive-train are respected, the parameter Δh has to be increased to overcome the opposing forces.

Also further measures have to be taken, to consider the effects of the drive-train. If the loss model of the ball screw is respected, the leg is not able to fall down and to move the drive-train in the opposite direction. The opposing force in the ball screw-transmission-motor combination is higher than the force resulting from the weight of the segmented leg pulling at the cable.

Therefore, an additional current $i_{\text{M-}} = -2.5$ A has to be added to the motor control during the fall of the leg. This current serves only to counteract the effects of friction in the drive-train. It is also switched in the manner of the switching of the stiffness k_{v}. During the upward motion also a current $i_{\text{M+}} = 1$ A is added to counterbalance the friction during this part of the movement. The values of current for this friction compensation were developed on the test-bed and chosen due to their performance. In the block diagrams this mechanism is symbolized by the "‘compensation losses"’ box.

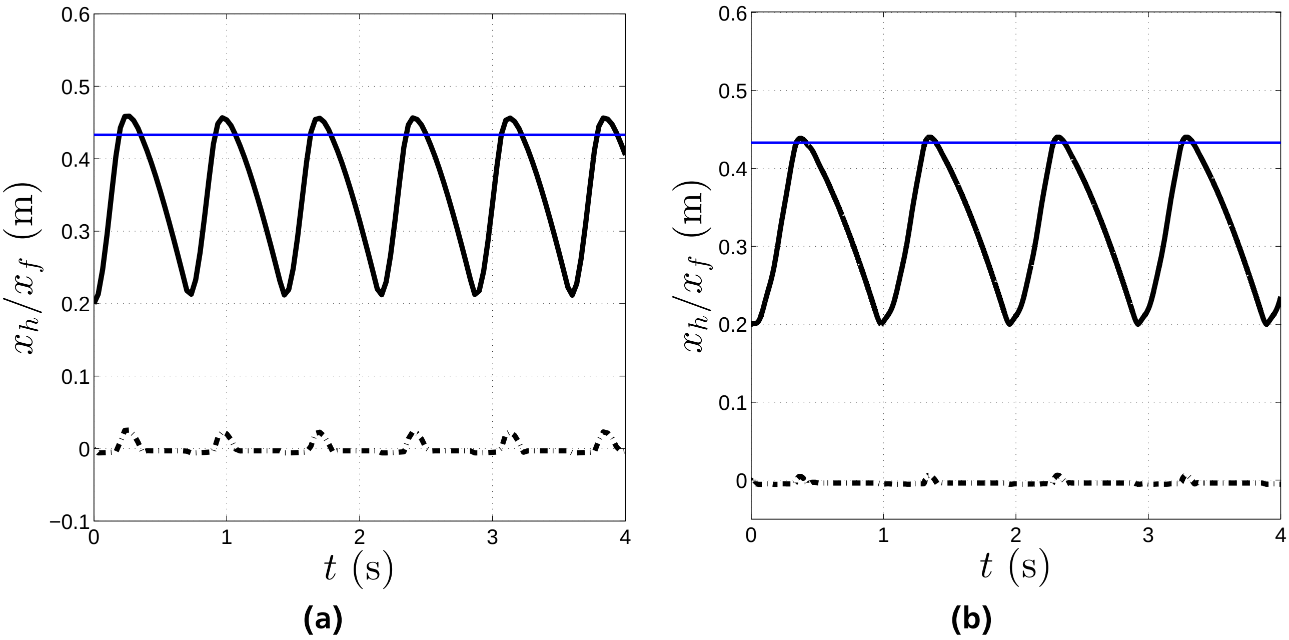

Figure 4.6.: [SIM] Comparison between the simulation of the multi-body system with drive-train and the consideration of friction forces (b) and the simulation of the segmented leg without drive-train but the same parameters for the friction models (a). The method of free fall is used with $\Delta h = 0.15$ m. The switching points are set to $x_{\mathrm{h+}} = 0.45$ m and to $x_{\mathrm{h-}} = 0.22$ m. Shown are the time dependent positions of the hip and the foot. The solver used in the simulation is ODE23.

As to see in Fig. 4.6 the apex point of the movement and also the hopping frequency is further reduced. Nonetheless, a stable hopping motion is possible. The next step is to implement the developed control strategy on the test-bed.

Comparison of simulation and experiment

The control approach combining feed forward control and the bang-bang approach of stiffness manipulation is used on the test bed to test its usability. In fig. 4.7 the results are shown.

A stable hopping motion is the result in the simulation and in the experiment. At one point the experimental movement is disturbed but reaches again a hopping motion after this event. The hopping height is comparable and also the velocity of the upward motion. In the experiment the fall of the hip to the initial position takes a longer time than predicted in the simulation. Because of this longer duration the frequency of the hopping motion is reduced. Reasons for this slower movement lie probably in an incorrect adjusted value for the friction compensation current $i_{\mathrm{M-}}$ and the realization of the desired current course by the internal current control of the motor.

Summary bang-bang control

The method of the feed-forward control in combination with a bang-bang approach for adjusting the virtual stiffness k_{v} is able to produce hopping motions in simulation and on the test-bed.

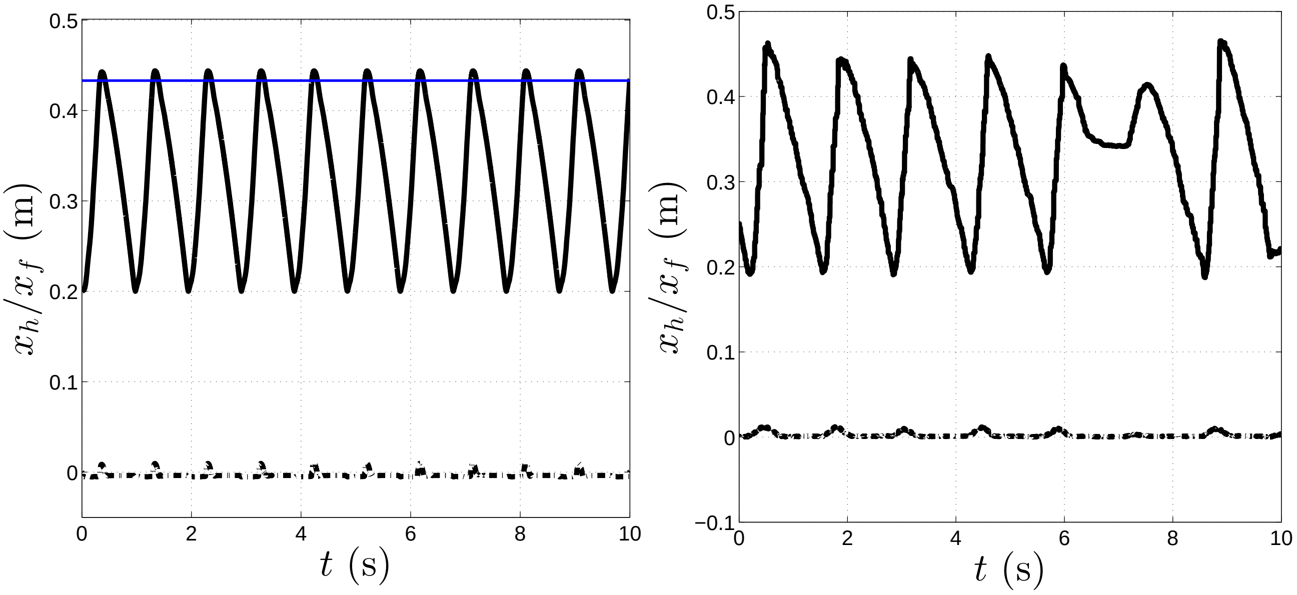

(a) **(b)**

Figure 4.7.: [SIM+EXP] Comparison between the simulation of the multi-body system with drive-train and included friction effects (a) and an experiment with the same control parameters with the test-bed (b). The method bang-bang control is used with $\Delta h = 0.3$ m, $x_{\text{h-}} = 0.22$ m and $x_{\text{h+}} = 0.45$ m. The last ten seconds of the experiment are shown. The solver used in the simulation is ODE23.

One property of the bang-bang control approach is the discrete nature of the control. The function for the stiffness is a periodic step-function. Motor currents and also forces are changing very abrupt. This behavior is not biologically inspired and is also not desirable for the actuator. For this reason another method for the control of the test-bed through an adjustment of the virtual spring stiffness k_{v} is developed.

4.1.2 Feed forward control - continuous change of spring stiffness

In [17] a method called "‘constant energy supply"’ is suggested to control the test-bed MARCO Hopper. It is a possible energy management technique to produce stable hopping motions even if the movement is confronted with perturbations or uncertain underground. In this method the virtual spring stiffness is changed continuously over the leg length.

In the phase after midstance (the lowest point of the movement, the ground reaction force is maximal) the stiffness of the virtual spring is raised to inject a certain amount of energy ΔW in the system during every hop. The additional stiffness Δk is calculated by:

$$\Delta k = 6\ \Delta W \frac{x_{\text{h}} - x_{\text{f}} - x_0}{(l_0 - x_0)^3} \tag{4.3}$$

l_0 describes the rest length of the virtual spring. Experiments in [17] show that a certain amount of energy leads to a hopping height, where losses and additional energy are in equilibrium.

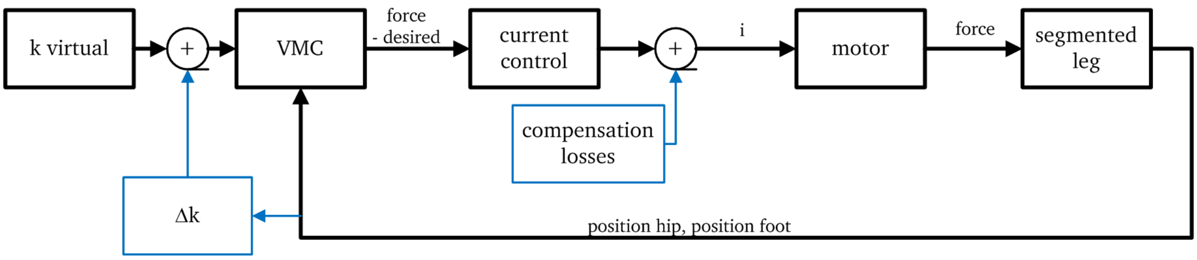

Figure 4.8.: Control block diagram of the continuous change of spring stiffness approach. As before the black boxes show the basic feed-forward mechanism of the system. An additional stiffness Δk is added to the system dependent on the positions of hip and foot. The compensation of losses in the real system can enhance the performance of the system. It contains the additional current values $i_{\text{M-}}$ and $i_{\text{M+}}$ compensating the effects of the ball screw (see chapter 4.1.1).

Now the virtual spring stiffness contains two parts. A basic stiffness k_0 and the additional stiffness Δk inject a certain amount of energy ΔW during each hop in the system. Δk is only active during the upward movement (from 'midstance' to 'take-off'). The switching between the stiffness calculation laws happens again at the points $x_{\text{h+}} = 0.45$ m and $x_{\text{h-}} = 0.22$ m.

$$k_{\text{v}} = k_0 + \Delta k \tag{4.4}$$

The basic stiffness k_0 will be set to the value, which is necessary to reach the rest length of the spring (see eq. 2.9).

$$k_0 = \frac{2mg}{l_0 - x_0} \tag{4.5}$$

The amount of energy added to the system ΔW compensates the losses by friction and the ground. It is adjusted during the experiments to values that can generate stable hopping motions.

In this chapter it is shown that the multi-body system can perform hopping motions with the concept of a continuous change of the spring stiffness. The chosen control strategy is the feed forward approach as used before for the bang-bang calculation of the stiffness. The current i_{M} set to the motor is calculated like in eq. 4.8. A desired force F_{des} is calculated with eq. 2.47.

For testing the control strategy, the same procedure shall be used as for the test of the bang-bang approach. First, the strategy will be tested on the multi-body model without drive-train and the results gained under the influence of friction forces are shown. After that the suitability for the model with drive-train is tested. Last, the strategy will be used to control the test-bed.

Comparison of hopping motions with or without included friction forces

The differences in the motion deriving between a model with and without the influence of friction forces are shown. In this experiment the drive-train is not included. The stiffness of the virtual spring is set to a value of k_{v}, which is necessary to reach the rest length. ΔW is varied. A comparison between the behavior of the system with and without the influence of friction forces is shown in Fig. 4.9. A hopping motion is feasible only for the system without the influence of friction. The opposing force of the friction lets the oscillation cease. At some point the force

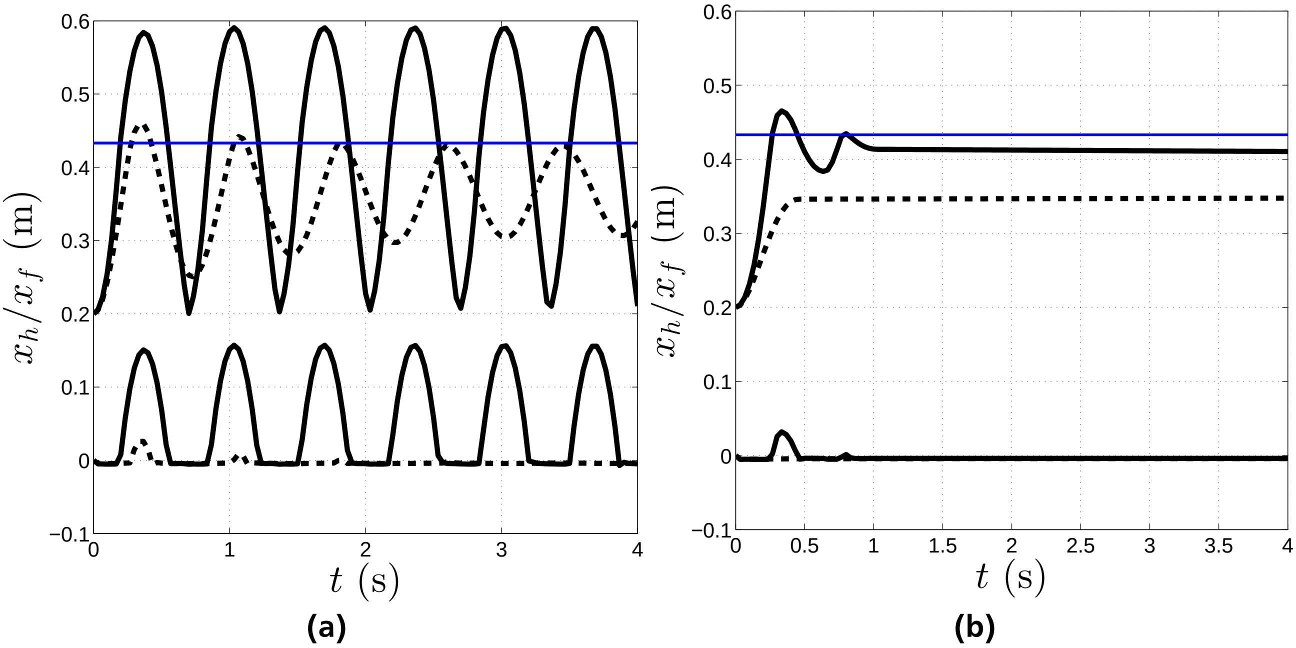

Figure 4.9.: [SIM] Comparison of hopping motions of the multi-body system with a continuous change of spring stiffness during the upward movement. In (a) the friction in the bearings have been turned to zero. In (b) realistic friction forces act in the bearings. The switching points are set to $x_{\text{h+}} = 0.45$ m and to $x_{\text{h-}} = 0.22$ m. The solid black lines show the behavior with a $\Delta W = 0$ J, while the dashed black lines show the behavior with $\Delta W = 3$ J. A stable hopping motion is producable in the system without friction. The friction lets the oscillations decease. The solver used is ODE23.

generated by the motor, the friction force and the weight force of the leg are in balance and the motion stops. Therefore, an implementation on the model with drive-train is not promising.

Through the method with the bang-bang adjustment of the virtual stiffness, the effects of the opposing friction force has been bypassed. During the downward movement no force is generated by the motor. The only force opposing the weight is the friction force. So the movement can not stuck if the weight force is higher than the stiction and the movement is not hindered by the drive-train. This method shall also be be applied to the continuous change of the spring stiffness.

4.1.3 Feed forward control - bang-bang control and continuous change of the spring stiffness

The idea is to combine both, bang bang control, for its performance in the downward movement, and the continuous change of the spring stiffness, for its smother motion upwards. At this point the idea of [17] is changed. In the work of *Kalveram* the spring-rate k is never turned to zero. Due to the properties of the drive-train of MARCO II this measure seems necessary.

The switching positions are kept at $x_{\text{h+}} = 0.45$ m and $x_{\text{h-}} = 0.22$ m. At this point the approach should be presented in a closed form. During the development some parameters and assumptions have been changed a lot. This closed sequence for the control approach makes it easier to follow the control idea. The principle is also shown in Fig. 4.8.

The knee torque τ is calculated to gain the behavior of a single mass oscillator with a segmented leg.

$$\tau = 2\cos\left(\frac{\phi}{2}\right) l_1 \left(\frac{k_v(l_0 - x_h + x_f) - mg}{m}\left(m_1 + \frac{3}{4}m_2 + \frac{1}{4}m_3\right) + \left(m_1 + m_2 + \frac{m_3}{2}\right) g\right) \tag{4.6}$$

This torque is used to calculate a desired force F_{des} attacking the end of the cable respectively the end of the drive-train. At this point the force can be measured. Therefore, it serves as a control value for a possible force-control approach. The desired torque τ_{des} derives from the equation above and the adjustment of the virtual spring stiffness k_v.

$$F_{\mathrm{des}} = \frac{\tau_{\mathrm{des}}}{r_p \eta_c} \tag{4.7}$$

The parameters of the drive-train make it possible to calculate a desired current of the motor to gain the desired force.

$$i_M = F_{\mathrm{des}} \frac{1}{i_{bs} i_T \eta_{bs} \eta_T k_M} \tag{4.8}$$

The motor is presented with this current (on the test-bed the motor controller is presented with this desired current, errors resulting from the internal control of the motor setting this current downgrade the performance).

To manipulate the motion, a certain value for k_v is calculated:

$$k_v = k_0 + \Delta k \tag{4.9}$$

The basic stiffness k_0 is set to reach the rest length of the spring in a system where friction is neglected.

$$k_0 = \frac{2mg}{l_0 - x_0} \tag{4.10}$$

The additional stiffness Δk is changed over the position of the leg and adds energy in a smooth way:

$$\Delta k = 6\,\Delta W \frac{x_h - x_f - x_0}{(l_0 - x_0)^3} \tag{4.11}$$

The bang-bang part of the approach changes k_v between $k_v = 0$ and $k_v = k_0 + \Delta k$, dependent on the position of the hip and the direction of movement. The goal is to let the leg fall free to counterbalance friction effects of the bearings of hip and foot. During k_v is set to zero the motor current is set to certain negative value $i_{M\text{-}}$ to move the drive-train and to counterbalance the effects of friction and damping in the drive-train.

If this method is used, the motion in Fig. 4.10 occurs. The approach is tested on the simulation model without drive-train (a) and the model with an attached drive-train (b). In the simulation of the segmented leg driven by an ideal torque, the torque is set to zero during the fall of the leg.

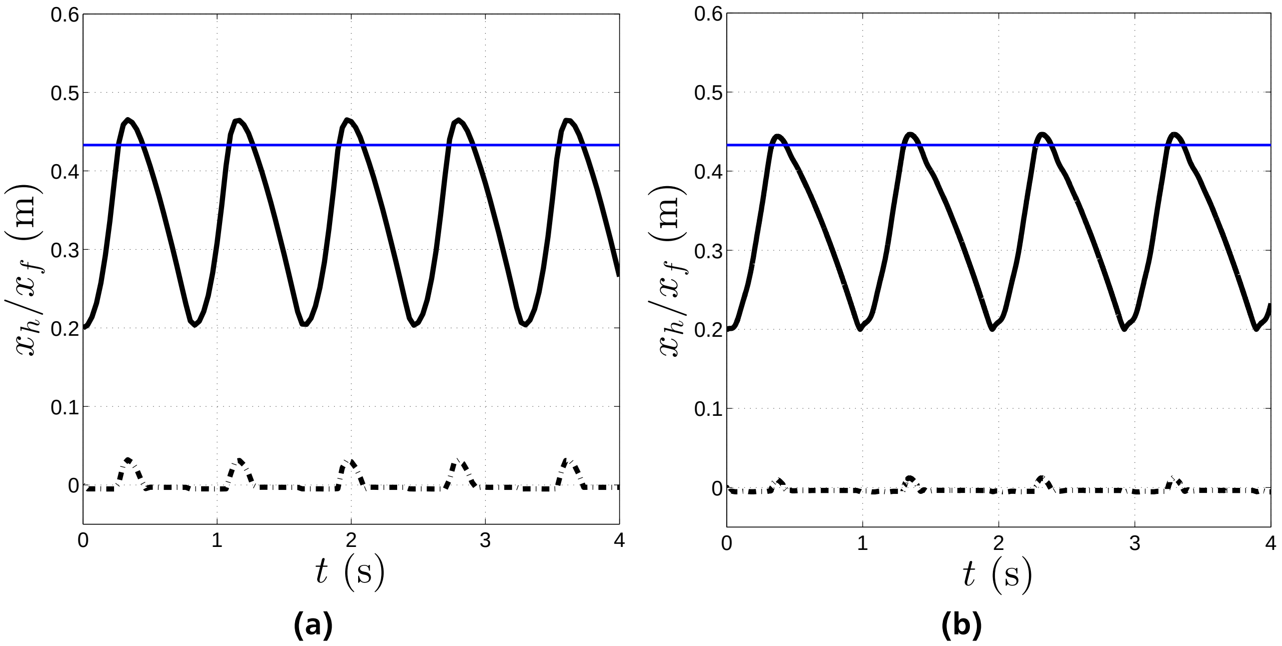

Figure 4.10.: [SIM] Comparison between the multi-body system with (b) and without (a) an attached drive-train. Both simulations were performed under the influence of friction forces. The approach to control the movement is a combination of constant energy supply with $\Delta W = 3$ J and free fall during the downward motion. A solid vertical line marks the position of the complete stretched leg. The solver used in the simulation is ODE23.

Both systems are able to perform stable hopping motions. The system without the drive-train describes the ideal movement with the control approach if it was possible to actuate the knee with an ideal torque source. In the system with drive-train a lot of the used energy serves to overcome the losses of the drive-train. Also the torque at the knee is not the ideal torque at all times, due to the inertia of the drive train, the losses in it and the elasticity of the cable. Therefore, the reached hopping height is smaller than in the ideal model.

Implementation on the test-bed

The developed control is implemented on the test-bed. Results are shown in Fig. 4.11. Like in all experiments before the hopping height in experiment and simulation is comparable. The frequency of the hopping motion in the simulation is higher. The reason for this phenomenon is the slower fall down of the leg in the experimental setup. As to see in Fig. 4.11 (b) a stable hopping motion is only possible over two repeats. There were some problems with the power source of the test-bed during the execution of this experiment. The available current fell down to half of the desired current. It is assumed that a stable motion is possible if the power source does not limit the current.

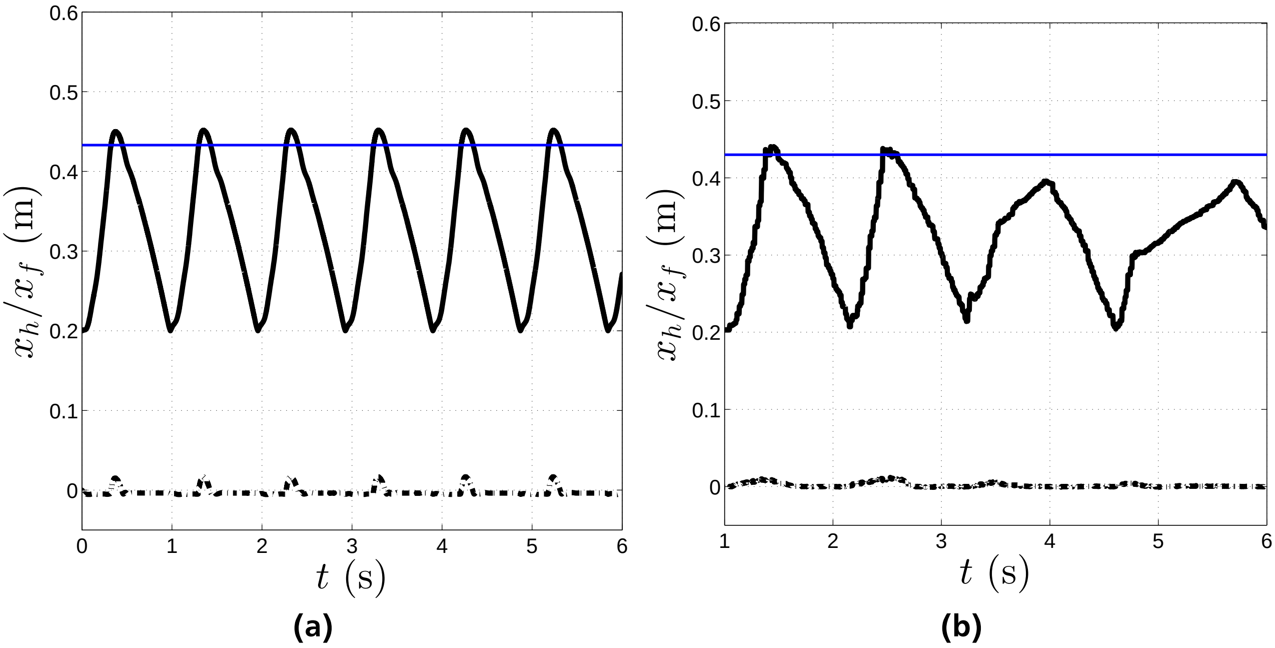

Figure 4.11.: [SIM+EXP] Comparison of the simulated test-bed with attached drive-train (a) and the real test-bed (b). The approach to control the movement is a combination of constant energy supply with $\Delta W = 5$ J and free fall during the downward motion. A solid vertical line marks the position of the complete stretched leg. The solver used in the simulation is ODE23.

Summary feed forward control

It has been shown that with a model based feed forward control approach a hopping motion of the segmented leg in simulation and experiment is feasible. It is not necessary to measure process values of the system, but the positions of the hip and the foot, to realize the control approach. Important parameter settings of the experiments are summarized in Fig. 4.1.

The most promising approach is the combination of the bang-bang control with the continuous change of the spring rate over the leg length. So far the hopping height was small. The performance is limited by the available current of the motor. The question is if an overlie of a force-control can enhance the performance of the system.

Table 4.1.: Parameters of the experiments with bang-bang control and continuous change of the stiffness

parameters - feed forward	
switching height 1	$x_{h+} = 0.45$ m
switching height 2	$x_{h-} = 0.22$ m
angle knee stop	$\phi_{max} = 120$ °
maximum current of the motor	$i_{M,max} = 10.5$ A

4.1.4 Feed forward control + PID - bang-bang control and continuous change of spring stiffness

To gain a better performance, the feed-forward control is combined with a PID-controller (shown is the principle in Fig. 4.12). Its parameter settings depend on the force error. The overlain controller also influences the current signal of the motor. Within this experiments the limit of the motor current is neglected. The primary goal is to find optimized control parameters.

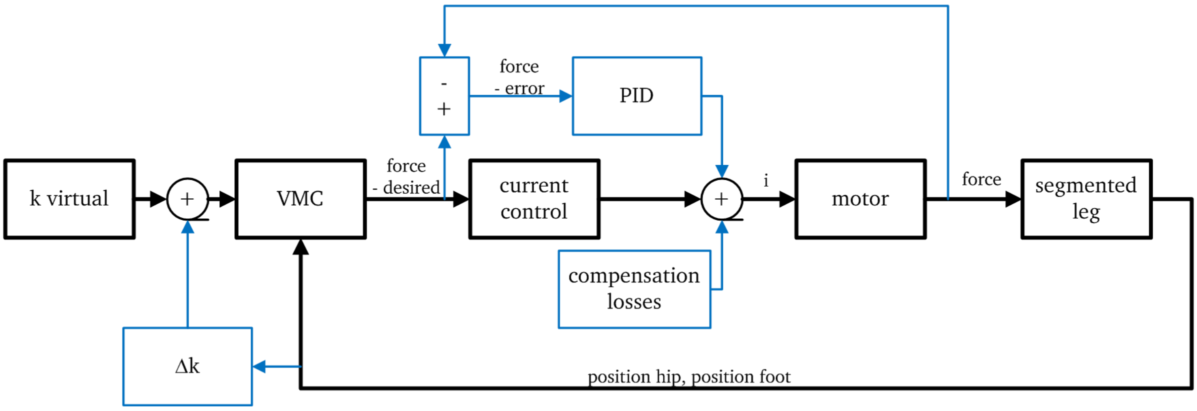

Figure 4.12.: Control block diagram of the continuous change of spring stiffness approach with an additional PID-force-control part. As before the darker boxes show the basic feed-forward mechanism of the system. An additional stiffness Δk is added to the system dependent on the positions of hip and foot. The error resulting from the desired- and actual force is used to control the system with a PID-controller. The compensation of losses in the real system can enhance the performance of the system. It contains the additional current values $i_{\mathrm{M-}}$ and $i_{\mathrm{M+}}$ compensating the effects of the ball screw (see chapter 4.1.1).

To optimize the behavior of the controlled system, the desired current value calculated by the controller is added to the motor with the same logic, in which the systems changes between the stiffness values k_{v} for the calculation of the desired torque/force.

During the fall of the leg the PID-controller current is set to zero. The system reaches a high level of force when hitting the knee stop, which results in a very high error in the force control. If not turned of during these events, the controller would produce unreasonable high values for the desired current. Early simulations showed that these peaks downgrade the performance of the system.

A criterion to evaluate the performance of the controller can be the integrated absolute error of the force over the time $F_{\mathrm{err,int}}$. Necessary values are the desired force at the end of the drive-train F_{des} and the actual force measured by the force sensor F_{dt}. The error is only recorded when the controller is active (when $k_{\mathrm{v}} \neq 0$). This circumstance is be expressed by a logic operator c_{switch}, which is set to zero if the stiffness is set to zero, and is set to one when the stiffness is switched to a value unequal zero.

$$F_{\text{err,int}} = \int\limits_T (c_{\text{switch}} \, |(F_{\text{des}} - F_{\text{dt}})|) \tag{4.12}$$

The presented experiment with the feed-forward approach of the combination of bang-bang control and the continuous change of the spring stiffness serves as a benchmark. Parameters of this benchmark test are shown in Fig. 4.2.

Table 4.2.: Benchmark parameters of the experiment with bang-bang control and continuous change of the stiffness

parameters - feed forward	
switching height 1	$\mathrm{x_{h+}} = 0.45$ m
switching height 2	$\mathrm{x_{h\text{-}}} = 0.22$ m
angle knee stop	$\phi_{\text{max}} = 120$ °
maximum current of the motor	$\mathrm{i_{M,max}} = 100$ A
length of the experiment	$\mathrm{T}=5s$
energy injection through change of spring rate	$\Delta W = 5$ J
integrated absolute error	$\mathrm{F_{error,\ int}} = 513.5$ N

Model based control parameter determination I

To derive values for the constants of the PID-controller, a connection between the values has to be found. The procedure is inspired by a method presented in [10].

The starting point lies in the equation of equilibrium between the force acting at the end of the drive-train at the cable F_{dt} and the force driving the knee at the pulley F. They attack at both ends of the cable with the stiffness k_{c}. With this elasticity and the positions of both ends of the cable x_{S1} and x_{S2}, a relationship between both forces can be derived.

$$\begin{aligned} &\text{Part } ①\text{:}\\ &\quad 0 = F_{\text{dt}} - k_{\text{c}}(x_{\text{S1}} - x_{\text{S2}})\\ &\text{Part } ②\text{:}\\ &\quad 0 = -F + k_{\text{c}}(x_{\text{S1}} - x_{\text{S2}})\\ &\quad \text{so:}\\ &\quad F_{\text{dt}} = F \end{aligned} \tag{4.13}$$

F_{dt} is the force at the end of the drive-train and it is assumed that it can be controlled ideally via the motor through the current. The force consists of the desired force F_{des}, the feed forward part described before and a part that depends on the difference between the desired force and the actual force F_{dt}. This value is the error F_{err} of the controlled parameter.

$$F_{\text{err}} = F_{\text{des}} - F_{\text{dt}} \tag{4.14}$$

The value of the error and its derivations are used to change the desired force signal, with the goal to minimize the error. The force resulting from the drive-train now consists of a part given through the desired force and a part resulting from the force error. If the force error becomes zero, the force at the end of the drive-train corresponds with the desired force.

$$F_{\mathrm{dt}} = F_{\mathrm{des}} + k_{\mathrm{P}} F_{\mathrm{err}} + k_{\mathrm{D}} \dot{F}_{\mathrm{err}} + k_{\mathrm{I}} \int F_{\mathrm{err}} \tag{4.15}$$

The parameters k_{P}, k_{I} and k_{D} can be tuned to gain different system behavior. F_{dt} is equal to the actual force F_{act} measured with the force sensor. As shown the elasticity of the cable k_{c} does not influence the results of this approach. With some operations the equation can be transformed in a second order differential equation. In [20] a condition for the critical damping of second order differential equations is given. One parameter of k_{P}, k_{D} and k_{I} can be chosen to realize this condition.

$$\begin{aligned}
&F_{\mathrm{des}} + k_{\mathrm{P}} F_{\mathrm{err}} + k_{\mathrm{D}} \dot{F}_{\mathrm{err}} + k_{\mathrm{I}} \int F_{\mathrm{err}} = F_{\mathrm{act}} \\
&F_{\mathrm{err}} + k_{\mathrm{P}} F_{\mathrm{err}} + k_{\mathrm{D}} \dot{F}_{\mathrm{err}} + k_{\mathrm{I}} \int F_{\mathrm{err}} = 0 \\
&\dot{F}_{\mathrm{err}} + k_{\mathrm{P}} \dot{F}_{\mathrm{err}} + k_{\mathrm{D}} \ddot{F}_{\mathrm{err}} + k_{\mathrm{I}} F_{\mathrm{err}} = 0 \\
&\ddot{F}_{\mathrm{err}} + \frac{1 + k_{\mathrm{P}}}{k_{\mathrm{D}}} \dot{F}_{\mathrm{err}} + \frac{k_{\mathrm{I}}}{k_{\mathrm{D}}} F_{\mathrm{err}} = 0
\end{aligned} \tag{4.16}$$

condition for critical damping of the system:

$$\begin{aligned}
&\frac{1 + k_{\mathrm{P}}}{2 k_{\mathrm{D}}} = \sqrt{\frac{k_{\mathrm{I}}}{k_{\mathrm{D}}}} \\
&k_{\mathrm{I}} = \frac{(1 + k_{\mathrm{P}})^2}{4 k_{\mathrm{D}}}
\end{aligned} \tag{4.17}$$

One of the parameters is fixed with this condition. The other two can be chosen dependent on a performance criteria. The experiment performed in fig. 4.13 shows the comparison of the uncontrolled and the controlled hopping motion. With a control the error of the force can be reduced, resulting in a higher hopping height.

In this experiment the chosen performance criteria, the integrated error $F_{\mathrm{error,\,int}}$, sums up to $F_{\mathrm{error,\,int}} = 153.4$ N, less than a third of the uncontrolled system over the same time period.

On the other hand there are maximum values for the current bigger than $i_{\mathrm{M}} = 60$ A and forces on the cable bigger than $F = 2500$ N. These values are not bearable for the real test-bed. A better performance can be realized in theory but for the limitations of the used components it can not be realized in reality under this circumstances.

A simulation with the actual current limits of the motor shows that the performance with an enabled controller comes near to the same results as without one.

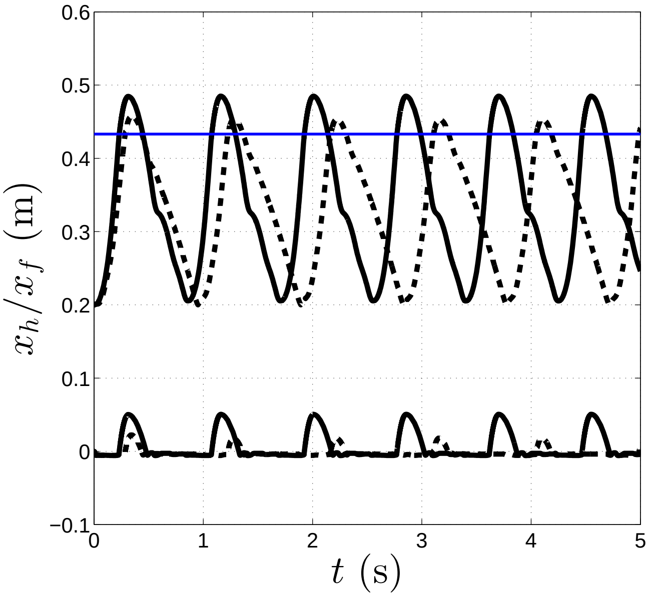

Figure 4.13.: [SIM] Comparison of the motion patterns of a segmented leg with drive-train under the influence of a force PID-control (solid line). The system without PID-control is shown by the dashed lines. The control parameters are set to $k_P = 1$, $k_D = 0.03$ and $k_I = 33.3$. The vertical solid line shows the position of the stretched leg. The injected energy through the control is set to $\Delta W = 5$ J. The solver used in the simulation is ODE23.

Optimization of the PID parameters

Up to now the values for k_P and k_D were chosen by trial and error. k_I has been calculated by the derived law.

Now a map is be presented that shows the performance over a certain range of values for k_P and k_D. The chosen area for these parameters is $k_P = 0.1 + N0.2$ and $k_D = 0.01 + N0.02$ for $N = 1-9$. All combinations of these set of parameters were combined and the resulting performance is evaluated by $F_{\text{err,int}}$ over a time of $T = 3$ s. The parameter of the stiffness control is set to $\Delta W = 5$ J (the results are listed in Fig. A.2).

The optimum point within this range of values is at the point $k_P = 2$, $k_D = 0.05$ and through the calculation $k_I = 45$. The integrated error sums up to $F_{\text{err,int}} = 31.68$ N. The benchmark value for a system without control over a period of three seconds is $F_{\text{err,int}} = 214$.

A problem lies within the values for the current (peaks over $i_M = 80$ A) and the force on the cable (peaks over $F_{\text{dt}} = 6000$ N). One possibility to reduce this values is to choose control parameters that are not in the optimum but are near to an optimum in the possible range of current and force values. A possibility is to reduce the k_P and k_D values. As to see in Fig. 4.14, sets of parameters are possible where low values of error are reached and the control parameters are relative low.

An experiment for $k_P = 0.5$ and $k_D = 0.03$ is performed. The integrated error is $F_{\text{err,in}} = 164.4$ N. The maximum peak value for the motor current is reduced to $i_M \approx 50$ A, while the force in the drive-train can not be reduced and is also about $F_{\text{dt}} = 2500$ N. Beside the peaks values the highest values for the motor current are about $i_M \approx 20$ A.

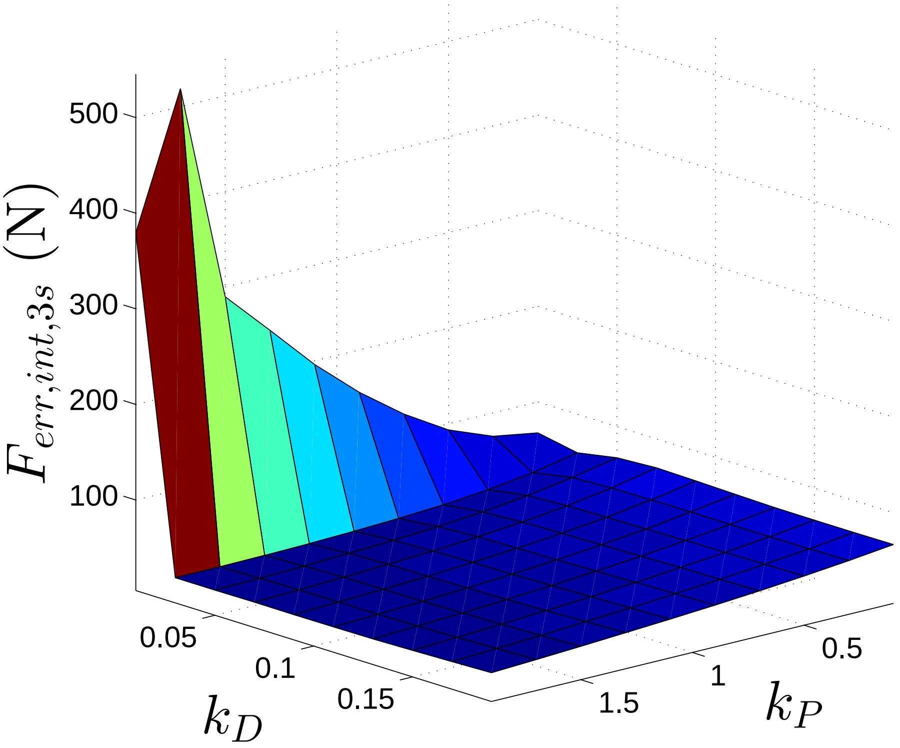

Figure 4.14.: [SIM] The integrated error $F_{\text{err, int}}$ over the parameters k_{P} in the range 0.1 to 2 and k_{D} in the range 0.01 to 0.2. The simulation is performed over a time period of 3 seconds. There is a optimum point for the control parameters. The solver used in the simulation is ODE23.

Model based control parameter determination II

Similar to the chosen concept, the section before, a second model based approach is developed. This time some more information of the drive-train is included in the development. Whereas before a relationship of forces at the end of the drive-train was used, this approach begins with the dynamic equations of the motor.

A variation of the same idea as in the first approach is used. The load torque, represented by the actual force F_{act}, and the motor torque, represented by a certain desired current, attack at the motor. The motor torque can be calculated by the desired current and the torque constant k_{M}. The desired current derives from a desired force F_{des} (calculated through the virtual model control) and an additional term consisting of derivations of the force error F_{err}. If both, the error and the acceleration of the motor, become zero, the actual force and the desired force are

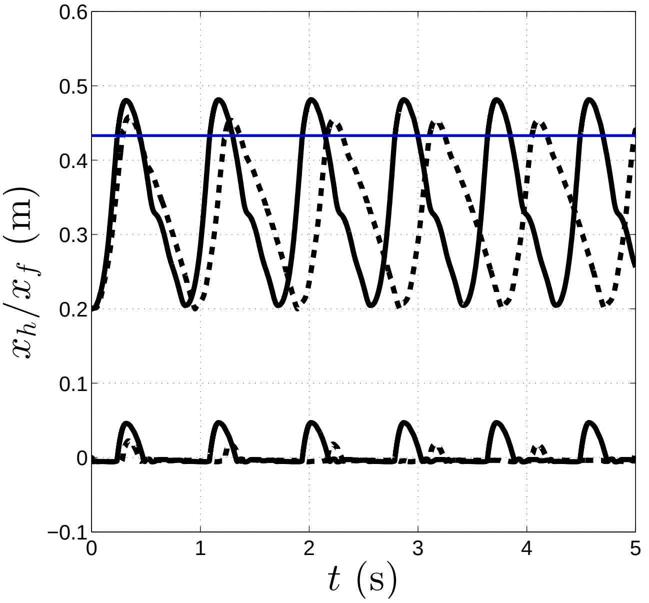

Figure 4.15.: [SIM] Comparison of the motion patterns of a segmented leg with drive-train under the influence of a force PID-control (solid line). The system without PID-control is shown by the dashed lines. The control parameters are set to $k_\mathrm{P} = 0.5$, $k_\mathrm{D} = 0.03$ and $k_\mathrm{I} = 18.75$. The vertical solid line shows the position of the stretched leg. The injected energy through the control is set to $\Delta W = 5$ J. The solver used in the simulation is ODE23.

the same. The same approach of critical damping is chosen for the adjustment of the control parameters.

$$
\begin{aligned}
\theta \ddot{\phi}_\mathrm{M} &= -F_\mathrm{act}\frac{1}{i_\mathrm{T} i_\mathrm{bs} \eta_\mathrm{T} \eta_\mathrm{bs}} + k_\mathrm{M}\left(F_\mathrm{des}\frac{1}{i_\mathrm{T} i_\mathrm{bs} \eta_\mathrm{T} \eta_\mathrm{bs} k_\mathrm{M}} + k_\mathrm{P} F_\mathrm{err} + k_\mathrm{D}\dot{F}_\mathrm{err} + k_\mathrm{I}\int F_\mathrm{err}\right)\\
\theta \ddot{\phi}_\mathrm{M} &= F_\mathrm{err}\frac{1}{i_\mathrm{T} i_\mathrm{bs} \eta_\mathrm{T} \eta_\mathrm{bs}} + k_\mathrm{M}\left(k_\mathrm{P} F_\mathrm{err} + k_\mathrm{D}\dot{F}_\mathrm{err} + k_\mathrm{I}\int F_\mathrm{err}\right)\\
\theta \ddot{\phi}_\mathrm{M} &= F_\mathrm{err}\frac{1}{i_\mathrm{T} i_\mathrm{bs} \eta_\mathrm{T} \eta_\mathrm{bs}} + k_\mathrm{M} k_\mathrm{P} + k_\mathrm{M} k_\mathrm{D}\dot{F}_\mathrm{err} + k_\mathrm{M} k_\mathrm{I}\int F_\mathrm{err}\\
\theta \dddot{\phi} &= \ddot{F}_\mathrm{err} + \dot{F}_\mathrm{err}\left(\frac{\frac{1}{i_\mathrm{T} i_\mathrm{bs} \eta_\mathrm{T} \eta_\mathrm{bs}} + k_\mathrm{M} k_\mathrm{P}}{k_\mathrm{M} k_\mathrm{D}}\right) + \frac{k_\mathrm{I}}{k_\mathrm{D}} F_\mathrm{err}\\
&\textbf{particular part:}\\
0 &= \ddot{F}_\mathrm{err} + \dot{F}_\mathrm{err}\left(\frac{\frac{1}{i_\mathrm{T} i_\mathrm{bs} \eta_\mathrm{T} \eta_\mathrm{bs}} + k_\mathrm{M} k_\mathrm{P}}{k_\mathrm{M} k_\mathrm{D}}\right) + \frac{k_\mathrm{I}}{k_\mathrm{D}} F_\mathrm{err}
\end{aligned}
\tag{4.18}
$$

condition for critical damping of the system:

$$\left(\frac{\frac{1}{i_T i_{bs} \eta_T \eta_{bs}} + k_M k_P}{2 k_M k_D}\right) = \sqrt{\frac{k_I}{k_D}}$$
$$k_I = \frac{\left(\frac{1}{i_T i_{bs} \eta_T \eta_{bs}} + k_M k_P\right)^2}{4 k_M^2 k_D} \tag{4.19}$$

Also an optimization of the control parameters has been performed. It has been chosen the same parameter range as in the first approach. The area for these parameters is $k_P = 0.1 + N0.2$ and $k_D = 0.01 + N0.02$ for $N = 1 - 9$. All combinations of these set of parameters were combined and the resulting performance is evaluated by $F_{\text{err,int}}$ over a time of $T = 3$ s. The parameter of the stiffness control is set to $\Delta W = 5$ J (the results are listed in Fig. A.3).

The resulting error over the range of parameters is shown in Fig. 4.16. Unequal to the parameter map of the first approach, there is no area where the error stays low over a wide range of parameters. If this approach is chosen, the exact choice of parameters is more important. The lowest error can be reached with control values of $k_P = 2$ and $k_D = 0.03$. The optimal point lies in the same region as in the approach before. An integrated error of $F_{err,int} \approx 37$ N is reached. Therefore, the performance of the more complicated approach is worse than of the first one.

The simulation with the controller model based on the motor is shown in Fig. 4.17. The same energy injection setup of $\Delta W = 5$ J for the values of k_P and k_D is used to make the results comparable. The performance is also enhanced and the integrated error comes to $F_{\text{error, int}} = 151.1$ N.

This is close to the half of the uncontrolled system but also a much higher value than for the first control approach. The desired current is reduced to values less than $i = 30$ A most of the time. Also the forces on the cable are less than $F = 2700$ N. This is still to high for the test-bed.

Current limitation and performance

The error map over the control parameters k_P and k_D is shown in Fig. 4.18. The third parameter k_I is calculated through the first model based calculation. During the development of this map the current in the system was limited to $i_M = 10.5$ A. The same limit is given by the properties of the test bed.

As shown, the lowest error for this constellation is given when the control parameters are near to zero. Every setup of control parameters downgrades the performance of the system. With the actual limitations of the current and the developed control strategies an improvement of the performance is not possible.

Summary model based PID control in combination with virtual model control

An improvement of the performance of the control can be produced by the use of a PID-control in combination with the most developed calculation approach for k_v. Two methods for the choice of

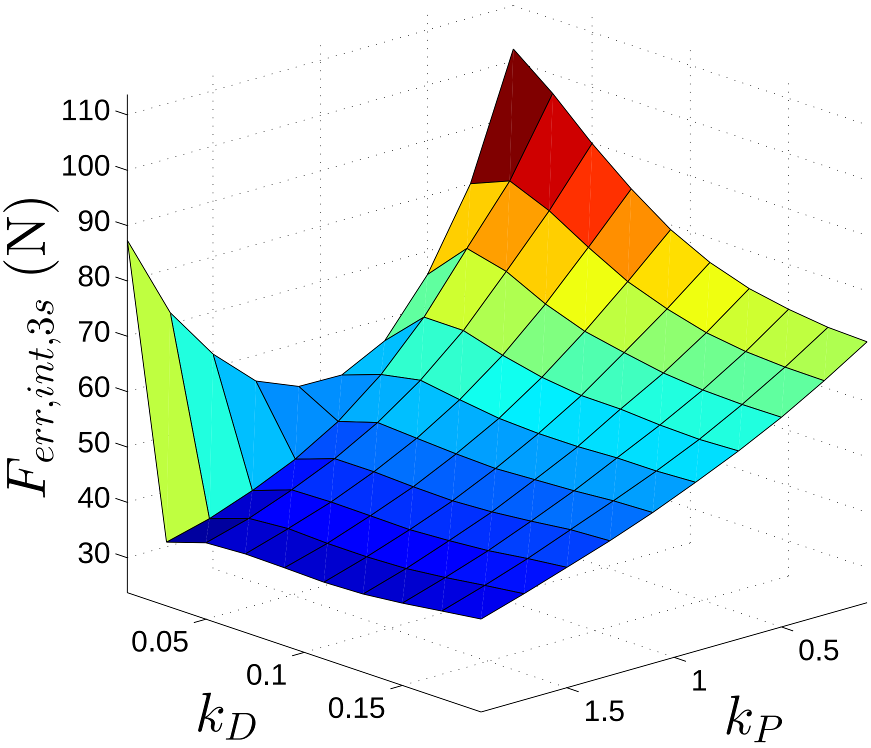

Figure 4.16.: [SIM] The integrated error $F_{\text{err, int}}$ over the parameters k_{P} in the range 0.1 to 2 and k_{D} in the range 0.01 to 0.2. The simulation is performed over a time period of 3 seconds. The solver used in the simulation is ODE23.

control parameters have been presented. The first approach is recommended, as it is simpler. A choice of the free parameters is very flexible and not as sensitive to improper chosen parameters. Over a wide parameter range, good results can be reached.

One problem of the control approaches is the limitation of the possible current. An improvement of performance is always connected with higher values of motor current i_{M} and of the force at the cable F_{dt}. These values can not be realized in the current state of the test bed. So the force control approach is promising but not easy to realize.

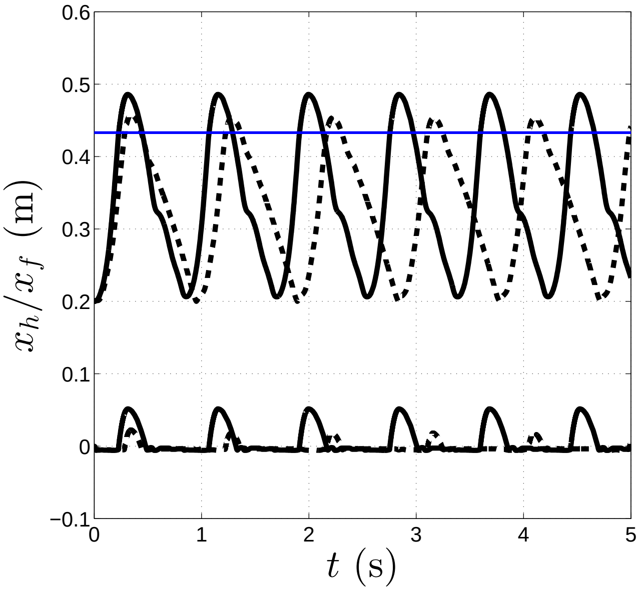

Figure 4.17.: [SIM] Comparison of the motion patterns of a segmented leg with drive-train under the influence of a force PID-control (solid line). The system without PID-control is shown by the dashed lines. The control parameters are set to $k_{\mathrm{P}} = 2$, $k_{\mathrm{D}} = 0.03$ and $k_{\mathrm{I}} = 34$. The vertical solid line shows the position of the stretched leg. The injected energy through the control is set to $\Delta W = 5$ J. The solver used in the simulation is ODE23.

4.2 Force control - PID

In this section the possibility of a force PID-control for the test-bed shall be investigated. The principle is shown in Fig. 4.19. The change of the concept lies in the instance that the direct connection from the virtual model control to the actuator is erased. The PID-controller sets, dependent on the force error, the desired current values to the motor. There is no feed-forward term in the system.

For the test of this approach the adjustment law for the control parameters from the last section is used, $k_{\mathrm{P}} = 2$, $k_{\mathrm{D}} = 0.03$, $k_{\mathrm{I}} = 75$ and $\Delta W = 5$ J. The PID-controller is still switched in the same manner as the stiffness for the virtual model control part. The results are shown in Fig. 4.20. In Fig. 4.20 (a) the current is not limited. In Fig. 4.20 (b) the current is limited to $i_{\mathrm{M}} = 10.5$ A. The first thing to note is that it is possible to control a stable hopping motion through a PID-control approach.

Even in the case of limitation of the motor current a stable hopping motion is feasible. The hopping height and frequency is comparable to the values reached through the combination of bang-bang control and a continuous change of spring stiffness (see Fig. 4.11). With the simpler approach of the combination of bang-bang control and a continuous change of spring stiffness, the same results are feasible. No further sensor information than the positions of hip and foot are necessary for this method.

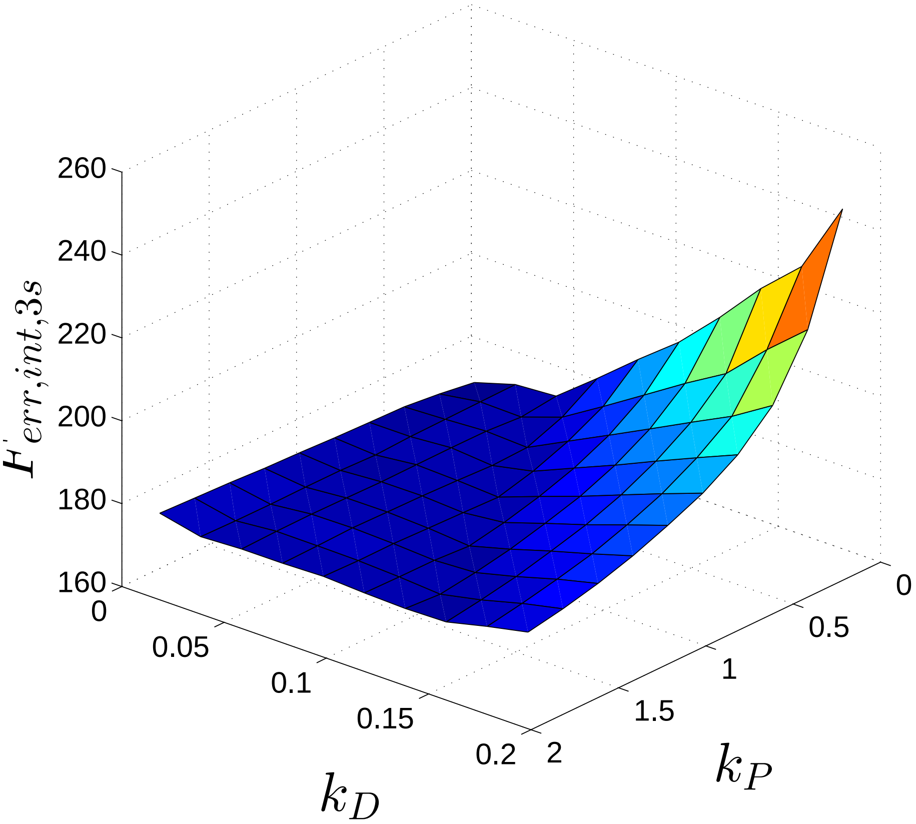

Figure 4.18.: [SIM] The integrated error $F_{\text{err, int}}$ over the parameters k_{P} in the range 0.1 to 2 and k_{D} in the range 0.01 to 0.2. The simulation is performed over a time period of 3 seconds. $\Delta W = 5$ J and the current is limited to $i_{\text{M}} = 10.5A$. The solver used in the simulation is ODE23.

In the case of the PID-control the information of the actual force is needed as well, which increases the complexity of the system and makes it more prone to disturbances. Furthermore, the incorrect adjustment of control parameters could downgrade the performance.

For this reasons a PID control is not recommended. Only if a possibility is found to extend the range of motor current, the PID-control could enhance the performance of the feed-forward control schemes. With additional sensor information and signal conversion processes the probability of errors rises.

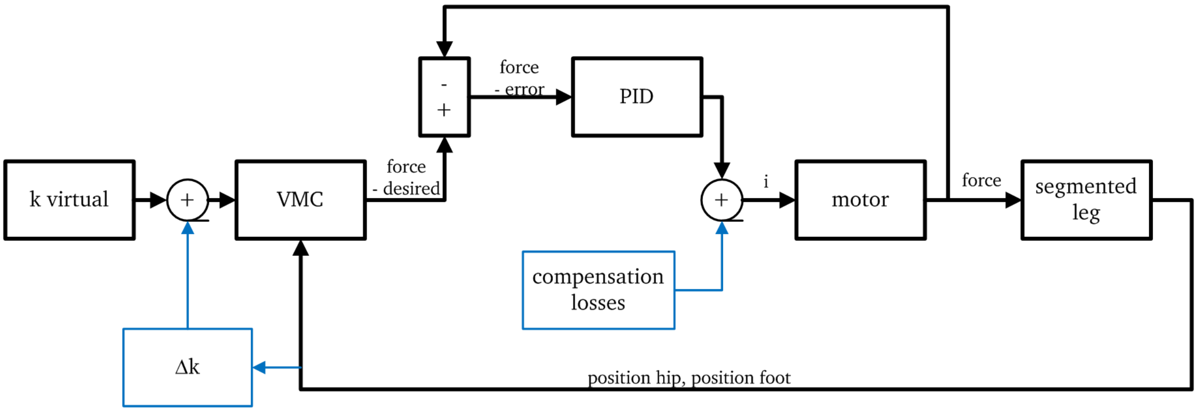

Figure 4.19.: Control block diagram of an alternative to the continuous change of spring stiffness approach. The current is now controlled with an additional PID-force-control part. As before the darker boxes show the basic mechanism of the system. An additional stiffness Δk is added to the system dependent on the positions of hip and foot. The error resulting from the desired- and actual force is used to control the system with a PID-controller. The compensation of losses in the real system can enhance the performance of the system.

4.3 Position control - SEA

A possibility, not mentioned before, is the combination of a serial elastic actuation (SEA) concept with a position control. This method is used in [23] and [24]. In these works the virtual model control approach is used to generate desired values for certain forces. The force is not controlled directly.

At each point, where the force should be controlled, an elasticity in combination with the actuator and one position sensor at each end, is fixed. With the knowledge of the positions and the value of the stiffness of the elasticity, the actual force can be determined. Therefore, a force control can be implemented as a position control and without the need of a force sensor. If certain positions (or differences between positions) are reached, the desired force could be accomplished.

This method is also possible for the drive-train of MARCO Hopper II. In this case a spring has to be attached between the two carriages in the drive-train (see Fig. 4.21). The position of the first carriage x_{bs} can be determined by the angular sensor of the motor and the transmission ratios of motor transmission i_{T} and ball screw i_{bs}.

$$x_{\mathrm{bs}} = \frac{\phi_{\mathrm{M}}}{i_{\mathrm{T}} i_{\mathrm{bs}}} \tag{4.20}$$

A position of the second carriage x_{c2} can be measured by an own potentiometer sensor already attached on the test-bed. The force in the drive-train F_{dt} can be calculated with these positions, the rest length of the spring $l_{0,\mathrm{SEA}}$ and its spring rate k_{SEA}.

$$F_{\mathrm{dt}} = k_{\mathrm{SEA}} \left(x_{\mathrm{bs}} - x_{\mathrm{c2}} - l_{0,\mathrm{SEA}} \right) \tag{4.21}$$

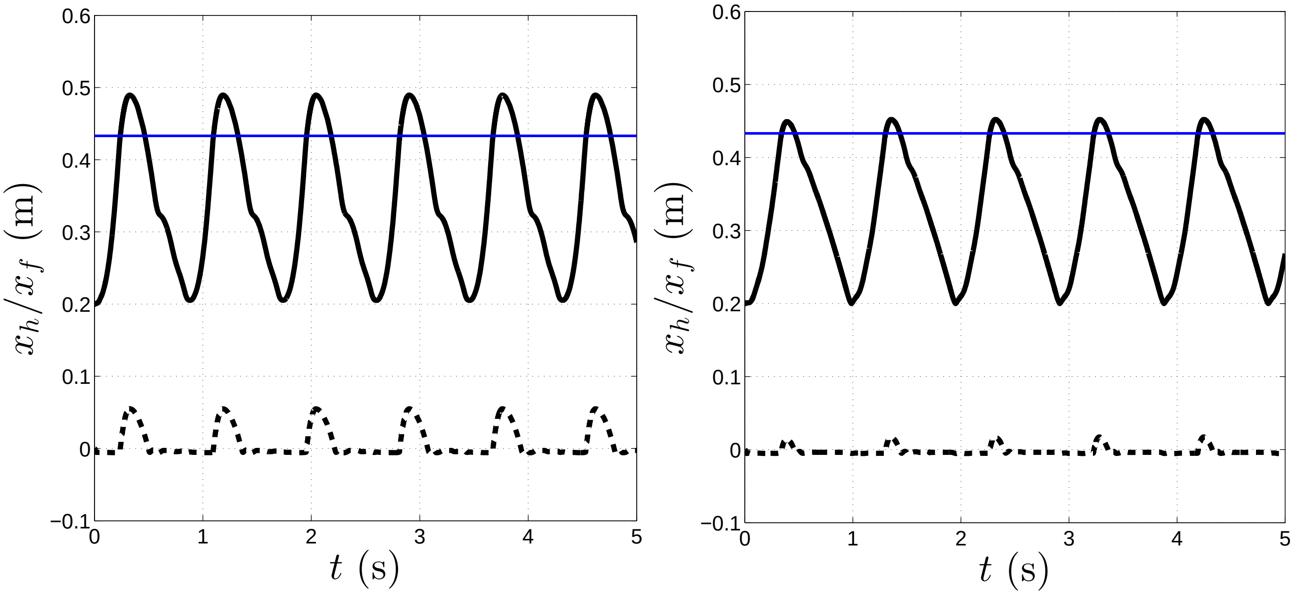

(a) **(b)**

Figure 4.20.: [SIM] Comparison of the motion patterns of a segmented leg with drive-train under the influence of a force PID-control. The control parameters are set to $k_{\mathrm{P}} = 2$, $k_{\mathrm{D}} = 0.03$ and $k_{\mathrm{I}} = 34$. The vertical solid line shows the position of the stretched leg. The injected energy through the control is set to $\Delta W = 5$ J. The difference of both systems lies in the limitation of the current. In (a) the current is not limited, while in (b) the current is limited by $i_{\mathrm{M,,max}} = 10.5$ A. The solver used in the simulation is ODE23.

The desired difference between the positions of the carriages $\Delta x_{\mathrm{bs,des}}$ becomes the control parameter when a desired force is given.

$$\begin{aligned} F_{\mathrm{dt}} &= F_{\mathrm{des}} \\ x_{\mathrm{bs}} - x_{\mathrm{c2}} &= \Delta x_{\mathrm{bs}} \\ \Delta x_{\mathrm{bs,des}} &= \frac{F_{\mathrm{des}}}{k_{\mathrm{SEA}}} + l_{0,\mathrm{SEA}} \end{aligned} \tag{4.22}$$

For this approach has neither been implemented on the test-bed nor has been tested in simulation, no further developments are shown at this point.

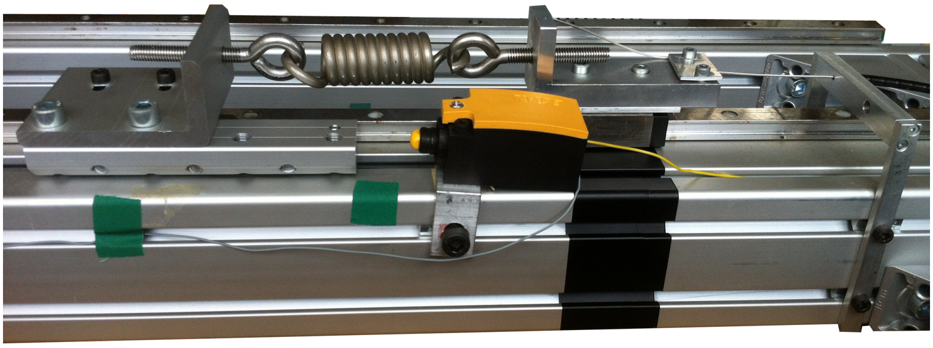

Figure 4.21.: Possible attachment place of a spring in the drive-train. The elasticity is attached between the carriages of the drive-train. The position of both carriages could be determined (the left one through the motor position, the right one with a potentiometer position sensor, comparable to the one used to measure the foot position). With these positions a force/position control could be implemented.

5 Experiments and suggestion for changes

This section includes specialties of the approach and goes into some characteristics of the test-bed and the control, which were not mentioned before. Furthermore, suggestions will be made to enhance the performance of the test-bed.

5.1 Experiments

Some special characteristics of the test-bed and simulation and also a comparison with an example of human hopping are shown.

5.1.1 Theoretical power consumption and motor current requirements

A maximum required power of $P = 23.7$ W was assumed in the development of MARCO Hopper II [9]. Examinations of the simulation models developed in this thesis show that the true necessary power goes beyond this value.

As an example the simulation of a hopping motion with bang-bang control and continuous change of spring stiffness with a $\Delta W = 5$ J is performed and the resulting power consumption will be shown.

The results are shown in Fig. 5.1. Negative peak values of the power result from the circumstance that the motor drives in the stretched cable when the leg hits the knee stop. The second periodic negative peak value of lesser magnitude marks the change of direction of the motor when the stiffness is changed through the bang-bang control.

The crucial peak value is the positive value of $P_{\mathrm{M}} \approx 70$ W. This power is necessary to perform the hopping motion. Although the resulting hopping motion is not that high, the power consumption is more than twice as high as assumed during the concept development of MARCO Hopper II in [9]. The motor is able to provide power up to $P_{\mathrm{M}} = 200$ W but the motor current is most of the time at its limit of $i_{\mathrm{M}} = 10.5$ A during this experiment.

A possibility for using the power of the motor is to use the whole range of motor velocity. A change of transmission ratios can make this possible. A lower value of current is necessary to gain the same forces at the end of the drive-train. This circumstance is easy to see with the equation for the desired torque τ_{des}.

$$i_{\mathrm{M}} = \frac{\tau_{\mathrm{des}}}{r_{\mathrm{p}}\eta_{\mathrm{c}}} \frac{1}{i_{\mathrm{bs}} i_{\mathrm{T}} \eta_{\mathrm{bs}} \eta_{\mathrm{T}} k_{\mathrm{M}}} \tag{5.1}$$

The desired torque will stay the same. To lower the desired current, all other values have to be raised. The efficiencies η_{c}, η_{bs} and η_{T} can not be changed. The transmission of the ball screw i_{bs}

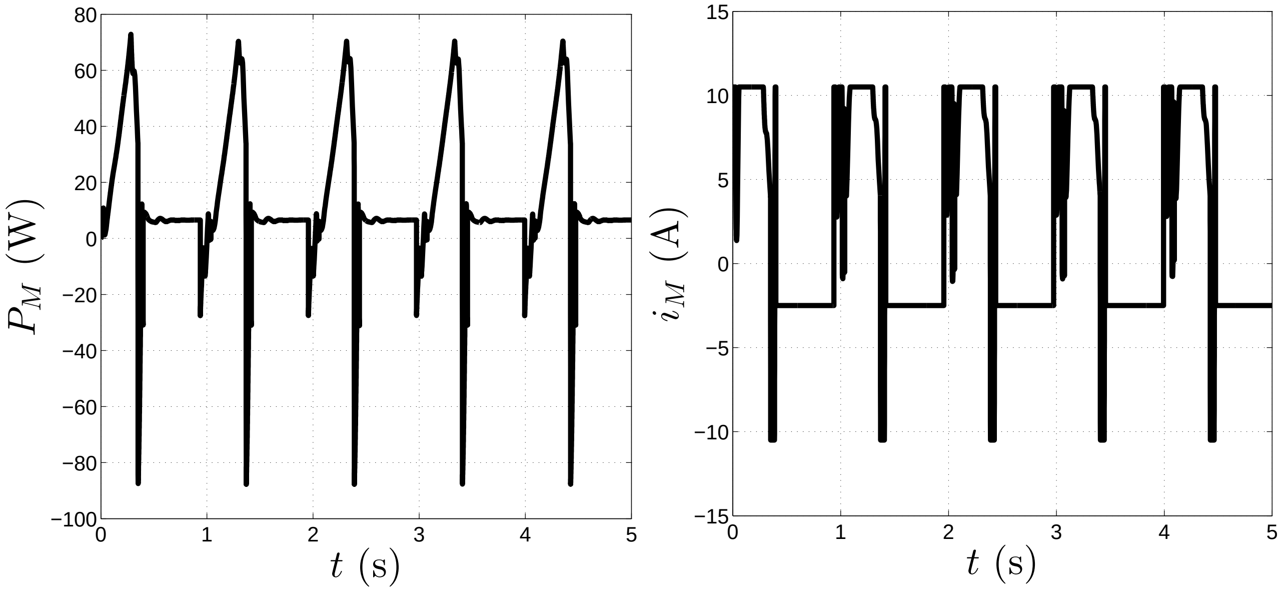

(a) **(b)**

Figure 5.1.: [SIM] Power consumption of the motor P_{M} (a) (calculated with the angular velocity of the motor ϕ_{M} and the load torque on the motor τ_{M}) and motor current i_{M} (b) during the hopping experiment shown in Fig. 4.11. The injected energy is tuned to be $\Delta W = 5$ J.

is also fixed. A ball screw with different properties is difficult to implement in the drive-train and is also expensive.

The most promising measures are to change the radius of the pulley r_{p} and to attach a different motor transmission i_{T}. A motor transmission is also expensive but easy to change in the test-bed. The easiest part to change is the pulley.

It has to be considered that a raise of transmission values always raises the necessary motion range of the drive-train. The limits of the ball screw have to be respected.

5.1.2 Ground reaction force - leg length relationship

A relationship that is regarded for locomotion experiments and theory is the relationship between the ground reaction force F_{GRF} and the leg length l_{leg} (depending on the positions of hip x_{h} and foot x_{f}).

$$l_{\mathrm{leg}} = x_{\mathrm{h}} - x_{\mathrm{f}} \tag{5.2}$$

The comparison of this relationship between a single mass oscillator and the segmented leg is shown in Fig. 5.2. A fixed value for k (the black lines) and a continuous change of the spring stiffness with bang-bang control ($k_0 + \Delta k$, the blue lines) is shown for both systems. The basic stiffness was set to the value, which is necessary to reach the rest-length of the spring. The injected energy is set to $\Delta W = 1$ J for both systems. The system switches between $k_{\mathrm{v}} = k_0$ and $k_{\mathrm{v}} = k_0 + \Delta k$. The peaks of the force in the beginning of Fig. 5.2 come from the sudden

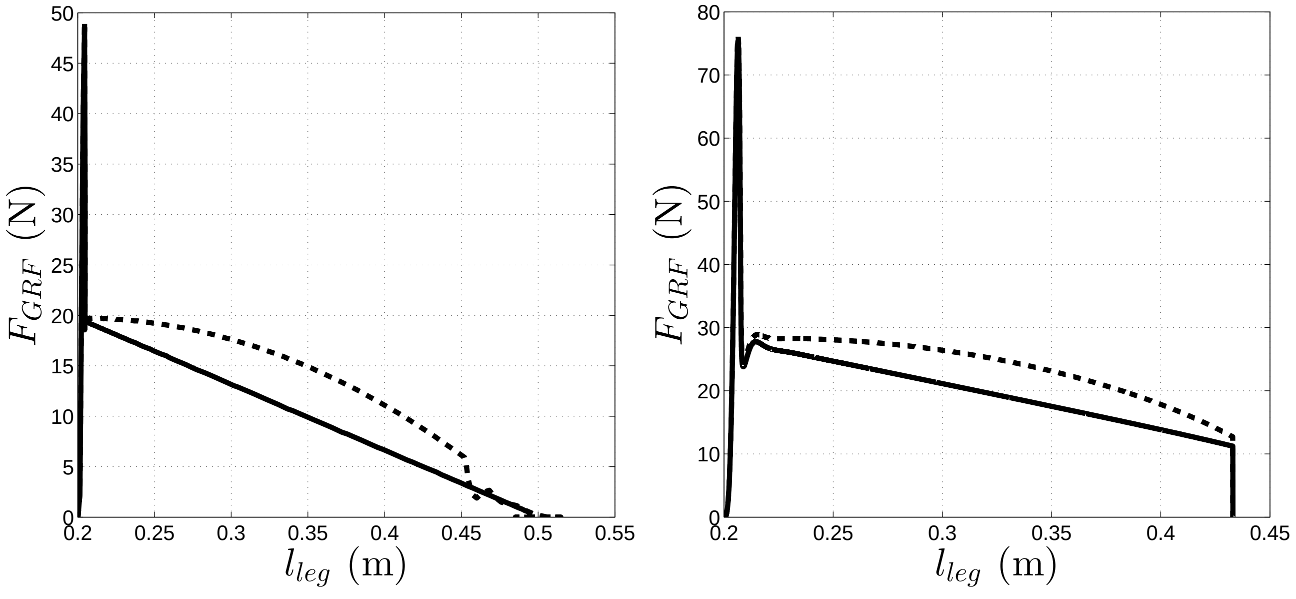

(a) **(b)**

Figure 5.2.: [SIM] Comparison of the relationship between ground reaction force and rest length of a single hop with a control tuned to $\Delta W = 1$ J. Friction forces are turned to zero. The single mass oscillator (a) has a mass of $m = 1$ kg. Different line-types stand for the different calculation methods for k. The solid line has a fixed value of k, a linear spring. For the dashed line the stiffness was changed in the fashion of the continuous change of stiffness with bang-bang control. The segmented leg (b) is tuned with its real masses.

deformation of the ground in the beginning of the motion and do not have a further meaning.

A characteristic of the segmented leg is the knee stop that prevents the leg from reaching the rest-length of the virtual spring. A hop starts when the leg length is $l_{\text{leg}} \approx 0.43$ m. The ground reaction force is already zero while the spring would exert further force on the leg.

The area underneath the lines determines the energy injected in the system. A difference between a fixed stiffness and a variable stiffness and the energy that is additional injected through the continuous change of spring stiffness can be determined that way. For future work on the test-bed and additional actuation methods, examinations of this relationships can be interesting.

5.1.3 Comparison to human hopping motions

It has been shown that the model of the segmented leg with distributed masses can be controlled in the fashion of a single mass oscillator respectively the SLIP model. Now the resulting motion and also the pattern of the ground reaction forces are compared with human hopping data.

For it was not possible to gather special locomotion data that fits the requirements and parameters of this thesis, the comparison shall be made with existing research results from [17]. In this work also the reaction to perturbations, in form of a changing ground level, was examined. Therefore, the perturbation is shown in the motion and force patterns. For this comparison only the frequency of the motion and the pattern of the ground reaction force and the movement are regarded.

The simulation is performed with the model of the segmented leg, without an attached drive-train. Also the friction forces in the bearings of the hip and the foot were turned to zero. In the case of a real segmented leg there are no bearings that influence the motion.

Also the force by the hip bed-stop was turned to zero. The leg can now be imagined as a segmented leg moving in one direction, only influenced by the ground reaction force and the driving torque τ at the knee.

It was chosen the bang-bang approach with a continuous change of stiffness in the fashion of chapter 4.1.3 for the actuation. One difference is given in the circumstance that in this experiment the stiffness is not turned to zero, but to the basic value k_0. So the same control pattern as in [17] was chosen. This makes the results more comparable.

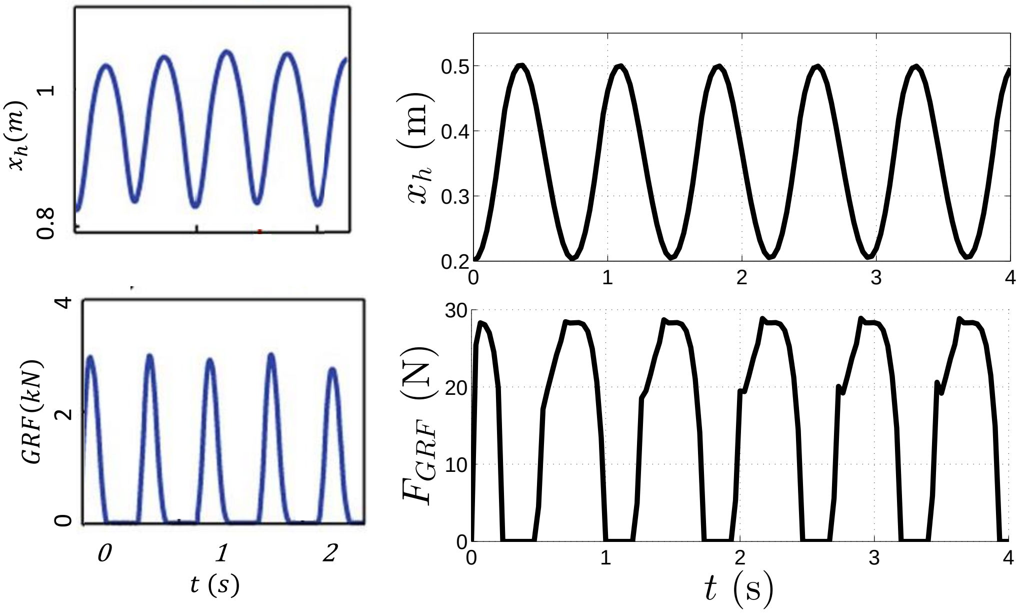

(a) **(b)**

Figure 5.3.: Comparison of the patterns of motion and ground reaction force of the segmented leg and a human hopping motion. The human hopping data (a) is from [17]. Parameters of the experiment in (b) are $\Delta W = 1$ J and switching points of $x_{\text{h+}} = 0.45$ m and $x_{\text{h-}} = 0.22$ m. The solver used is ODE23.

The pattern of movement and also the pattern of ground reaction forces are similar but not equal. A stable hopping motion with an almost constant level of hopping height can be realized. The peak and course of the force pattern is smoother for the human model. The course of the force during the first hop in the simulation comes very close to the pattern of the human model. Also the force pattern during the second half of each hopping cycle (maximum compression to take-off) comes close to the human model.

A likely explanation is that there are deviations from a realistic situation in the impact modeling/ground model of the simulation. Second, the segmented leg consists only of two segments. The influence of the foot is not regarded.

In this experiment a look at the model of the segmented leg has been taken, that is separated from the drive-train and the influence of the friction forces on the leg.

The smooth motion and force patterns derived here, are only possible when the leg is seen as an ideal model. Losses only are introduced through the ground and the demanded torque at the knee could be provided at all times.

The experiments with the real test-bed show that the resulting movements change due to the losses and influences of the bearings and the imperfections of the drive-train. A suitable indicator for this circumstance is the adjustment of the control parameter ΔW. The hopping motion performed for the segmented leg needs an energy injection of $\Delta W = 1$ J. At least a value of $\Delta W = 5$ J was necessary to perform a hopping motion on the test-bed for the experiments performed in the control chapters.

Nonetheless a hopping motion can be performed with the shown control schemes but the distance to the biological inspiration is getting higher due to the characteristics of the test-bed. Concepts of actuation can be tried but the performance and comparability is limited.

5.2 Problems and suggestion for changes

In this section suggestions for the enhancement of performance of the test shall be made.

5.2.1 Motor controller

An internal current control of the motor controller sets the desired currents to the motor. This task is performed by a controller from *maxxon* the *Escon Module 50/5, 4-Q*. The internal control is realized by a PI controller with the current values of $k_\mathrm{P} = 59$ and a reset time of $T_\mathrm{N} = 0.286$ s. The control values can be tuned manually or by an automatic tuning. This controller is presented with a desired current value by the embedded hardware controller *MyRIO* and controls the current in the motor.

The problems deriving from the current control are shown in Fig. 5.4. Oscillations around the desired value happen most of the time. Especially during the backward movement (the current is negative) this oscillations could influence the system behavior in a negative way. The oscillations around the desired value are compared to this value rather high (the current fluctuates between $i_\mathrm{M} \approx -1$ A and $i_\mathrm{M} \approx -3$ A. The backward motion of the carriages is probably disturbed. The assumption is, that this behavior leads to the slow backward motion of the drive-train. A test for this assumption has to be performed yet.

A second problem is shown during the third cycle of the experiment. The current suddenly drops to $i_\mathrm{M} \approx 5$ A. This behavior is responsible for the unstable motion in Fig. 4.7 and Fig. 4.11. The hopping motion can not be performed further on because the necessary current to drive the motor can not be reached.

These problems can not be solved until the current moment. A proper tuning of the motor controller and a fix for the problem with the dropping current are necessary to produce a stable hopping motion and to improve the performance.

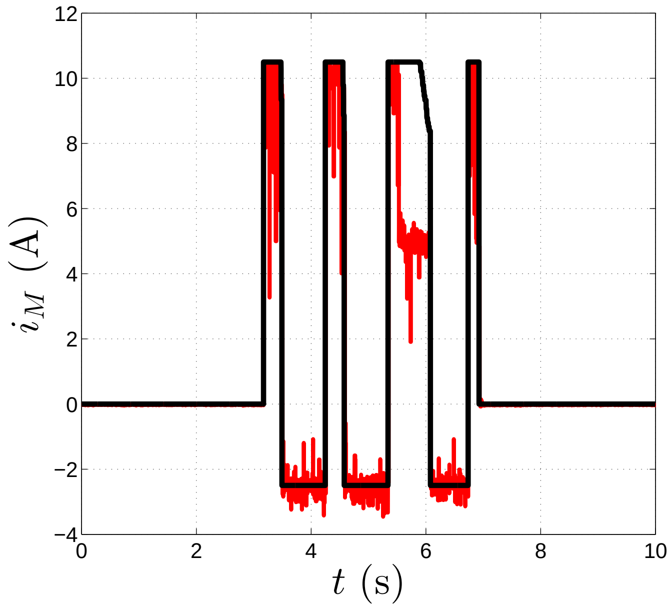

Figure 5.4.: [EXP] The course of the desired (black line) and the actual motor current (lighter line) during an experiment on the test-bed.

5.2.2 Change of the knee pulley

For the test-bed is driven in the limits of its capability (e.g. current limit, strain of the cable) a lowering of the necessary forces in the drive-train can improve the performance and lessen the needed power of the motor.

A lesser force with a constant torque at the knee can be realized through a higher radius of the knee pulley. The new knee pulley with a diameter of $d_p = 98$ mm instead of the old pulley with a diameter of $d_p = 80$mm has been attached to the segmented leg. Up to this moment no further experiments could be performed with the changed test-bed. Simulations show some positive effects of a bigger pulley.

The condition which has to be regarded if a bigger pulley is used is that with the reduced force, the motion range of the drive-train/ball screw rises. Limits of the possible travel of the drive-train have to be respected if another bigger pulley is attached.

5.2.3 Power sources

In the current setup of MARCO II the test-bed is supplied by two power sources. The power source for the sensors is sufficient for this purpose. Problems with the current of the motor are not exclusive up to the motor controller. The current limit of the actual power supply of the motor is at $i = 10.5$ A and it happened that the power supply turned itself off during the experiments. A power supply with a higher possible current is recommended to avoid this problem.

If the power supply is powerful enough problems with a break-in of the current could be isolated to the motor controller. First tests with more powerful supplies support this assumption.

5.2.4 Reduction of friction

A characteristic of the test-bed that downgrades the performance of the control approaches and also falsifies the motion patterns of the segmented leg is the friction, induced through the bearings of hip and foot. If the friction was reduced better results, as shown before, would be expected.

One possibility for the reduction of friction is the separating of the wipers of the linear bearings/carriages. The stiction force could be lowered significantly. Also alternatives to the current lubrication concept could be considered.

6 Conclusion and future works

In this thesis the possibility of the control of a segmented robotic leg with the virtual model control approach has been investigated.

The virtual model control bases on the implementation of virtual components in real devices to realize a desired behavior. Existing actuators mimic the effects that virtual components would have. A common template for a biological hopping motion is a single mass oscillator, the spring loaded inverted pendulum (SLIP) model. Resulting motion and force patterns come close to the human role model. A virtual spring can be implemented in a segmented leg to mimic the behavior of the SLIP model and, therefore, the biological role model.

A behavior similar to the SLIP model can be accomplished for an ideal segmented leg without losses . In the real test-bed MARCO Hopper II the leg is influenced by losses through friction and damping forces resulting from bearings, the ground and imperfections of the driving forces by the drive-train. Control methods have been developed to counteract those losses and imperfections and to adapt the idea to the test-bed. A promising control method that results in hopping motions in simulation and also on the test-bed has been developed and tested - the bang-bang control of the virtual spring rate with a continuous adjustment of virtual spring stiffness. Only position information is necessary to calculate desired values of force and current for the drive-train and to accomplish the desired behavior (the controlled parameter do not get feedback information).

It has been tested if an overlaid PID force-control can enhance the performance of the test-bed. This task can be accomplished in simulation but not on the test-bed for restrictions of the energy supply and possible motor currents.

Finally suggestions for changes of the test-bed and alternative control methods have been developed.

The idea of serial elastic actuation methods in combination with the derived laws can be interesting for future works. The reduction of power consumption through the use of SEA and resonance effects is a possible topic to investigate. Originally the test-bed has been developed for the possibility of different drive-train concepts and for the resulting advantages and performance enhancements. Muscle models can be accomplished by an adaptation of the drive-train.

The suggestions made to improve the performance of the test-bed must be regarded and developed to realizable solutions. Especially improvements on the motor controller and the overall transmission ratio of the drive-train, through adjustments of the pulley and motor transmission, have to be accomplished.

There are other possible laws for the calculation of the virtual spring stiffness. A first approach for a variable virtual stiffness has been tested. More advanced methods could improve the performance of the control without the necessity of further sensor information. Also a parameter variation of the rest length of the virtual spring could be tested and analyzed.

Up to now the motion has not been disturbed through changes of the ground level or intended forces at different places. A device can be developed to investigate the disturbed behavior and robustness of the control method. In the course of these developments research on ground models and the interaction with the ground can be done. The development of an additional extension of MARCO Hopper II, which holds the possibility of different grounds with an integrated force sensor and perturbation mechanism can be an promising task.

It is also possible to extend the structure to a leg with three segments. A foot with an additional actuated or passive joint is a possible next step. In this way a simple method for the actuation of a whole leg can be realized.

A Appendix

A.1 Run of the test-bed

To run experiments on the test-bed the following steps have to be followed:

1. start PC
2. turn on power sources sensors and motor
3. turn on power source *MyRIO*
4. load *LabView* file
5. set emergency stop to OFF, enable motor controller by switch ON
6. choose function in *LabView*
    - Referenzposition anfahren - carriages drive to reference start position
    - Kraftregelung neu - possibility for run with continuous change of spring stiffness control
    - more functions will follow
7. initialize data record on the GUI - experimental data of the run will be saved in .xlsx-files
8. start function in *LabView*
9. stop function in *LabView*
10. save experimental data on an external data storage medium
11. if problems occur: press emergency stop

Changes of the force-control functions have to be made in the formula node of the *Labview*-file. Implementation of a possibility to tune the parameters in the GUI will follow soon.

A.2 Data DVD

The attached DVD contains all relevant data of this thesis. It is organized as follows:

1. **latex data + print version thesis:**
   Included are the latex files, all used figures and photos and the final version of the thesis.
2. **presentation:**
   The presentation of the thesis as .pptx, all used figures and other material.

3. **simulation models:**:
   All relevant simulation models and m-files necessary to produce the results presented in this thesis.
4. **experimental results + analysis:**
   The results from experiments with MARCO II and necessary m-files for the analysis of the data.
5. **graphics, photos and figures:**
   All diagrams (as .fig-files) produced during the work on the task. Also photos of different parts of MARCO II and sketches of different models.

A.2.1 Simulation models and m-files

A short description of the simulation models and m-files is given. All models were tested with the *Matlab* versions R2013a and R2012b. Necessary information for the run of the models is given in the models and in the corresponding m-files. For the simulation of the model only the model and the m-file are necessary. The simulation is controlled via the m-file and started by the run of the m-file. m-file and simulation model have to be in the same folder and the model must be open in *Matlab*. Name changes have to be executed in both, the simulation model and the m-file.

For most models an iteration over certain parameters, via a for-loop, is possible. The results are shown in diagrams to estimate effects by the iteration. The arrays used for the parameter variations are explained in the corresponding m-files.

SLIP model

Included is the simulation model of the SLIP model "“SLIP_150616.slx"” and the m-file "“parameters_SLIP_150616.m"” necessary to control the model.

The control models of the bang-bang- and continuous-change-of-stiffness-approaches as well as a constant spring stiffness are implemented on the model and the desired case has to be chosen by manual switches in the model.

Segmented leg without drive-train

Included is the simulation model of the segmented leg as *SimMechanics* model "“extented_model_150708_VMC.slx"” and the m-file "“parameters_model_150708_VMC.m"” necessary to control the model.

The control models of the bang-bang- and continuous-change-of-stiffness-approaches are implemented on the model and the desired case has to be chosen by manual switches in the model.

Drive-train

Included is the simulation model of the drive-train "‘test_drivetrain.slx"’ and the m-file "‘parameters_test_drivetrain.m"’ necessary to control the model.

The simulation model includes the whole drive-train, up to the carriages attached on the ball screw. Tests for the drive-train like the following of a desired current signal are possible. Also a velocity control for the drive-train is implemented.

Segmented leg with drive-train

Included is the simulation model of the segmented leg with attached drive-train "‘drivetrain_multibody_3DOF.slx"’ and the m-file "‘parameters_drivetrain_multibody_3DOF.m"’ necessary to control the model.

The control models of the bang-bang- and continuous-change-of-stiffness-approaches are implemented on the model and the desired case has to be chosen by manual switches in the model. The model is the combination of the segmented leg model and the drive-train model. Specialties of both can be found in this.

The m-file of the most complex model is shown here. All other m-files could be found on the data-DVD.

- `parameters_drivetrain_multibody_3DOF.m` m-file for the control of the simulation model of the segmented leg with attached drive-train

```
%%%%%%%%%%%%%%%%%%%%%%%%%%%%%%%%%%%%%%%%%%%%%%%%%%%%%%%%%%%%%%%%%%%%%%%%
%simulation of the whole system segmented leg + drive−train%%%%%%%%%%%%%%%
%%%%%%%%%%%%%%%%%%%%%%%%%%%%%%%%%%%%%%%%%%%%%%%%%%%%%%%%%%%%%%%%%%%%%%%%

 clear all;
 close all;

%Parameters Motor maxon EC−4pole 305013
%%%%%%%%%%%%%%%%%%%%%%%%%%%%%%%%%%%%%%%%%%%%%%%%%%%%%%%%%%%%%%%%%%%%%%%%

 theta_M=3.33*10^(−6); %[kgm^2]
 d_M=0.00005; %damping of the motor, unklar [Nms/rad]
 k_M=0.0136; %Drehmomentkonstante [Nm/A]
 R_M=0.102; %Resistance motor [Ohm]
 L_M=0.0000163; %Inductance motor [Henry]
 k_E=1/(700/60*2*pi); %Drehzahlkonstante [rad/(V*s)]
 i_max_M=10.5; %max. current by motor [A]
 t_delay_M=0.00182; %mechanical delay of the motor [s]
 phi_dt_M_max=25000*2*pi/60; %max. phi_dt motor [rad/s]
 V_max=24; %rated voltage motor [V]

%parameters transmission maxon GP 42 C 203116
%%%%%%%%%%%%%%%%%%%%%%%%%%%%%%%%%%%%%%%%%%%%%%%%%%%%%%%%%%%%%%%%%%%%%%%%%
```

```
theta_T=15*10^(-6); %Massentr gheitsmoment transmission [kgm^2]
eta_T=0.81; %Wirkungsgrad transmission
i_T=91/6; %Untersetzung transmission

%parameters transmission spindel item KGT VK14 0.0.414.32
%%%%%%%%%%%%%%%%%%%%%%%%%%%%%%%%%%%%%%%%%%%%%%%%%%%%%%%%%%%%%%%%%%%%%%%%%%%%%%%%

theta_sp=5.3*10^(-5); %mass moment of inertia ball screw [kgm^2]
p_spindel=0.02; %slope p of ball screw [m]
i_spindel=2*pi/p_spindel; %transmission ball screw
eta_spindel=0.85; %efficiency ball screw
r_spindel=0.01; %radius shaft ball screw
alpha_spindel=0.31; %rad 0.31
rho_spindel=0.016; %friction angle ball screw [rad]
F_s_sp=350;%stricbeck paramter I ball screw
F_c_sp=3/10*F_s_sp;;%stricbeck paramter II ball screw
F_v_sp=0.0;%stricbeck paramter III ball screw
v_s_sp=0.0010;%stricbeck paramter IV ball screw
k_v_sp=10;%parameter alternative friction model ball screw

%parameters mechanical structure
%%%%%%%%%%%%%%%%%%%%%%%%%%%%%%%%%%%%%%%%%%%%%%%%%%%%%%%%%%%%%%%%%%%%%%%%%%%%%%%

%masses, densitys
m_top=1.1015; %mass on top [kg]
m_foot=0.297; %mass of the foot [kg]
m_knee=0.3; %mass of additional parts of the leg, concentrated at the knee [kg]
rho_al=2700; %density aluminium [kg/m^3]; links got a weight of ca. 0.3 kg
g=9.81; %gravitational constant [m/s^2]

%geometries
h_stop_hip=0.2; %height of the hip stop [m]
phi_stop_knee=120*pi/180; %maximum angle at the knee, knee stop [rad]
l_link=0.25; %length of shank/thigh [m]
w_link=0.005; %width of shank/thigh [m]
h_link=0.04; %height of shank/thigh [m]
r_pulley=0.034;% %radius of the pulley/knee [m]
phi_knee_zero=2*asin(0.5*h_stop_hip/l_link); %knee angle in rest position [rad]
x_init=0.2;%initial position hip [m]
x_init_foot=0;%initial position foot [m]
x_high=0.45;%switch position + [m]
x_catch=0.22;%switch position - [m]

m_2=l_link*w_link*h_link*rho_al; %weight link [kg]
theta_link=1/12*m_2*(l_link^2+w_link^2)+m_2*(l_link/2)^2;%mass moment of inertia
    segment [kgm^2]
m_3=1; %mass of 1DOF Oscilltor to mimic [kg]

%spring-rates and damping coefficents
k_ground=1000000; %spring rate of the ground [N/m]
k_bowden=556650; %stiffness bowden cable [N/m]
d_ground=100; %damping rate of the ground [N/(m/s)]
d_knee=100; %damping coefficent of the knee stop [Nms/(rad)]

%alternative ground model
```

```
a_ground=0.25*10^9;
b_ground=3;


%Forces and torques
T_fric_rb=0.0012; %friction torque in the roller bearings [Nm]

%friction model - stribeck
v_s=0.001; %stricbeck paramter I hip bearing, carriages drive-train
delta_f=1; %stricbeck paramter II hip bearing, carriages drive-train
F_s=5; %stricbeck paramter III hip bearing, carriages drive-train
F_c=8/10*F_s; %stricbeck paramter IV hip bearing, carriages drive-train
F_v=5; %stricbeck paramter V hip bearing, carriages drive-train

F_s_foot=4.5;%stricbeck paramter I foot bearing
F_c_foot=8/10*F_s_foot;%stricbeck paramter II foot bearing
F_v_foot=1;%stricbeck paramter III foot bearing

%Virtual Model Control
delta_h=0.3;
delta_W=5;
delta_z_0=0.5; %rest length virtual spring [m]

%efficiencies
eta_BC=0.9; %effficiency of the bowden cable, ADP Report p. 52

%%%%%%%%%%%%%%%%%%%%%%%%%%%%%%%%%%%%%%%%%%%%%%%%%%%%%%%%%%%%%%%%%%%%%%%%%%%%%%%%
%start of the simulation and calculation of results
%%%%%%%%%%%%%%%%%%%%%%%%%%%%%%%%%%%%%%%%%%%%%%%%%%%%%%%%%%%%%%%%%%%%%%%%%%%%%%%%
figure(1);
figure(2);
figure(3);
figure(4);
figure(5);
figure(6);
%parameters simulation
StartTime=0;
StopTime=5;

set_param('drivetrain_multibody_3DOF','StartTime',num2str(StartTime));
set_param('drivetrain_multibody_3DOF','StopTime',num2str(StopTime));

%different arrays for test of different values
i_neg_array=[2.5];%negative current for friction compensation [A]
P_array=[0];%PID modell I
P_2_array=[0];%PID modell II
D_array=[0.03];%PID modell I
D_2_array=[0 0.0015];%PID modell II
I_array=[0 (2+1)^2/(4*0.03)];%PID modell I
I_2_array=[0 (1/i_T/i_spindel/eta_T/eta_spindel+k_M*2)^2/(4*k_M^2*0.03)];%PID
    modell II

switch_FF_array=[1];%switch for inclusion of feed-forward term 1=on

for i=1:length(i_neg_array)%parameter iteration I
```

```
%   for ii=1:length(D_array) %possible parameter iteration II for
%   combinationtests
    omega_set=sqrt(2*g/(delta_z_0-x_init));%basic frequency for reaching rest
        length SMO
    %omega_set_array(i);%for testing of different desired frequencies
    k_virtual=omega_set^2*m_3;%basic stiffness for reaching rest length SMO
    %k_virtual=2*g*m_top*(delta_h*(m_top+m_foot)/m_top-x_init+delta_z_0)/(x_init-
        delta_z_0)^2;%stiffness
    %for change of height

    %possible variation of parameters in the loop
    i_neg=i_neg_array(i);
    P=P_array(1);
    P_2=P_2_array(1);
    D=D_array(1);
    D_2=D_2_array(1);
    I=I_array(1);
    I_2=I_2_array(1);
    switch_FF=switch_FF_array(1);

    a{i}=['P =',num2str(P)];%legend of diagrams during parameter variation
%%%%%%%%%%%%%%%%%%%%%%%%%%%%%%%%%%%%%%%%%%%%%%%%%%%%%%%%%%%%%%%%%%%%%%%%%%%%%%%%%%%
%begin of simulation of the model%%%%%%%%%%%%%%%%%%%%%%%%%%%%%%%%%%%%%%%%%%%%%%%%%%%
%%%%%%%%%%%%%%%%%%%%%%%%%%%%%%%%%%%%%%%%%%%%%%%%%%%%%%%%%%%%%%%%%%%%%%%%%%%%%%%%%%%
    sim('drivetrain_multibody_3DOF');

    leg_length=x_top_2-q_foot_2;%distance hip-foot [m]

    int_error_array(i)=max(int_error);%determination of integrated force error [N]

    %generation of different results in diagrams
    figure(1);
    plot(leg_length,F_foot,leg_length,F_GRF_des,'linewidth',2);
    hold on;
    plot(leg_length,k_des,'k-.','linewidth',2);
    xlabel('leg length');
    ylabel('ground reaction force');
    legend(a);
    hold all;
    grid on;
%
    figure(3);
    plot(F_error,'linewidth',2);
    hold on;
    xlabel('time in s');
    ylabel('F_error in N');
    legend(a);
    hold all;
    grid on;
%
%     subplot(3,1,3);
%     plot(F_error_dt,'linewidth',2);
%     hold on;
% %     plot(T_set_virtual,'k-.','linewidth',2);
%     xlabel('time in s');
%     ylabel('F_error_dt in N/s');
%     legend('F_error_dt in N/s');
%     hold all;
%     grid on;
%
    figure(2);
    plot(i_M,'linewidth',2);
    xlabel('time in s');
    ylabel('Motor current in A');
    legend(a);
    grid on;
    hold all;
%%
%%      figure(3);
%%      plot(phi_k,'linewidth',2);
%%      xlabel('time in s');
%%      ylabel('phi in  '); %torque at the knee
%%      legend('knee angle in  ');
%%      grid on;
%%      hold all;
%
    figure(4);
%     subplot(2,1,1);
%     plot(x_1,'linewidth',2);
%     hold on;
    plot(x_top,'linewidth',2);
    hold on;
    plot([0 StopTime],[2*l_link*sin(phi_stop_knee/2) 2*l_link*sin(phi_stop_knee/2)
        ],'b','linewidth',2);
    hold on;
    plot(x_foot,'k—.','linewidth',2);
    hold on;
    xlabel('\textbf{time in s}','FontSize',14,'interpreter','latex');
    ylabel('\textbf{position of hip/foot in m}','FontSize',14,'interpreter','latex
        ');
    title('\textbf{Multibody System — drivetrain}','FontSize',14,'interpreter','
        latex');
    legend(a);
    grid on;
    hold all;
%
%     subplot(2,1,2);
%     plot(x_1_dt_dt,'linewidth',2);
%     xlabel('time in s');
%     ylabel('acceleration of body in m'); %position of body and foot
%     legend('acceleration of spindel');
%     grid on;
%     hold all;
%
    figure(5);
    subplot(3,1,1);
    plot(Load_torque,'linewidth',2);
    hold on;
    plot(Set_torque,'k——','linewidth',2);
    hold on;
    plot(load_torque_real,’b—.’,’linewidth’,2);
    hold on;
    xlabel(’time in s’);
    ylabel(’Torque in Nm’);
    legend(’Torque_{load}’,’Torque_{set}’,’Torque_{real}’);
    grid on;

    subplot(3,1,2);
    plot(F_spindel,’linewidth’,2);
    hold on;
    plot(F_set,’k—’,’linewidth’,2);
    hold on;
    xlabel(’time in s’);
    ylabel(’F spindel in N’); %
    legend(’F spindel’,’F set’);
    grid on;

   subplot(3,1,3);
    plot(x_spindel,’linewidth’,2);
    hold on;
    plot(diff_x_S,’k—’,’linewidth’,2);
    hold on;
    xlabel(’time in s’);
    ylabel(’x spindel in m’); %
    legend(’x spindel’,’Abstand Feder spindel’);
    grid on;

    hold all;

    figure(6);
    plot(int_error,’linewidth’,2);
    hold on;
    xlabel(’time in s’);
    ylabel(’integrated absolute F_{\text{error}}’);
    legend(a);
    grid on;
    hold all;
%%
    figure(7);
    subplot(2,1,1);
    plot(F_fric,’linewidth’,2);
    hold on;
    xlabel(’time in s’);
    ylabel(’friction force on bearing in N’);
    legend(’velocity motor in rad/s’);
    grid on;

    subplot(2,1,2);
    plot(T_load_M,’linewidth’,2);
    hold on;
    xlabel(’time in s’);
    ylabel(’T_load_M’);
    legend(’’);
    grid on;
    figure(8);
    subplot(3,1,1);
    plot(x_1,'linewidth',2);
    hold on;
    xlabel('time in s');
    ylabel('x spindel in m'); %force at the foot
    grid on;

    subplot(3,1,2);
    plot(x_1_dt,'linewidth',2);
    hold on;
    xlabel('time in s');
    ylabel('x_dt spindel in m/s');
    grid on;

   subplot(3,1,3);
    plot(x_1_dt_dt,'linewidth',2);
    hold on;
    xlabel('time in s');
    ylabel('x_dt_dt spindel in m'); %
    grid on;

    hold all;

    hold all;

    figure(9);
    subplot(2,1,1);
    plot(F_foot_2,'linewidth',2);
    hold on;
    xlabel('\textbf{time in s}','FontSize',14,'interpreter','latex');
    ylabel('\textbf{ground reaction force in N}','FontSize',14,'interpreter','
        latex');
    title('\textbf{Multibody System}','FontSize',14,'interpreter','latex');
   %legend(a);
    grid on;
    subplot(2,1,2);
    plot(x_top,'linewidth',2);
    hold on;
    plot(x_foot,'linewidth',2);
    hold on;
    xlabel('\textbf{time in s}','FontSize',14,'interpreter','latex');
    ylabel('\textbf{position of top point in m}','FontSize',14,'interpreter','
        latex');
    title('');
   %legend(a);
    grid on;

    hold all;

    figure(10);
    plot(P_motor,'linewidth',2);
    hold on;
    xlabel('time in s');
    ylabel('power consumption of the motor in W');
    grid on;
%      end;
end;
```

Other models

Included is the simulation model of the segmented leg attached to the cable, which is attached to a rigid end-point "“nonlin_leg.slx"” and the m-file "“parameters_nonlin_leg.m"” necessary to control the model.

Also a m-file "“stribeck_friction.m"” is given, which can be used to calculate different setups of stribeck-friction and to produce diagrams of the resulting friction forces.

A.2.2 Experimental results + analysis

All measured data during experiments is collected here. The data is ordered after the date it was required. Each folder holds the information, which experiment was performed. In the folders there are information about the parameters used during the execution of the experiments.

A.2.3 Graphics, photos and figures

The folder is separated in sub-folders.

- **Diagrams:**
  The .fig-files of all produces diagrams are saved.
- **Mechanical drawings:**
  The drawings of the developed adapters as .pdf-files.
- **Photos:**
  All photos of different parts and the whole structure of MARCO II.
- **Sketches:**
  Different sketches of free body pictures, block diagrams and other basic drawings.

A.3 Tables measurement data

The data for the calibration of the force sensor *Scaime* ZF 0-100 kg is presented. For the load cell no data is available for the test was performed during the absence of the author and no data has been recorded.

A.4 Mechanical drawings

Table A.1.: Data calibration force sensors

Scaime ZF 0-100 kg		load cell 0-30 kg	
weight in g	**output voltage in mV**	**weight in g**	**output voltage in mV**
571	38.827	no data available	
1055	38.707	no data available	
1573	38.615	no data available	
2075	38.616	no data available	
2336	44.107	no data available	
2556	61.888	no data available	
2816	84.727	no data available	
3336	129.126	no data available	
3837	173.026	no data available	
4318	214.654	no data available	
5021	275.111	no data available	
10028	707.558	no data available	
15024	1139	no data available	
20025	1571	no data available	

Table A.2.: Presentation of the integrated error $F_{\text{err,int}}$ over different control parameter settings for the control parameters model I. The time of the experiment is set to $T = 3$ s, the injected energy is set to $\Delta W = 5$ J.

k_D	0.01	0.03	0.05	0.07	0.09	0.11	0.13	0.15	0.17	0.19
k_P	x	x	x	x	x	x	x	x	x	x
0.1	67.74	59.80	67.40	69.79	68.99	67.79	66.86	66.53	66.52	66.79
0.3	75.48	50.29	58.20	60.14	60.48	60.86	60.56	60.60	60.77	61.45
0.5	93.48	43.99	50.62	52.88	53.71	54.33	55.25	55.61	56.04	56.75
0.7	121.57	39.48	44.88	47.21	48.41	49.11	50.19	51.35	51.85	52.67
0.9	155.77	36.70	40.95	43.16	44.13	44.86	45.95	47.15	48.24	48.94
1.1	196.27	34.61	38.02	39.78	40.65	41.22	42.29	43.51	44.80	45.82
1.3	243.51	33.10	35.83	37.19	37.79	38.33	39.14	40.31	41.69	42.96
1.5	289.82	32.33	33.84	35.08	35.45	35.74	36.40	37.58	38.78	40.13
1.7	518.92	31.79	32.67	33.30	33.47	33.49	34.13	35.14	36.38	37.69
1.9	379.48	31.70	31.68	31.88	31.75	31.76	32.15	32.98	34.14	35.41

Table A.3.: Presentation of the integrated error $F_{\text{err,int}}$ over different control parameter settings for the control parameters model I. The time of the experiment is set to $T = 3$ s, the injected energy is set to $\Delta W = 5$ J.

k_{D} k_{P}	0.01 x	0.03 x	0.05 x	0.07 x	0.09 x	0.11 x	0.13 x	0.15 x	0.17 x	0.19 x
0.1	102.16	96.52	89.88	84.07	79.10	75.58	73.26	71.92	71.04	70.82
0.3	80.01	82.91	79.92	75.71	71.91	69.36	67.47	66.45	66.03	65.98
0.5	65.79	72.90	71.15	67.67	65.13	63.67	62.38	61.72	61.50	61.55
0.7	56.00	62.69	62.65	60.61	59.00	58.11	58.05	57.57	57.38	57.68
0.9	52.04	54.50	55.89	54.76	53.77	53.45	53.48	53.84	53.87	54.22
1.1	52.16	48.24	50.43	49.97	49.56	49.31	49.69	50.09	50.67	50.95
1.3	55.33	43.62	46.11	46.14	45.83	45.67	46.05	46.78	47.65	48.03
1.5	62.40	40.11	42.68	42.84	42.77	42.66	43.07	43.66	44.62	45.43
1.7	72.10	37.26	39.69	40.26	39.98	39.95	40.21	40.99	41.96	42.85
1.9	87.36	35.20	37.48	37.88	37.76	37.56	37.82	38.57	39.52	40.47

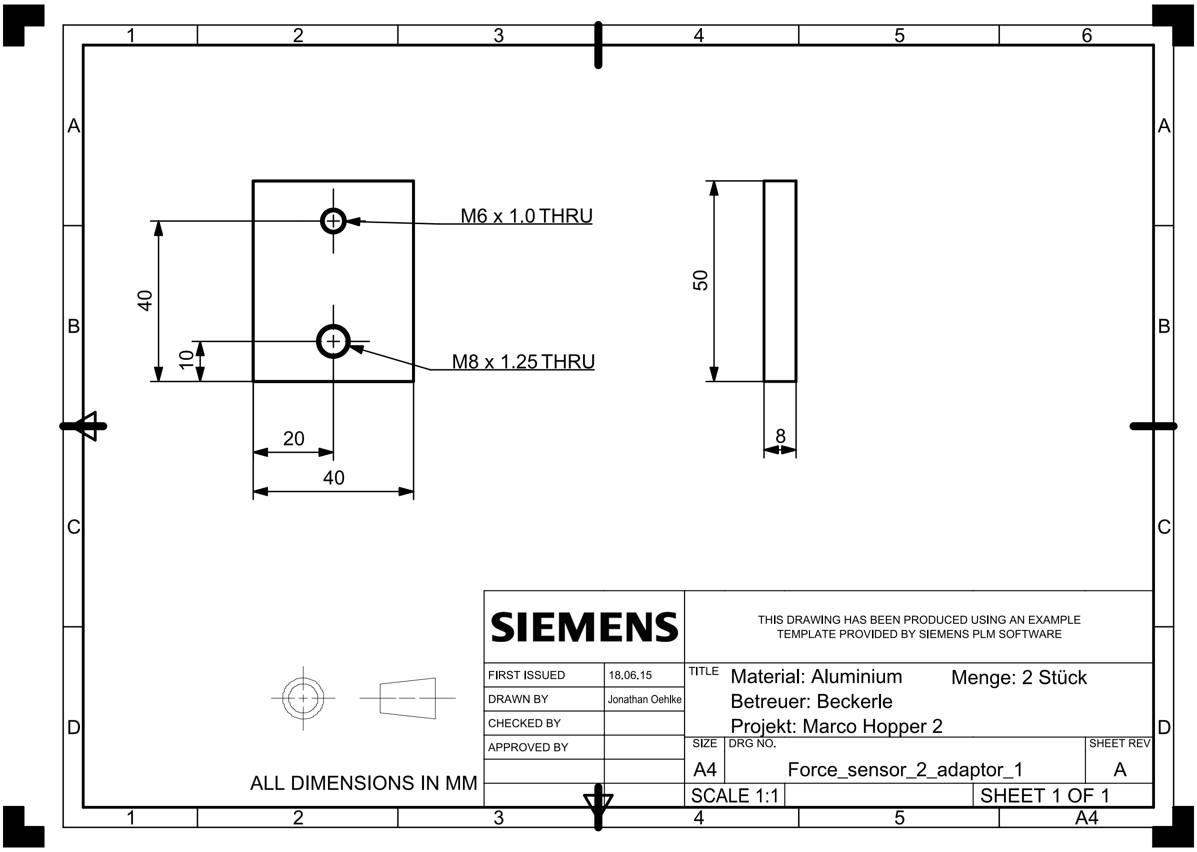
1
2
3
4
5
6
A
B
C
D
M6 x 1.0 THRU
M8 x 1.25 THRU
40
10
20
40
50
8
SIEMENS
THIS DRAWING HAS BEEN PRODUCED USING AN EXAMPLE TEMPLATE PROVIDED BY SIEMENS PLM SOFTWARE
FIRST ISSUED 18.06.15
DRAWN BY Jonathan Oehlke
CHECKED BY
APPROVED BY
TITLE
Material: Aluminium
Menge: 2 Stück
Betreuer: Beckerle
Projekt: Marco Hopper 2
SIZE A4
DRG NO. Force_sensor_2_adaptor_1
SHEET REV A
SCALE 1:1
SHEET 1 OF 1
ALL DIMENSIONS IN MM
A4

Figure A.1.: Adapter force sensor-carriage, Scaime ZF 0-100kg

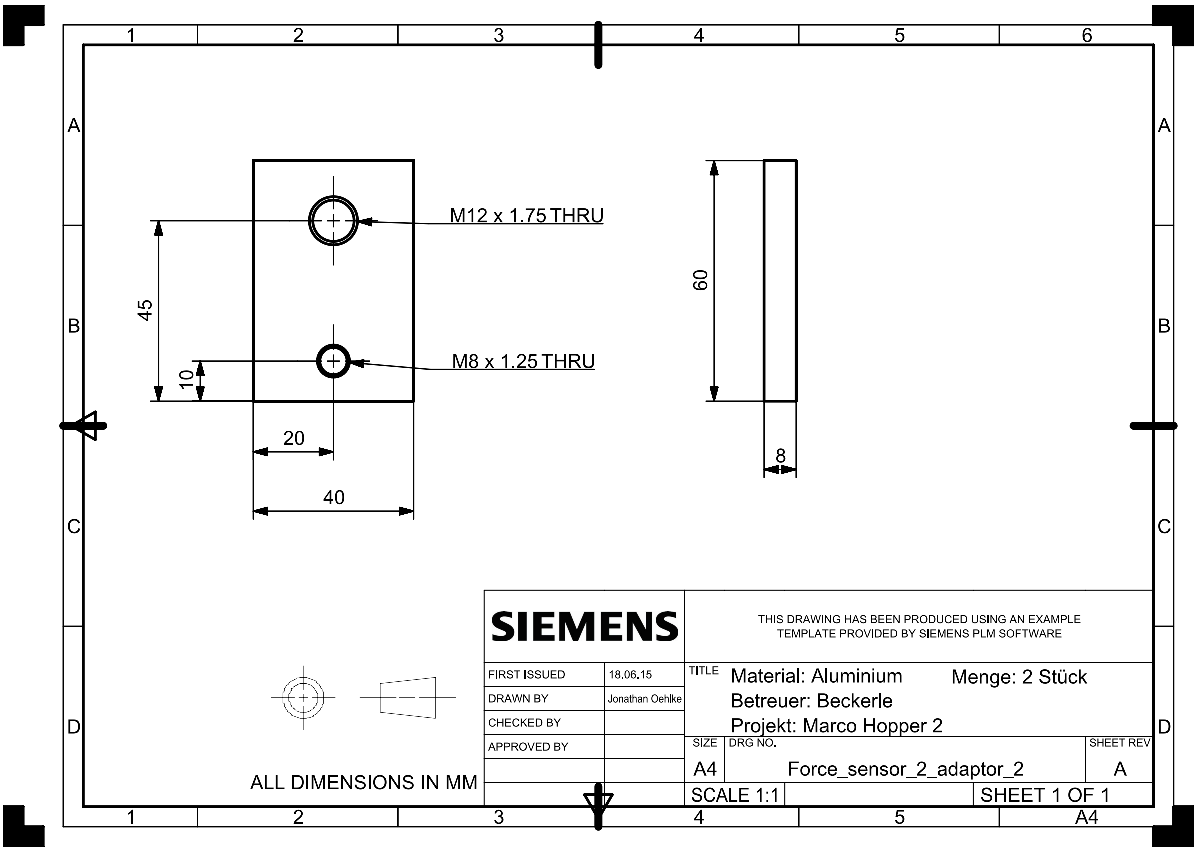
M12 x 1.75 THRU
M8 x 1.25 THRU
45
10
20
40
60
8
SIEMENS
THIS DRAWING HAS BEEN PRODUCED USING AN EXAMPLE TEMPLATE PROVIDED BY SIEMENS PLM SOFTWARE
FIRST ISSUED 18.06.15
DRAWN BY Jonathan Oehlke
CHECKED BY
APPROVED BY
TITLE Material: Aluminium Menge: 2 Stück
Betreuer: Beckerle
Projekt: Marco Hopper 2
SIZE A4
DRG NO. Force_sensor_2_adaptor_2
SHEET REV A
SCALE 1:1
SHEET 1 OF 1
ALL DIMENSIONS IN MM
A4

Figure A.2.: Adapter force sensor-carriage, Megatron 0-200kg

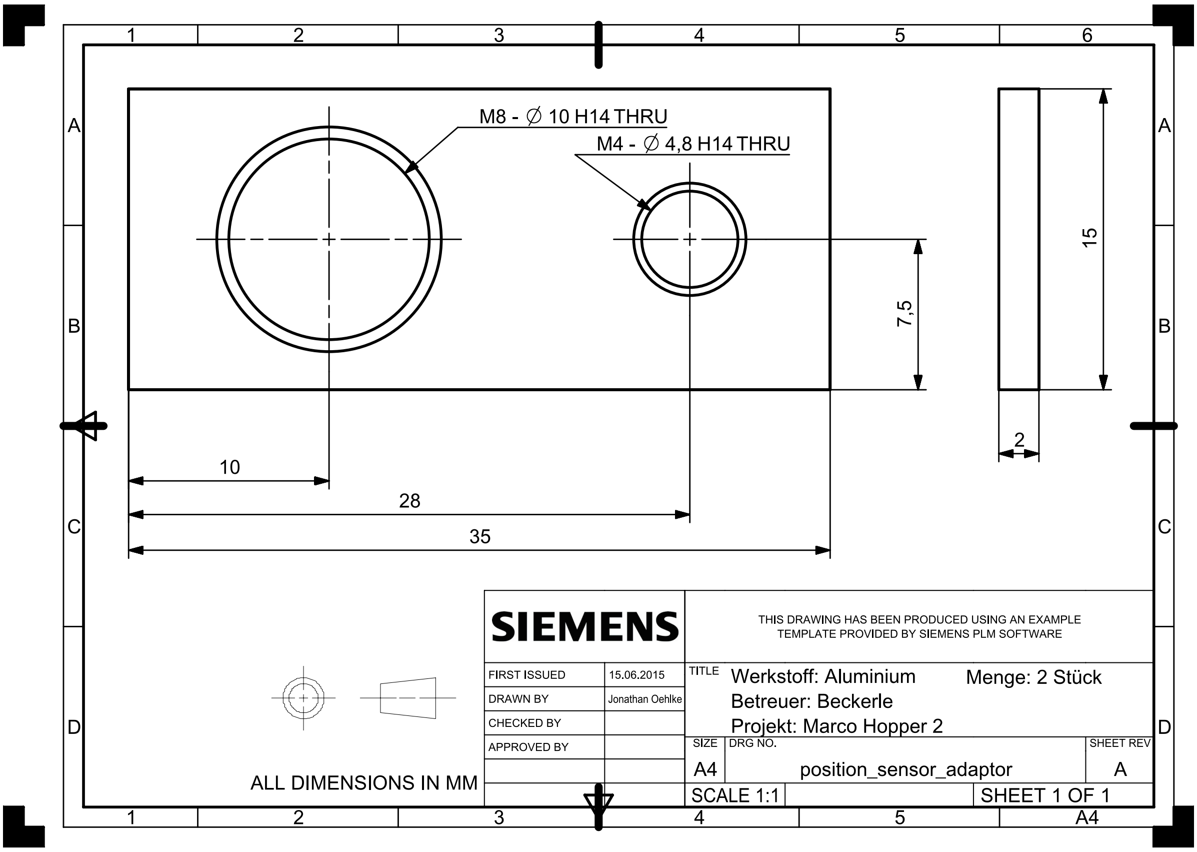
M8 - ∅ 10 H14 THRU
M4 - ∅ 4,8 H14 THRU
7,5
15
2
10
28
35
SIEMENS
THIS DRAWING HAS BEEN PRODUCED USING AN EXAMPLE TEMPLATE PROVIDED BY SIEMENS PLM SOFTWARE
FIRST ISSUED 15.06.2015
DRAWN BY Jonathan Oehlke
CHECKED BY
APPROVED BY
TITLE Werkstoff: Aluminium Menge: 2 Stück
Betreuer: Beckerle
Projekt: Marco Hopper 2
SIZE A4
DRG NO. position_sensor_adaptor
SHEET REV A
SCALE 1:1
SHEET 1 OF 1
ALL DIMENSIONS IN MM
A4

Figure A.3.: Adapter foot position sensor

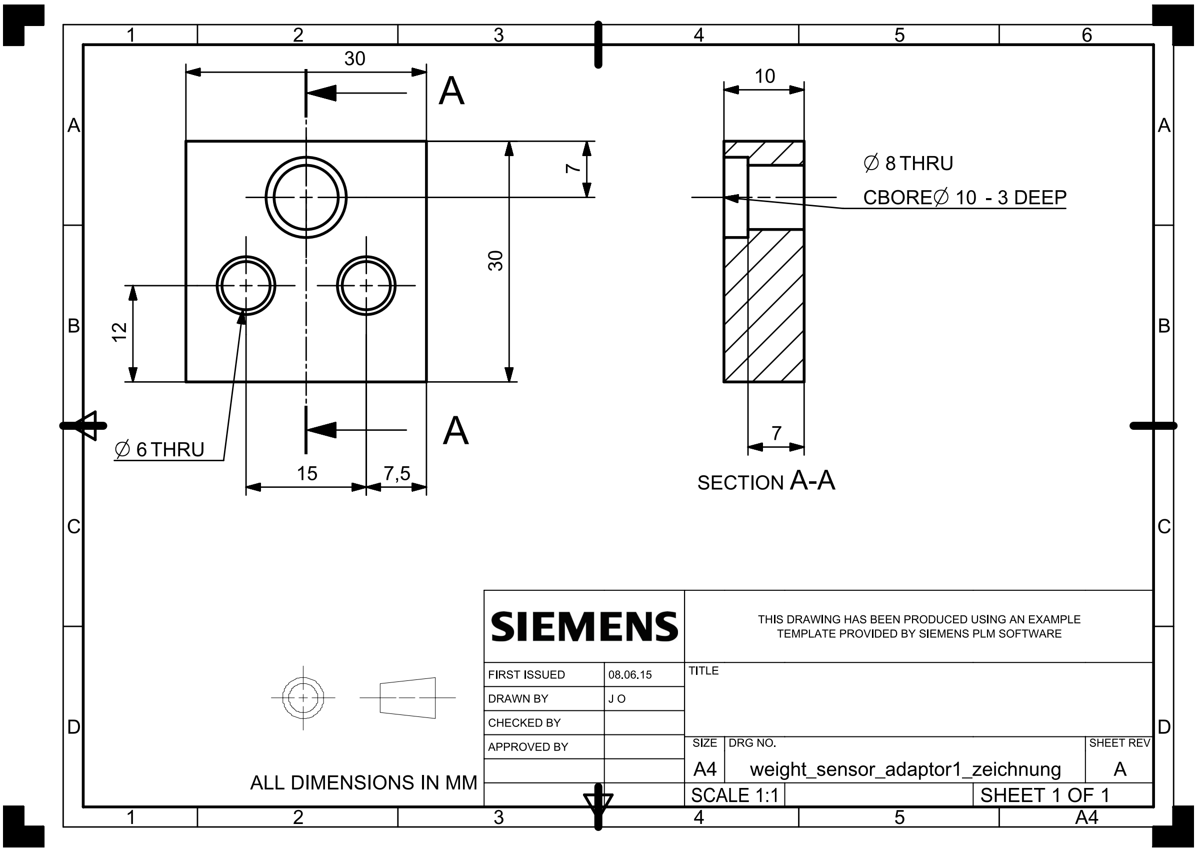
30
A
7
30
12
Ø 6 THRU
15
7,5
A
10
Ø 8 THRU
CBOREØ 10 - 3 DEEP
7
SECTION A-A
SIEMENS
THIS DRAWING HAS BEEN PRODUCED USING AN EXAMPLE TEMPLATE PROVIDED BY SIEMENS PLM SOFTWARE
FIRST ISSUED 08.06.15
DRAWN BY J O
CHECKED BY
APPROVED BY
TITLE
SIZE A4
DRG NO. weight_sensor_adaptor1_zeichnung
SHEET REV A
ALL DIMENSIONS IN MM
SCALE 1:1
SHEET 1 OF 1
A4

Figure A.4.: protection plate force sensor ground reaction force

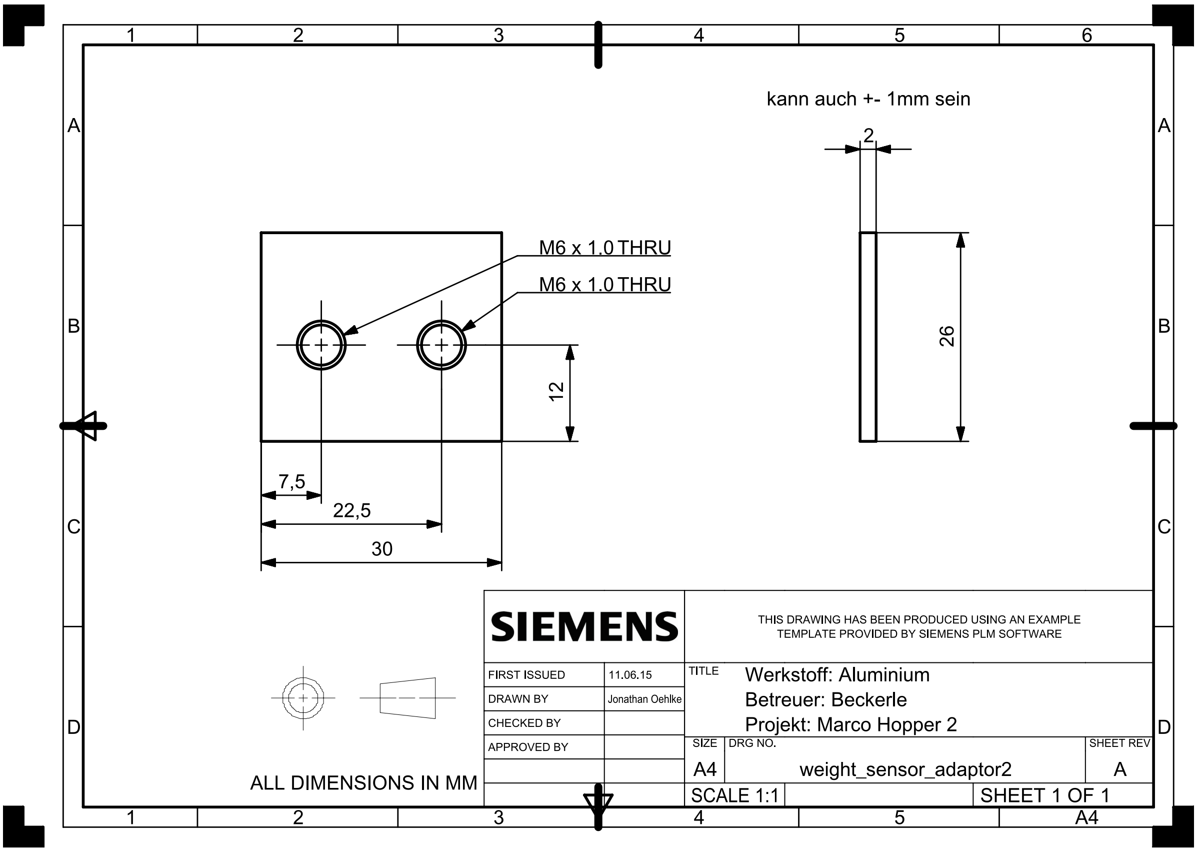
kann auch +- 1mm sein
2
M6 x 1.0 THRU
M6 x 1.0 THRU
12
26
7,5
22,5
30
SIEMENS
THIS DRAWING HAS BEEN PRODUCED USING AN EXAMPLE TEMPLATE PROVIDED BY SIEMENS PLM SOFTWARE
FIRST ISSUED 11.06.15
DRAWN BY Jonathan Oehlke
CHECKED BY
APPROVED BY
TITLE Werkstoff: Aluminium
Betreuer: Beckerle
Projekt: Marco Hopper 2
SIZE A4
DRG NO. weight_sensor_adaptor2
SHEET REV A
ALL DIMENSIONS IN MM
SCALE 1:1
SHEET 1 OF 1
A4

Figure A.5.

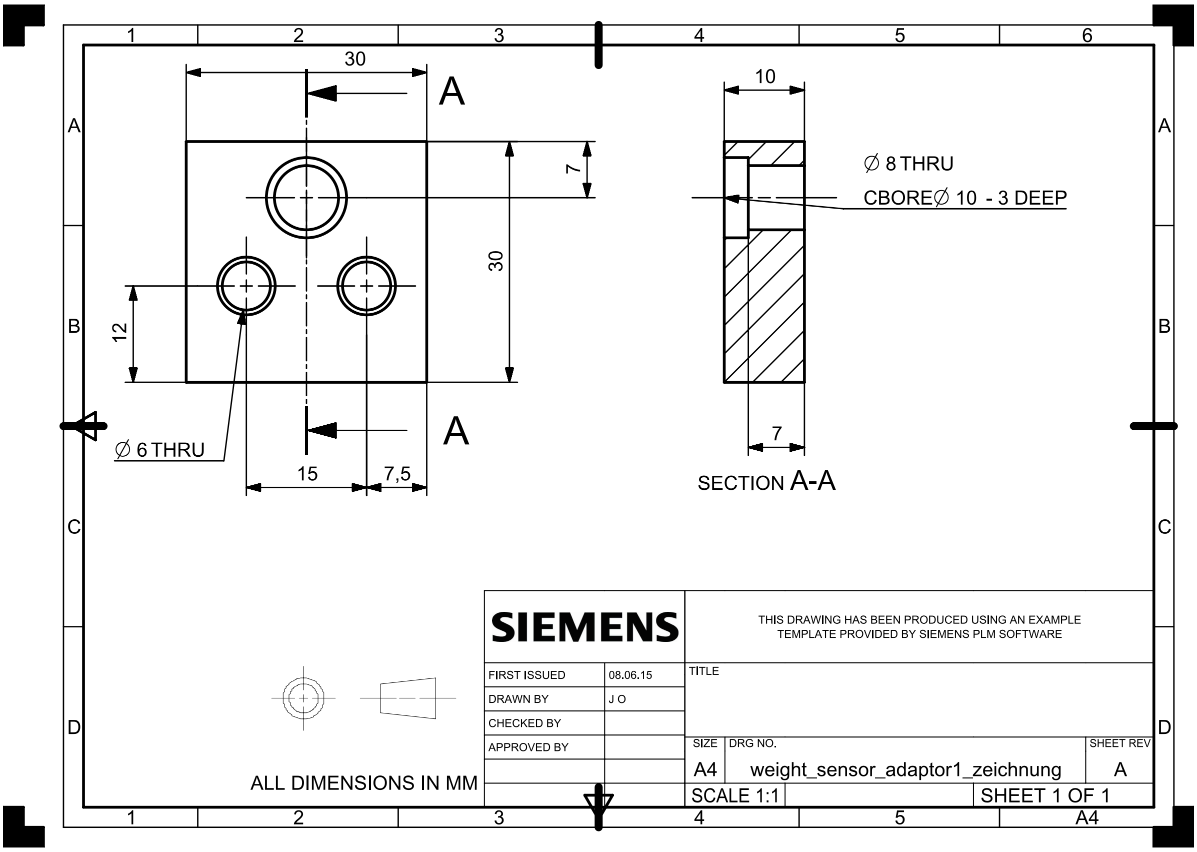
30
A
7
30
12
∅ 6 THRU
A
15
7,5
10
∅ 8 THRU
CBORE∅ 10 - 3 DEEP
7
SECTION A-A
SIEMENS
THIS DRAWING HAS BEEN PRODUCED USING AN EXAMPLE TEMPLATE PROVIDED BY SIEMENS PLM SOFTWARE
FIRST ISSUED 08.06.15
DRAWN BY J O
CHECKED BY
APPROVED BY
TITLE
SIZE A4
DRG NO. weight_sensor_adaptor1_zeichnung
SHEET REV A
SCALE 1:1
SHEET 1 OF 1
ALL DIMENSIONS IN MM
1 2 3 4 5 6
A B C D
A4

Figure A.6.

Bibliography

[1] *Differenzverstärker / Subtrahierer (Operationsverstärker)*. http://www.elektronik-kompendium.de/sites/slt/0210153.htm

[2] *FT-ZF-FEG-0404.indd - ZF-FEG-0404.pdf*. ftp://server.prom-a.ru/Vendors/Scaime/Datasheet/ZF-FEG-0404.pdf

[3] *Gewichtsensor (Load Cell) 0-30kg - Watterott electronic*. http://www.watterott.com/de/Weight-Sensor-Load-Cell-0-30kg

[4] *MPU6050 3-Achsen Beschleunigungssensor + Gyro - 6DOF Modul - Watterott electronic*. http://www.watterott.com/de/MPU6050-6DOF-Modul

[5] *Produkte | Führungswagen | Kugelumlaufführung-Wagen PS 4-15 - 0.0.443.06 | item Online-Shop*. http://www.item24.de/produkte/produktkatalog/produktdetails/products/fuehrungswagen/kugelumlauffuehrung-wagen-ps-4-15-44306.html

[6] *SKF Bearing Calculator*. http://www.skf.com/de/knowledge-centre/engineering-tools/skfbearingcalculator.html

[7] *SKF_Wälzlager-Schmierstoffe - SKF_Waelzlager-Schmierstoffe.pdf*. http://files.ludwigmeister.de/produkte/chemisch/schmiermittel/SKF_Waelzlager-Schmierstoffe.pdf

[8] Blickhan, R.: The spring-mass model for running and hopping. In: *Journal of Biomechanics* 22 (1989), Februar, Nr. 11-12, 1217–27. http://dx.doi.org/10.1016/0021-9290(89)90224-8. – DOI 10.1016/0021–9290(89)90224–8. – ISSN 0021–9290

[9] Cengic, Filip ; Hammen, Florian ; Lahnstein, Jonas ; Souza, Bernardo Spring d. ; Zwetsch, Fabian: Human motions and robotics. Darmstadt, Oktober 2013. – ADP

[10] Craig, John J.: *Introduction to Robotics: Mechanics and Control*. 3 edition. Upper Saddle River, N.J : Prentice Hall, 2004. – ISBN 978–0–201–54361–2

[11] Full, Robert J. ; Koditschek, Daniel E.: Templates and anchors: neuromechanical hypotheses of legged locomotion on land. In: *Journal of Experimental Biology* 202 (1999), Nr. 23, 3325–3332. http://jeb.biologists.org/content/202/23/3325.short

[12] Gross, Dietmar ; Hauger, Werner ; Schröder, Jörg ; Wall, Wolfgang A.: *Technische Mechanik 1*. Berlin, Heidelberg : Springer Berlin Heidelberg, 2009 (Springer-Lehrbuch). – ISBN 978–3–540–68394–0

[13] Gross, Dietmar ; Hauger, Werner ; Schröder, Jörg ; Wall, Wolfgang A.: *Technische Mechanik 3*. Berlin, Heidelberg : Springer Berlin Heidelberg, 2010 (Sringer-Lehrbuch). – ISBN 978–3–642–11263–8

[14] Gross, Dietmar ; Hauger, Werner ; Schröder, Jörg ; Wall, Wolfgang A.: *Technische Mechanik 2*. Berlin, Heidelberg : Springer Berlin Heidelberg, 2014 (Springer-Lehrbuch). http://link.springer.com/10.1007/978-3-642-40966-0. – ISBN 978–3–642–40965–3 978–3–642–40966–0

[15] Haeufle, D.F.B. ; Günther, M. ; Blickhan, R. ; Schmitt, S.: Can Quick Release Experiments Reveal the Muscle Structure? A Bionic Approach. In: *Journal of Bionic Engineering* 9 (2012), Juni, Nr. 2, 211–223. http://dx.doi.org/10.1016/S1672-6529(11)60115-7. – DOI 10.1016/S1672–6529(11)60115–7. – ISSN 16726529

[16] Hill, A. V.: The Heat of Shortening and the Dynamic Constants of Muscle. In: *Proceedings of the Royal Society of London B: Biological Sciences* 126 (1938), Nr. 843, S. 136–195. http://dx.doi.org/10.1098/rspb.1938.0050. – DOI 10.1098/rspb.1938.0050. – ISSN 0080–4649

[17] Kalveram, Karl T. ; Haeufle, Daniel F. B. ; Seyfarth, André ; Grimmer, Sten: Energy management that generates terrain following versus apex-preserving hopping in man and machine. In: *Biological Cybernetics* 106 (2012), Januar, Nr. 1, 1–13. http://dx.doi.org/10.1007/s00422-012-0476-8. – DOI 10.1007/s00422–012–0476–8. – ISSN 0340–1200, 1432–0770

[18] Krämer, Andreas ; Kempkes, Joachim: Modellierung und Simulation von nichtlinearen Reibungseffekten bei der Lageregelung von Servomotoren. (2014). https://opus4.kobv.de/opus4-fhws/frontdoor/index/index/docId/44

[19] Ludwig, C. ; Grimmer, S. ; Seyfarth, A. ; Maus, H.-M.: Multiple-step model-experiment matching allows precise definition of dynamical leg parameters in human running. In: *Journal of Biomechanics* 45 (2012), September, Nr. 14, 2472–2475. http://dx.doi.org/10.1016/j.jbiomech.2012.06.030. – DOI 10.1016/j.jbiomech.2012.06.030. – ISSN 00219290

[20] Markert, Richard: *Strukturdynamik*. Aachen : Shaker, 2013. – ISBN 978–3–8440–2098–4

[21] Mochon, Simon ; McMahon, Thomas A.: Ballistic Walking. In: *Journal of Biomechanics* 13 (1980), Nr. 1, 49–57. http://ac.els-cdn.com/002192908090007X/1-s2.0-002192908090007X-main.pdf?_tid=1a553432-69ac-11e5-bb1c-00000aab0f6b&acdnat=1443862540_506bdaa0ac09f84e47c484f0db512040. – ISSN 0021–9290

[22] Nordmann, Rainer ; Birkhofer, Herbert: *Maschinenelemente und Mechatronik 1*. 3. überarb. Aufl. Aachen : Shaker, 2003. – ISBN 3–8265–9343–X

[23] Pratt, Jerry ; Dilworth, Peter ; Pratt, Gill: Virtual model control of a bipedal walking robot. In: *Robotics and Automation, 1997. Proceedings., 1997 IEEE International Conference on* Bd. 1, IEEE, 1997, 193–198

[24] Pratt, Jerry E.: Exploiting inherent robustness and natural dynamics in the control of bipedal walking robots / DTIC Document. Version: 2000. http://oai.dtic.mil/oai/oai?verb=getRecord&metadataPrefix=html&identifier=ADA475455. 2000. – Forschungsbericht

[25] Radkhah, Katayon ; Maufroy, Christophe ; Maus, Moritz ; Scholz, Dorian ; Seyfarth, Andre ; Von Stryk, Oskar: Concept and design of the biobiped1 robot for human-like walking and running. In: *International Journal of Humanoid Robotics* 8 (2011), Nr. 03, 439–458. `http://www.worldscientific.com/doi/abs/10.1142/S0219843611002587`

[26] Riese, Sebastian ; Seyfarth, Andre: Stance leg control: variation of leg parameters supports stable hopping. In: *Bioinspiration & Biomimetics* 7 (2012), März, Nr. 1, 016006. `http://dx.doi.org/10.1088/1748-3182/7/1/016006`. – DOI 10.1088/1748–3182/7/1/016006. – ISSN 1748–3182, 1748–3190

[27] Seyfarth, André: *Biomechanik - Vorlesungsfolien zur Veranstaltung*. 2014

[28] Seyfarth, Andre ; Häufle, Daniel ; Maus, Horst-Moritz ; Peuker, Frank ; Kalveram, Karl T. ; Grimmer, Sten: Biomechanical and Neuromechanical Concepts for Legged Locomotion. Version: 2012. `https`. In: *Routledge Handbook of Motor Control and Motor Learning*. Routledge, 2012

[29] Seyfarth, Andre ; Kalveram, Karl T. ; Geyer, Hartmut: Simulating muscle-reflex dynamics in a simple hopping robot. Version: 2007. `http://link.springer.com/chapter/10.1007/978-3-540-74764-2_45`. In: *Autonome Mobile Systeme 2007*. Springer, 2007, 294–300

[30] Sharbafi, Maziar A. ; Radkhah, Katayon ; Stryk, Oskar von ; Seyfarth, Andre: Hopping control for the musculoskeletal bipedal robot: BioBiped. In: *Intelligent Robots and Systems (IROS 2014), 2014 IEEE/RSJ International Conference on*, IEEE, 2014, 4868–4875

[31] Vu, H. ; PFEIFER, R. ; Iida, F. ; Yu, X.: Improving energy efficiency of hopping locomotion by using a variable stiffness actuator. In: *IEEE/ASME Transactions on Mechatronics* PP (2015), Nr. 99, S. 1–1. `http://dx.doi.org/10.1109/TMECH.2015.2428274`. – DOI 10.1109/TMECH.2015.2428274. – ISSN 1083–4435

[32] Williamson, Matthew M.: Series elastic actuators. (1995). `http://dspace.mit.edu/handle/1721.1/6776`